Università degli Studi di Trieste

XXX Ciclo del Dottorato di Ricerca in
Earth Science and Fluid Mechanics

ACOUSTIC ANALOGIES AND LARGE-EDDY SIMULATIONS OF INCOMPRESSIBLE AND CAVITATING FLOWS AROUND BLUFF BODIES

Settore scientifico-disciplinare: ICAR/01

Ph.D. Student:	Marta Cianferra
Ph.D. Program Coordinator:	Prof. Pierpaolo Omari
Supervisor:	Prof. Vincenzo Armenio
Co-Supervisor:	Dr. Sandro Ianniello

Academic Year 2016–2017

Author: Marta Cianferra

e-mail: marta.cianferra@phd.units.it

Affiliation: Doctoral School in
"Earth Science and Fluid Mechanics".
Dipartimento di Ingegneria e Architettura,
University of Trieste, Piazzale Europa 1,
I-34127 Trieste, Italy

Supervisor: Prof. Vincenzo Armenio

e-mail: armenio@dica.units.it

Affiliation: Dipartimento di Ingegneria e Architettura,
University of Trieste, Piazzale Europa 1,
I-34127 Trieste, Italy

Co-Supervisor: Dr. Sandro Ianniello

e-mail: sandro.ianniello@cnr.it

Affiliation: CNR-INSEAN, Marine Technology Research Institute,
via di Vallerano, Rome

Day of the defence: 23.03.2018

To cite this work: Marta Cianferra, *Use of the Ffowcs Williams and Hawkings equation for the prediction of hydroacoustic noise for single-phase and cavitating flows.*, Ph.D. Thesis, School of Earth Science and Fluid Mechanics, University of Trieste (2017). Digital resource deposited in the National Legal Deposit service. NBN: *to be assigned.*

Abstract

The research activity reported in this thesis concerns the numerical study of hydroacoustic noise generation and propagation. Sound waves may be emitted whenever a relative motion exists between two fluids or between a fluid and a surface. Examples for which flow-induced noise has been a subject of concern are industrial jets and valves, automobiles, airplanes, helicopters, wood-cutting machinery, ventilation fans, marine propellers, and household rotary lawn mowers.
In nearly all problems of flow-generated noise, the energy source for sound production is a kind of flow unsteadiness. This unsteadiness is not necessary associated to turbulence, as there are numerous cases of tonal sounds (whistles, cavity tones, singing propellers and turbine blades) that involve sinusoidal disturbances in the fluid. A number of other cases of flow-induced sound, at low velocity (or Mach number) especially, involve a restricted region of free shear turbulence (jets) or in contact with a body. An essential ingredient of flow unsteadiness that determines the efficiency of noise production in non-cavitating and bubble-fluids is its own vorticity.
In the latter decades, sophisticated fluid dynamic and acoustic solvers have been developed also in view of the exponential increase of the available computational resources. However a number of aspects related to acoustic modeling need further investigation. This is especially true when noise production and propagation are related to complex physics (among the others hydro-elastic effects, shock waves and cavitation bubbles), to the presence of multiple sources or to the presence of inhomogeneous and moving media.
A direct acoustic model would require the numerical solution of the Navier-Stokes equations for compressible flows. Few studies of this kind are available in literature, mostly limited to 2D cases or elementary configurations. However, two fundamental problems arise: the different time scales between fluid dynamic and acoustic processes and the limited dimensions of the fluid dynamic mesh with respect to the acoustic "far" field. Both aspects make unfeasible the direct adoption of the Navier-Stokes equations for compressible flows in case of practical interest. An alternative choice, commonly in use in literature, is represented by the so–called hybrid methods (descending from the so-called *acoustic analogies*), which allow to decouple the fluid dynamic problem from the acoustic one. The background idea is to treat the flow as a collection of noise sources, and to describe the way the pressure signals interact and propagate in the field through the wave theory. This methodology provides a number of advantages, the most important being that, starting from an essentially confined (fluid dynamic) domain, the acoustic solution is radiated in the (acoustic)

far field at any point of interest. Further, due to the presence of different source terms, the inhomogeneous wave equation provides a simple identification of the dominant source mechanisms taking place in the flow.
In the past decades much attention has been paid to aeroacoustic noise problems (i.e. helicopter rotor noise). Over the years, theoretical and numerical models suitable for transonic or super-sonic flows have been developed, and their effectiveness has been tested. The main source of noise has been identified with the pressure field variation on the blades surface, known as thickness and loading noise. To detect this type of noise source it is enough to consider the linear terms of the Ffowcs Williams and Hawkings (FW-H) equation. In underwater environment the acoustic waves, thus the pressure disturbances, travel at speed much higher than that of the flow motion, such that most of hydrodynamic phenomena are in an incompressible regime. Wave length is commonly much larger than the length scale of the considered problem (such as the immersed body's side). Moreover, vortex developing at the rear of an immersed body, persists on the wake until breaking downstream thus giving a considerable contribution to the noise signature.
Under these conditions, the mechanisms of noise production and propagation need a different modeling. Thus, in this work, different solution methodologies of the FW-H equation are analyzed and discussed in order to account for the non-linear terms. In particular, the advective form of the non-linear terms, suitable for wind-tunnel type of problems, is derived.
The flow field, regarded as a collection of noise impulses, needs to be reproduced accurately. A Large-Eddy Simulation (LES) is here considered as the most advantageous tool to reproduce turbulent flows and, at the same time, deal with cases of practical interest.
The first part of the study is dedicated to the assessment of the model: we perform a LES of a flow around a finite-size square cylinder. We compare the contribution from different terms of the FW-H equation with the fluid dynamic pressure. Different methods which are proposed in literature were considered. The direct integration of the volume terms was found to give the most accurate results. Moreover, through dimensional analysis it is observed that for hydrodynamic problems, where velocity of a body is small compared to the speed of sound, the direct integration of the volume term is licit and practical .
The direct computation of non-linear terms, by integrating on the volume region surrounding the immersed body, is then employed, in the second part of the thesis, for the study of noise signature generated by a flow around three different geometries: sphere, cube and prolate spheroid. In spite of the fact that the frontal section of the bodies has the same area, the analysis shows that a streamlined body is able to produce a pressure signal one order of magnitude lower than that generated by a bluff geometry. Also, the presence of sharp corners enhances the acoustic field generated by the body, both in amplitude and in frequencies. A qualitative analysis between the case of the elongated square cylinder and the cube, shows that the persistence of a two-dimensionally shaped wake when compared to a three-dimensional wake contributes to increase the quadrupole part of the radiated noise.
Last part of the thesis is devoted to a preliminary study of the acoustic field emitted by a cavitating flow.

Cavitation may be interpreted as the rupture of the liquid continuum due to excessive stresses. It is the evaporation of a liquid in a flow when the pressure drops below the saturation pressure of that liquid. The importance of understanding cavitating flows is related to their occurrence in various technical applications, such as pumps, turbines, ship propellers and fuel injection systems, as well as in medical sciences.
There are several types of cavitation. Distinct appearances of cavitation are: sheet cavitation, bubble cavitation and vortex cavitation. Sheet cavitation may occur on hydrofoils, on blades of pumps and propellers, specifically when the loading is high. This type of cavitation can hardly be avoided, because of high efficiency requirements. The dynamics of sheet cavitation often generates strong pressure fluctuations due to the collapse of shed vapor structures, which might lead to erosion of surface material and intense and complex noise track. In this thesis a preliminary study on the cavitation noise is proposed, first considering an isolated bubble then a bubble cloud and then a two-dimensional hydrofoil. In the last chapter, dedicated to concluding remarks, open questions and likely future developments are hinted.
To summarize, the main results of the research are:
a dimensional analysis related to the time delays issue; the derivation of the advective formulation of the non-linear volume term, necessary for evaluating the radiating noise in wind-tunnel problems; the comparison of the noise signature radiated from different bluff bodies, with considerations regarding the contribution of FW-H linear and non-linear terms.

Contents

Chapter 1

Introduction

Analysis of fluid mechanics noise is of primary importance in a number of industrial and environmental applications. The acoustic pollution problems and their own impact on the environment, the stringent regulations concerning transportation industry and military applications are just few examples of the growing attention toward development of theoretical and numerical tools able to perform reliable noise predictions [9, 42]. For this reason, in the latter decades, sophisticated fluid dynamic and acoustic solvers have been developed, also due to the remarkable increase of computational resources. However, a number of aspects related to acoustic modeling need further investigation. This is especially true when noise production and propagation are related to complex physics (among the others, turbulence, shock waves or cavitation bubbles), to the presence of multiple sources (with mutual interference or scattering problems) or to the presence of inhomogeneous and moving media [62, 34].

Fluid dynamic noise represents the propagation of pressure/density disturbances generated by a flow and the evaluation of the acoustic field would require the solution of the Navier-Stokes equations for compressible flows. However, few studies are available in literature where the above mentioned equations are solved numerically, they are mostly limited to 2D cases or elementary configurations (see, for example, Inoue and Hatakeyama [29] and Marsden *et al.* [39]). On the other hand, engineering applications require accounting for realistic three-dimensional (3D) geometry, often in presence of complex source system. This leads to two fundamental problems: the different time scales between fluid dynamic and acoustic processes and the limited dimensions of the fluid dynamic mesh with respect to the acoustic wavelength. Both aspects make the direct use of the Navier-Stokes equations for acoustic purposes very complex and computationally demanding. An alternative choice, commonly in use in literature, is represented by the so–called acoustic analogy, which allows to decouple the fluid dynamic problem from the acoustic one. The background idea is to treat the flow as a collection of noise sources, and to describe the way pressure signals interact and propagate in the field through the wave theory. This methodology provides a number of advantages, the most important being that, starting from an essentially confined (fluid dynamic) domain, the acoustic solution can be radiated in the acoustic far field at any

point of interest. Further, due to the presence of different source terms, the inhomogeneous wave equation provides a simple identification of the dominant source mechanisms taking place in the flow.

The original Lighthill analogy [35] represents a rearrangement of the fundamental conservation laws of mass and momentum into an inhomogeneous wave equation. Lighthill's work was first extended by Curle [15], who accounted for the possible presence of a body in the flow field, and subsequently by Ffowcs Williams and Hawkings [18], who developed a more comprehensive formulation in which the body could be considered in motion. Accordingly, earlier formulations appear to be special cases of the FW-H equation. A very useful feature of the FW-H equation is that its original differential form can be turned into an integral formulation (by the use of the free-space Green's function), thus enabling the assessment of the acoustic field through a relatively simple post-processing of fluid dynamic data. Another important feature is the relationship between the resulting acoustic pressure and three different integral terms (corresponding to three different source terms of the FW-H differential equation), which are representative of all possible noise generation mechanisms. Two terms correspond to surface (hereafter referred to as 2D) integrals. Whether the integration domain corresponds to the surface of the body source, they identify two processes: the noise generated by the fluid displaced by the body (thickness component) and that coming from the fluid dynamic loads acting on the body surface (loading component). In this case, the 2D integrals are recognized as the "linear" terms of the FW-H equation and coincide (for a stationary body) with the formulation proposed by Curle. The third term of the FW-H equation accounts for all possible sources occurring in the field as a result of the flow-body interaction (turbulence, vorticity, etc.); it is known as the nonlinear (quadrupole) noise and, in principle, requires a volume (hereafter referred to as 3D) integration over the whole fluid region affected by the body motion. The direct evaluation of such nonlinear term has been carried out rarely, for different reasons. First of all, it has always been considered computationally demanding and complex to be implemented. Further, for many years the quadrupole noise was believed to be relevant for bodies moving at a high speed only (transonic or supersonic regime), when the flow is affected by the presence of shock waves; at these conditions, some complex generating noise mechanisms arise (depending on body motion and the position of the measurement point [25]) and the kernels of the volume integrals may become singular. However, it is worth pointing out that, for a marine propeller, the need to compute the FW-H quadrupole term at (very low) subsonic regime has been recently called into question and its contribution to the (hydro)acoustic far field seems to be far from negligible [27]. The (aero)acoustic community moved towards some alternative approaches, as the Kirchhoff method [32] and, subsequently, the so–called porous formulation [17, 7].

The porous formulation consists of moving the 2D integrals from the body surface over an external, closed and "permeable" radiating surface S_P, embedding the body together with the whole fluid region containing the relevant nonlinear sources. This allows to account for the contribution of the quadrupole sources located inside the domain wrapped by the surface S_P through a simple and fast 2D integration. The main drawback of the method is that the reliability of noise prediction is sensitive to the choice of the integration domain

and to the accuracy of fluid dynamic data available on S_P. Moreover, in many practical problems (as a marine propeller, or, in general, those characterized by the presence of a long, vortical wake advected downstream) the noise sources can be hardly embedded within a closed domain, and the vorticity crossing the porous surface gives rise to a spurious contribution of numerical nature. In literature, this undesired behavior is known as the *end–cap problem*.

To avoid this problem, in literature, it is common to place the porous domain in a region where the vorticity of the flow results negligible. In the case of a vorticity wake persisting downstream, the "outlet" side of the porous domain is omitted, so as to have an open domain of integration.

In recent years, the porous formulation has been employed by several authors and improved in many aspects. As regards the end–cap problem, Lockard and Casper [37] developed a correction to account for fluid dynamic sources propagating through the permeable surface. Their quadrupole boundary correction worked encouragingly for several two-dimensional test cases and was also employed for a flow around a three–dimensional cylinder. In order to reduce the spurious noise due to the end–cap problem, Rahier *et al.* [49] proposed to add 2D flux terms representing an approximation of the complementary volume integral. The effectiveness of their method was tested for an isolated vortex and a turbulent jet. Nitzorski and Mahesh [44] developed a sophisticated end–cap solving technique, based on multiple exit planes, over which the flux of quadrupole terms are subtracted and correlated to correction parameters computed dynamically; this technique was first validated considering a convecting potential vortex and, then, successfully applied to the study of the noise propagating from the turbulent flow around an infinite circular cylinder, for different Reynolds numbers.

To summarize, recent literature has demonstrated the importance of the non-linear quadrupole terms in the far field noise propagation for a wide class of engineering problems; the direct integration of the 3D volume terms has been avoided for a series of problems, the most important being the evaluation of the time-delay which makes the computation impractical. The evaluation of these terms has been reconsidered through a porous formulation which transforms 3D volume integrals onto 2D integrals over a porous surface embedding the noise source. Techniques have been developed to solve the end-cap problem.

As regards the base fluid-dynamic field to be used within the context of the hybrid methods, in literature it has been well recognize that the quality of the data plays a very important role (for a discussion see the review paper of Brentner and Farassat [8]). More recently, Lockard and Casper [37] found discrepancies between calculations using detached–eddy simulation (DES) and the Spalart–Allmaras Reynolds Averaged Navier-Stokes (RANS) turbulence model, thus emphasizing the need for very accurate input dataset. A similar conclusion can be found in the work of Ianniello *et al.* [26], where the authors studied the hydroacoustic behavior of a marine propeller combining a RANS simulation with the FW-H porous method; they highlighted the importance of the FW-H nonlinear terms and demonstrated the inadequacy of a RANS approach to capture the nonlinear noise sources required to achieve an accurate noise prediction. Nitzorski and Mahesh [44] underlined that for highly turbulent flows a LES led to better results than Unsteady-RANS.

The adequacy of results from Large–Eddy simulations (LES) in conjunction with the acoustic analogies was investigated by different authors [47, 58], who focused their attention on the high frequencies cut-off related to the unresolved sub-grid scales; their main conclusion was that filtering removes the small-scales fluctuations contributing to the higher derivatives of the Lighthill's tensor. However, the small scales, being not strongly correlated, are not expected to contribute significantly to the noise in the far field.

To summarize, in hydrodynamics, the new concept of 'silent ship' for reducing the environmental impact of cruise ships, as well as military applications are pushing toward new and state-of-art methodologies for the analysis of the radiated noise from immersed objects (among the others, ship propellers). It must be emphasized that the effect on the far-field noise of a persistent wake in hydrodynamics is more relevant and important to study than in aeroacoustics. This is the reason for which most research in hydroacoustic is oriented toward development of methodologies for an accurate reproduction of the non-linear terms coming from the wake. Among the others, the porous methodology has given encouraging results although the problem of closure of the domain in the wake region appears not fully solved and an application to realistic cases is still not available. We consider the 'standard' application of the porous technique and compare results with those obtained by direct volume integration. About this latter aspect, it is worth mentioning that, although the mathematical formulation of the volume term (at least for a body in motion in a fluid otherwise at rest) is known in literature since the original Lighthill manuscript, a direct volume integration has been always avoided due to the the time delays issue. The compactness condition for the noise source has been applied tout court to hydrodynamics without performing a rigorous dimensional analysis highlighting the main difference between the two field, namely the very different sound speed and the rotational velocity of blades.

In this context, the results of the present work concern:

- highlight these differences, performing a rigorous analysis of the problem of the time delays in hydrodynamic applications;
- show that in hydrodynamics, the direct integration of the volume terms is feasible and advantageous;
- derive the advective formulation of the non-linear volume term, necessary for evaluating the radiating noise in wind-tunnel problems, which basically are the standard problems in computational fluid dynamic applications;
- apply the acoustic analogy coupled with LES to compare the noise signature radiated from different archetypal geometries;
- implement the acoustic formulations within the OpenFOAM® platform as post-processing utilities.

Last part of the thesis is dedicated to an introductory study on cavitation noise.

Cavitation is the evaporation of a liquid in a flow when the pressure drops below the saturation pressure of the liquid. The importance of understanding cavitating flows is related to their occurrence in various technical applications, such as pumps, turbines, ship propellers and fuel injection systems, as well as in medical sciences such as lithotripsy treatment and the flow through artificial heart valves. The occurrence of low pressure regions in flows is a well-known phenomenon. For example, in the case of a Venturi, i.e. a converging duct followed by a diverging one, the velocity is maximum at the throat where the cross section is minimum. Then, according to Bernoulli equation, the pressure is minimum there and the risk of cavitation is maximum. Another example is the flow around a foil at a given angle of attack which is representative of that around the blades of a hydraulic machine. From classical hydrodynamics, it is well-known that the foil is subject to a lift because of a lower pressure on the suction side in comparison to the pressure side. Hence, the suction side is expected to be the place where cavitation will first develop. Last example is that of vortices which are very common structures in many flows. Because of the rotation and the associated centrifugal forces, the pressure in the core of such structures is lower than outside. Hence vortices are likely to cavitate in their core. There are actually many situations in which cavitating vortices can be observed as tip vortices or coherent vortical structures in turbulent flows like wakes or shear layers. where Kelvin-Helmholtz instability occur.

In devices such as propellers and pumps, cavitation causes a great deal of noise, damage to components, vibrations, and a loss of efficiency. Cavitation has also become a concern in the renewable energy sector as it may occur on the blade surface of tidal stream turbines. When the cavitation bubbles collapse, they force energetic liquid into very small volumes, thereby creating spots of high temperature and emitting shock waves, the latter becoming a source of noise. The noise created by cavitation is a relevant problem for military submarines, as it increases the chances of being detected by passive sonar. Although the collapse of a small cavity is a relatively low-energy event, highly localized collapses can erode metals, such as steel, over time.

The theory of classical bubble dynamics was started by Lord Rayleigh (1917) [50] during his work for the Royal Navy investigating cavitation damage of ship propellers. Plesset (1949) [48] first applied the Rayleigh equation to the problem of traveling cavitation bubbles. In the recent decades the collapse mechanism of a single isolated bubble has been studied both theoretically and experimentally. Experimental observations on the collapse of a single bubble as well as a bubble cloud demonstrate that violent radiated pressure waves occur with amplitudes of the order of 100 bar, see for example Fujikawa and Akamatsu [21]. Reisman *et al.* [51] experimentally investigated the break-up and collapse of sheet and vortex cavities and observed strong pressure pulses on a hydrofoil surface.

For what concerns noise emissions from bubbles significant contributions come from [10, 13, 12, 16, 64, 53], where dynamics and acoustics of a spherical (or deformable) gas/vapor bubble, steady or rising on a fluid column were investigated.

Numerical techniques frequently used for simulating a limited number of bubbles can be subdivided based on how they treat the interface between the liquid and the gas. Interface tracking techniques place grid nodes on the interface and the grid is thus deformed by

the bubble motion. Conversely, interface capturing techniques employ a static grid and therefore do not place grid points on the interface, rather they reconstruct the interface from a marker in the flow field. Although the former techniques provide a sharper representation of the interface than the latter for the same grid spacing, the complexity of the interface motion is more limited. In interface tracking the moving boundary, called interface in the following, is explicitly described by the computational mesh. Hence, the movement of the interface has to be accounted for by adjusting the position of the nodes on the interface. Interface tracking approaches are known to provide great accuracy, yet their applicability is limited in the case of severe interface motion. Only the flow in the liquid phase is studied and is supposed to circumvent the cavity. The interface may be simply the bubble wall, that separates the vapor from the liquid phase. In many cases of practical interest, the huge number of bubbles developing in the flow (e.g. 1000 per cm^3 liquid) and consequently huge number of interfaces to be tracked, would exclude the interface tracking methods. Multicomponent methods describe the cavitating flow by adopting a full set of equations, i.e. continuity, momentum and energy conservation equations, for the vapor phase, the liquid phase and sometimes even an inert gas phase together with their own thermodynamic relations. They allow for both mechanical and thermal non-equilibrium to be taken into account. These methods are assumed to possess more generality, but they are computationally expensive. The homogeneous-mixture methods are generally preferred when one phase (or component) that is very finely dispersed within the other phase (or component.) Many bubbly flows come close to this limit and can, at a first approximation, be considered homogeneous.
The Volume-of-Fluid (VOF) method tracks the motion of a certain fluid volume through the computational domain. The standard VOF method does account for the convective transport, but not for the phase transition. In this work a mixture model based on VOF method accounting for phase transition was adopted. The change of the cell vapor fraction depends on the number of bubbles per cell volume times the volume change of a single bubble and the convective transport.
Different forms of the transport equation-based cavitation models have been proposed in literature. The main differences are due to different source terms that are needed for cavity generation and destruction. All the models have introduced empirical factors to regulate the mass transfer. These empirical factors have been tuned based on numerical experimentation. The choice of the constants in the empirical relations appears to be somewhat arbitrary.
There are not many experimental or numerical data available in literature on the pressure field generated by cavitating flows, especially for simple cases that can be reproduced by manageable numerical simulations. In fact, the experiments are conducted at very high Reynolds numbers and the dependence on the parameters makes direct comparisons difficult. Moreover, the effects of three-dimensionality clearly influence the dynamics of the cavity and must be taken into account for a realistic analysis. Therefore, the present study deals mainly with verifying the reliability of FW-H methods to study cavitating flows and only preliminary considerations are proposed.

The Large-Eddy Simulations were performed through the use of OpenFOAM® software. Other codes, concerning simpler cases dealt with in this thesis, as for example, the monopole field, the advected vortex and the bubble cloud, have been written with Fortran.

Chapter 2

Simulation methodology

In this chapter an overview of the mathematical models adopted to reproduce the fluid-dynamic and acoustic phenomena is proposed.

Different physical phenomena are simulated:

- the fluid dynamics is solved using the Large-Eddy Simulation method. The flow is considered incompressible, Smagorinsky and dynamic Lagrangian turbulence model are used (section 2.2);
- the acoustic field is reconstructed by adopting a hybrid method. It is assumed to propagate in an homogeneous medium and any feedback of the acoustic waves on the fluid flow are neglected (section 2.3);
- the presence of a mixture in fluid medium can be simulated. A general mixture model is applied to the case of vapor gas in water. The fluid evaporation and condensation rates are based on bubble dynamic model (which is reported in the later section 6.2).

The governing equations for a single-phase flow are the continuity equation and the momentum equation. They read, respectively:

$$\frac{\partial \rho}{\partial t} + \frac{\partial (\rho u_i)}{\partial x_i} = 0, \tag{2.1}$$

$$\frac{\partial (\rho u_i)}{\partial t} + \frac{\partial (\rho u_i u_j)}{\partial x_j} = -\frac{\partial p}{\partial x_i} - \rho g \delta_{i3} + \frac{\partial}{\partial x_j}[2\mu S_{ij} - \frac{2}{3}\mu(\nabla \cdot \mathbf{u})\delta_{ij}]. \tag{2.2}$$

where u_i is the i-component of the fluid velocity vector, p is the pressure, μ is the dynamic viscosity, S_{ij} is the strain rate tensor, g is the gravitational acceleration. The set of governing equations is completed with the energy equation and the equation of state that relates pressure with density and temperature. In incompressible flows the fluid density ρ is assumed constant and drops out from the continuity equation which reduces to $\nabla \cdot \mathbf{u} = 0$.

Indeed, conservation of mass corresponds to conservation of the volume and the divergence free condition simplifies the diffusive term in the momentum equation (2.2).
Equations (2.1, 2.2) are used to reproduce the motion of single-phase flows. As we will see, the equations of Lighthill and FW-H derive from a re-arrangment of the above conservation equations.

The first part of this chapter introduces the Large-Eddy Simulation approach along with the two sub-grid models used in the present study.

Then the derivation of Lighthill and FW-H equations is described, together with the different integral solution methods adopted.

2.1 Large-Eddy Simulation

A turbulent flow is composed by vortices of different sizes. Large eddies are unstable and break up, transferring their energy to smaller eddies. This *energy cascade* occurs until the molecular viscosity is effective in dissipating the kinetic energy. The eddies in the largest size range have length scale comparable to the flow scale, they are anisotropic and are affected by the boundary conditions of the flow. The small scale eddies are statistically isotropic and less case-dependent than the large ones.
A Direct Numerical Simulation (DNS) solves the turbulent flow entirely, so it must be able to perceive the smallest temporal and spatial flow scales. The more the Reynolds number is high, the more the difference between largest and smallest scales is considerable.
A Large-Eddy Simulation (LES) exactly computes the large structures of motion, while the small scales of motion (*i.e.* with a characteristic length smaller than the grid cells width) are modeled with a Sub-Grid Scale (SGS) turbulence model. In practice, the governing equations are filtered by a spatial filter, the removal of the small-scale motion is performed by the numerical grid. The resolved quantity $\overline{u}_i$ is in the filter method defined by

$$\overline{u}_i(\boldsymbol{x},t) = \int_D u_i(\boldsymbol{x}',t) G_\ell(\boldsymbol{x}-\boldsymbol{x}')d\boldsymbol{x}', \tag{2.3}$$

where D is the entire domain. Different filter functions G can be adopted. The most commonly used, named *top-hat*, is defined by the computational grid:

$$G_{\overline{\Delta}}(\boldsymbol{x}-\boldsymbol{x}') = \begin{cases} \frac{1}{\overline{\Delta}} & \text{if } |\boldsymbol{x}-\boldsymbol{x}'| \leq \frac{\overline{\Delta}}{2} \\ \\ 0 & \text{otherwise} \end{cases} \tag{2.4}$$

where the filter length is the local grid width, defined by

$$\ell = \overline{\Delta} = (\Delta_x \Delta_y \Delta_z)^{1/3}, \tag{2.5}$$

and $\Delta_{x/y/z}$ are the local cell dimensions in x, y, z directions, respectively.

The LES approach provides an unsteady and three-dimensional solution for turbulent fluid flow problems. Furthermore, it requires a coarser mesh compared to DNS and it is less computationally demanding.
In the present work, the LES methodology is adopted together with the Smagorinsky and the dynamic Lagrangian turbulent model alternately, they are presented in the following section 2.2.

2.2 LES turbulent model

In this section, the filtered momentum equations are presented and both Smagorinsky and dynamic Lagrangian turbulent models are derived.
Applying the implicit (meaning that the cell size provides the filter size) grid filter (2.4) to the momentum equation (2.2), considering the case of incompressible flows at constant density ρ_0, ones obtains:

$$\frac{\partial \overline{u}_i}{\partial t} + \frac{\partial \overline{u}_i \overline{u}_j}{\partial x_j} = -\frac{1}{\rho_0}\frac{\partial \overline{p}}{\partial x_i} + \nu \frac{\partial^2 \overline{u}_i}{\partial x_j \partial x_j} - \frac{\partial}{\partial x_j}\tau_{ij}^{SGS} - g\delta_{i3}, \tag{2.6}$$

where the fluctuations term, named also *residual stress tensor*, is defined by:

$$\tau_{ij}^{SGS} = \overline{u_i u_j} - \overline{u}_i \overline{u}_j. \tag{2.7}$$

The residual tensor can be divided in the anisotropic and isotropic part:

$$\tau_{ij}^{SGS} = \underbrace{\tau_{ij}}_{anisotropic} + \underbrace{\frac{1}{3}\tau_{kk}^{SGS}\delta_{ij}}_{isotropic}. \tag{2.8}$$

The isotropic part of the *Sub-Grid Scale* (SGS) stress tensor contains the sum of the SGS normal stresses τ_{kk}^{SGS} which is twice the kinetic energy k^{SGS} of the SGS fluctuations and acts like a pressure.
This component is therefore added to the filtered pressure term, so as to obtain a new pressure variable P:

$$P = \overline{p} + \frac{2}{3}k^{SGS}. \tag{2.9}$$

The anisotropic part can be interpreted as the contribution of the small scales of motion (*i.e.* smaller than the grid width) to the large scales and need to be modeled with a turbulent model.
The description of the LES methodology here reported has been drawn mainly from [54, 63].

2.2.1 Smagorinsky model

The most popular eddy-viscosity SGS model is the Smagorinsky model [60] . The anisotropic stress tensor τ_{ij} is approximated by relating it to resolved rate of strain $\overline{S_{ij}}$ via an artificial *eddy viscosity* ν_t:

$$\tau_{ij} = -2\nu_t \overline{S_{ij}}, \tag{2.10}$$

where

$$\overline{S_{ij}} = \frac{1}{2}\left[\frac{\partial \overline{u}_i}{\partial x_j} + \frac{\partial \overline{u}_j}{\partial x_i}\right] \tag{2.11}$$

is the resolved strain rate tensor. This model is also known as *eddy-viscosity model*.
The eddy viscosity ν_t characterizes the unresolved SGS fluctuations and has to be derived. Smagorinsky proposed to relate ν_t to the strain rate tensor:

$$\nu_t = C_s \overline{\Delta}^2 |\overline{S_{ij}}|, \tag{2.12}$$

where C_s is the Smagorinsky constant for SGS momentum fluxes. Note that the constant C_s is always positive, thus the energy transfer is everywhere from the large scales to the small scales and energy backscattering is not allowed.
The Smagorinsky constant can be evaluated from analytical considerations, experiments or DNS. The main drawback of setting C_s to constant value, relays in the assumption of flow homogeneity. Close to solid boundaries, where the turbulent length-scales decrease, the Van Driest damping function [61] is usually applied to overcome such limitation.

2.2.2 Dynamic Lagrangian turbulent model

In a non-homogeneous flow, the best suited approach is to determine C_s^2 dynamically.
In Germano *et al.* [22] the following exact identity is derived, that establishes a link between the sub-grid tensor at two different filtering levels $\bar{\cdot}$ and $\widehat{\cdot}$ with respective filtering length scales $\overline{\Delta}$ and $\widehat{\Delta} \geq \overline{\Delta}$:

$$\underbrace{\widehat{\overline{u}_i\overline{u}_j} - \widehat{\overline{u}}_i\widehat{\overline{u}}_j}_{L_{ij}} = \underbrace{\widehat{\overline{u_iu_j}} - \widehat{\overline{u}}_i\widehat{\overline{u}}_j}_{\mathcal{T}_{ij}} - \underbrace{(\widehat{\overline{u_iu_j}} - \widehat{\overline{u}_i\overline{u}_j})}_{\widehat{\tau}_{ij}}. \tag{2.13}$$

The stress tensors $\widehat{\tau}_{ij}$ and $\mathcal{T}_{ij}$ can be modeled by the Smagorinsky eddy-viscosity model:

$$\widehat{\tau}_{ij} = \cong -2C_s^2\overline{\Delta}^2 \ \widehat{|\overline{S}|\overline{S}}_{ij},$$

and

$$\mathcal{T}_{ij} = \cong -2C_s^2(2\overline{\Delta})^2 \widehat{|\overline{S}|\overline{S}}_{ij}.$$

being $\widehat{\Delta} = 2\overline{\Delta}$.
Inserting the latter in (2.13), we obtain an over-determined system of equations for the unknown C_s^2. In order to solve the system we should minimize the residual associated to the use of Smagorinsky approximation, defined as:

$$e_{ij} = L_{ij} - 2\overline{\Delta}^2\left[C_s^2\widehat{|\overline{S}|\overline{S}}_{ij} - 4C_s^2\widehat{|\overline{S}|}\widehat{\overline{S}}_{ij}\right] \tag{2.14}$$

$$= L_{ij} - C_s^2 M_{ij}. \tag{2.15}$$

The most used solution is to operate a least-square minimization of the residual [36], that is to find C_s such that:

$$C_s^2 = \frac{L_{ij}M_{ij}}{M_{ij}M_{ij}}. \tag{2.16}$$

A relevant problem associated with the local dynamic model (2.16), is that the coefficient field predicted by the local model varies strongly in space and may contain a significant fraction of negative values. The problem was dealt with by averaging terms in the equations for C^2 over directions of statistical homogeneity. Meneveau proposed to average over particle trajectories rather than over space and/or time.
The Lagrangian model is obtained by minimizing the error under the assumption that C_s does not vary along the fluid-particle Lagrangian trajectories. The total error is then defined as the pathline accumulation of the local error squared, it is minimized with respect to C^2, and the coefficient is determined as:

$$C_s^2 = \frac{\mathcal{I}_{LM}(\mathbf{x},t)}{\mathcal{I}_{MM}(\mathbf{x},t)} \tag{2.17}$$

where the numerator and denominator can be expressed by integrals arising from the minimization procedure. By adopting an exponential function as a weighting function (which corresponds to the idea of averaging over pathlines with an exponentially decreasing memory, see [41]), the integrals $\mathcal{I}_{LM}$, $\mathcal{I}_{MM}$ are solutions of the following transport equations:

$$\frac{\partial \mathcal{I}_{LM}}{\partial t} + \overline{u}_k \frac{\partial \mathcal{I}_{LM}}{\partial x_k} = \frac{1}{\mathrm{T}} \left(L_{ij}M_{ij} - \mathcal{I}_{LM} \right), \tag{2.18}$$

$$\frac{\partial \mathcal{I}_{MM}}{\partial t} + \overline{u}_k \frac{\partial \mathcal{I}_{MM}}{\partial x_k} = \frac{1}{\mathrm{T}} \left(M_{ij}M_{ij} - \mathcal{I}_{MM} \right). \tag{2.19}$$

The relaxation time-scale is assumed to be:

$$\mathrm{T} = \theta \overline{\Delta} (\mathcal{I}_{LM}\mathcal{I}_{MM})^{-1/8}, \quad \theta = 1.5, \tag{2.20}$$

after the analysis of Meneveau *et al.* [41].
In order to enforce the condition $C_s^2 \geq 0$, a numerical *clipping* is performed on factors $\mathcal{I}_{LM}$ and $\mathcal{I}_{MM}$: after the resolution of the partial differential equations (2.18,2.19), if $\mathcal{I}_{LM}$ assumes negative values in some points, in that points it is set to zero; if $\mathcal{I}_{MM}$ assumes negative values in some points, in that points it is set to very small positive value (since it is used as denominator, it cannot be set to zero).
For the sake of completeness, it can be pointed out that the numerical solutions of the partial differential equations (2.18,2.19) are not strictly necessary. An approximate solution is given by a sequence specified by recursion:

$$\begin{cases} \mathcal{I}_{LM}^{n+1}(\mathbf{x}) = \epsilon [L_{ij}M_{ij}]^{n+1}(\mathbf{x}) \; + \; (1-\epsilon) \cdot \mathcal{I}_{LM}^{n}(\mathbf{x} - \overline{\mathbf{u}}^n \Delta t) \\ \mathcal{I}_{LM}^{0}(\mathbf{x}) = C_{s,0} [M_{ij}M_{ij}]^{0}(\mathbf{x}) \end{cases} \tag{2.21}$$

where $c_{s,0} = 0.0256$ is a classical value for the Smagorinsky constant, and

$$\begin{cases} \mathcal{I}^{n+1}_{MM}(\mathbf{x}) = \epsilon[M_{ij}M_{ij}]^{n+1}(\mathbf{x}) + (1-\epsilon)\cdot\mathcal{I}^{n}_{MM}(\mathbf{x}-\overline{\mathbf{u}}^{n}\Delta t) \\ \mathcal{I}^{0}_{MM}(\mathbf{x}) = [M_{ij}M_{ij}]^{0}(\mathbf{x}) \end{cases} \tag{2.22}$$

with

$$\epsilon = \frac{\Delta t/^{n}}{1+\Delta t/\mathrm{T}^{n}}, \quad \mathrm{T}^{n} = \theta\,\overline{\Delta}(\mathcal{I}^{n}_{LM}\mathcal{I}^{n}_{MM})^{-1/8}.$$

We refer to Meneveau *et al.* [41] for a derivation and a physical interpretation of these alternative equations.

2.3 Acoustic analogies

The theory of aerodynamic sound is built upon the equations of mass and momentum conservation of a compressible fluid. Lighthill originally derived the wave equation applicable to free shear flows. Curle and then Ffowcs Williams and Hawkings extended this methodology to include stationary and moving surfaces, respectively, by incorporating additional forcing terms to the wave equation. The FW-H approach can be applied also for non-rigid or porous surfaces in motion that may encapsulate the noise-source flow region.
In this section, the derivation of the original Lighthill equation is briefly described in subsection 2.3.1. Then, the FW-H equation is reported omitting the details of its derivation in subsections 2.3.2. Finally the FW-H advective formulation is described in subsection 2.3.5 and details of the derivation are given in the last subsection 2.3.6.

2.3.1 Lighthill equation

Lighthill's famous manuscript begins as "A theory is initiated.." [35]. The author was initially interested in solving problem of sound produced by a turbulent nozzle flow. He obtained from the Navier-Stokes equations, governing the flow of a compressible viscous fluid, an exact, inhomogeneous wave equation whose source terms are important only within the turbulent region. He argued that sound is a small component of the whole motion, thus, once generated, its back-reaction on the main flow can be ignored.
The conservative form of the momentum equation (eq. (2.2)), omitting the gravitational force, can be rewritten as:

$$\frac{\partial(\rho u_i)}{\partial t} = -\frac{\partial \pi_{ij}}{\partial x_j}, \tag{2.23}$$

where $\pi_{ij} = \rho u_i u_j + (p-p_0)\delta_{ij} - \sigma_{ij}$, and $\sigma_{ij} = 2\mu(S_{ij} - \frac{1}{3}S_{kk}\delta ij)$. π_{ij} is called momentum flux tensor and the constant p_0 is inserted for convenience, it corresponds to the mean pressure the fluid has at infinity (where it is assumed to be at rest). In an ideal, linear acoustic medium, the momentum flux tensor contains only the pressure, and can be written in terms of density:

$$\pi_{ij} \to \pi^{0}_{ij} = (p-p_0)\delta_{ij} = c_0^2(\rho-\rho_0)\delta_{ij}, \tag{2.24}$$

thus, the momentum equation reduces to

$$\frac{\partial(\rho u_i)}{\partial t} + \frac{\partial}{\partial x_i}[c_0^2(\rho - \rho_0)] = 0. \tag{2.25}$$

Considering the time derivative of continuity equation (2.1) and spatial derivative of momentum flux equation (2.25) and summing them each other so as to eliminate the mixed term $\partial^2(\rho u_i)/\partial t \partial x_i)$, finally follows:

$$\left(\frac{1}{c_0^2}\frac{\partial^2}{\partial t^2} - \nabla\right)[c_0^2(\rho - \rho_0)] = 0, \tag{2.26}$$

which is the equation of linear acoustics satisfied by the perturbation density. Because the turbulence is neglected in this approximation and there are no externally applied forces or moving boundaries, the unique solution of this equation that satisfies the radiation condition of outgoing wave behavior is simply $\rho - \rho_0 = 0$. Eq. (2.23) can be rewritten as the momentum equation for an ideal, stationary acoustic medium of mean density ρ_0 and sound speed c_0 subject to the externally applied stress $\pi_{ij} - \pi_{ij}^0$:

$$\frac{\partial(\rho u_i)}{\partial t} = -\frac{\partial}{\partial x_j}(\pi_{ij} - \pi_{ij}^0). \tag{2.27}$$

The stress distribution

$$T_{ij} = \pi_{ij} - \pi_{ij}^0 = \rho u_i u_j + ((p - p_0) - c_0^2(\rho - \rho_0))\delta_{ij} - \sigma_{ij} \tag{2.28}$$

is called *Lighthill tensor* and the non-uniform wave equation that follows is named *Lighthill equation*:

$$\left(\frac{1}{c_0^2}\frac{\partial^2}{\partial t^2} - \nabla\right)[c_0^2(\rho - \rho_0)] = \frac{\partial^2 T_{ij}}{\partial x_i \partial x_j}. \tag{2.29}$$

The turbulence generated sound is interpreted as the radiating density (or pressure) disturbance into a stationary, ideal fluid produced by a distribution of quadrupole sources. The wave equation may be solved in an integral form, assuming that the density/pressure signal propagates in a uniform medium, thus by a convolution of the free-space Green's function with the source term of eq. (2.29) it follows:

$$\hat{p}(\mathbf{x}, t) = \frac{1}{4\pi}\frac{\partial^2}{\partial x_i \partial x_j}\int_{\mathbb{R}^3} \frac{T_{ij}(\mathbf{y}, t - |\mathbf{x} - \mathbf{y}|/c_0)}{|\mathbf{x} - \mathbf{y}|}\, d\mathbf{y}, \tag{2.30}$$

being $\hat{p} = c_0^2(\rho - \rho_0)$.

2.3.2 Ffowcs Williams and Hawkings equation

It was necessary to generalize the Lighthill's theory to account for the presence of solid bodies in the flow. Indeed, turbulence is frequently generated in the boundary layers and

wakes of flow past such bodies (airfoils, blades..), together with the unsteady surface forces (dipoles) make a significant (or even predominant) contribution to the production of sound. Curle [15] has derived a formal solution of Lighthill's equation (2.30) for the sound produced by turbulence in the presence of an arbitrary fixed surface.
Successively, Ffowcs Williams and Hawkings [18] developed the formulation in case of a moving rigid body immersed in a quiescent fluid and representing a discontinuity in the flow field. The differential form of the Ffowcs Williams and Hawkings equation reads as:

$$\begin{aligned}\left(\frac{1}{c_0^2}\frac{\partial^2}{\partial t^2}-\nabla\right)\left[H(f)\hat{p}\right] &= \frac{\partial}{\partial t}\{[\rho_0 v_n+\rho(u_n-v_n)]\,\delta(f)\} \\ &- \frac{\partial}{\partial x_i}\{[\tilde{p}\hat{n}_i+\rho u_i(u_n-v_n)]\,\delta(f)\}+\frac{\partial^2}{\partial x_i\partial x_j}[T_{ij}H(f)]\end{aligned} \tag{2.31}$$

where v_n is the velocity of the surface S projected along the outward normal to S (represented by the unit vector $\hat{\mathbf{n}}$), ρ is the density perturbation of the flow field from a reference value ρ_0 (note that for incompressible flows $\rho=\rho_0$), $\tilde{p}=p-p_0$ is the pressure distribution on the surface and the function f describes the surface:

$$S=\{\mathbf{x}: f(\mathbf{x},t)=0\}. \tag{2.32}$$

Moreover, the function f is such that $f(\mathbf{x},t)<0$ within S and $f(\mathbf{x},t)>0$ outside S. H and δ are the Heaviside and delta functions respectively, they indicate where the integration is defined. Specifically, if V is the volume outside the closed surface S, $H(f)=1$ for $\mathbf{x}\in V$ and $H(f)=0$ for $\mathbf{x}$ within S, while $\delta(f)\neq 0$ only for $\mathbf{x}\in S$ and $\nabla H=\nabla f\delta(f)=\mathbf{n}\delta(f)$. The common assumption is that $|\nabla f|=1$ and f is a smooth function, defined everywhere.

Observation. *The surface S may coincide with the body surface. In this case, equation (2.31) is referred to as FW-H direct formulation and it verifies $u_n=v_n$. Alternatively, the surface S may describe a not-physical surface, external to the body, often referred to as porous domain or control surface. In this case, the net flow across S is given by the difference $u_n-v_n\neq 0$.*

Note that the use of Dirac and Heaviside functions to limit the acoustic sources distribution to specific surfaces or fluid regions, from the point of view of mathematical formalism, leads to consider derivatives in the sense of distributions. However, many of the known properties of the classical derivative operator (i.e. limit of the incremental ratio) are retained also for the generalized functions and are not discussed in the thesis.

2.3.3 FW-H direct formulation

The differential form may be turned into an integral form by the convolution of the source term of eq. (2.31) with the free-space three-dimensional Green's function

$$G(\mathbf{x}-\mathbf{y},t-\tau)=\frac{\delta(t-\tau-|\mathbf{x}-\mathbf{y}|/c_0)}{4\pi|\mathbf{x}-\mathbf{y}|} \tag{2.33}$$

which is the solution of the wave equation (at observer point $(\mathbf{x},t)$) for an impulsive point source at $(\mathbf{y},\tau)$, the wave propagating in a uniform and three-dimensional free space, with velocity c_0. Recalling briefly the fundamentals of wave theory, if we denote with $q(\mathbf{x},t)$ the source term of a wave equation (which may be interpreted as a distribution of impulsive sources), the resulting pressure is given by

$$\begin{aligned} p(\mathbf{x},t) = q(\mathbf{x},t) * G(\mathbf{x},t) &= \int_{\mathbb{R}^3} \int_{-\infty}^{\infty} q(\mathbf{y},\tau) G(\mathbf{x}-\mathbf{y}, t-\tau)\, d\mathbf{y} d\tau \\ &= \int_{\mathbb{R}^3} \left[\frac{q(\mathbf{y},\tau)}{4\pi|\mathbf{x}-\mathbf{y}|} \right]_{\tau=t-|\mathbf{x}-\mathbf{y}|/c_0} d\mathbf{y}. \end{aligned}$$

Moreover, denoting $g = t - \tau - |\mathbf{x}-\mathbf{y}|/c_0$ and $r = |\mathbf{x}-\mathbf{y}|$, results:

$$\begin{aligned} \frac{\partial}{\partial x_i}\left[\frac{\delta(g)}{r}\right] &= \left[-\frac{\hat{r}_i}{c_0 r}\frac{\partial}{\partial t} - \frac{\hat{r}_i}{r^2}\right]\delta(g), \\ \frac{\partial^2}{\partial x_i \partial x_j}\left[\frac{\delta(g)}{r}\right] &= \left[\frac{1}{c_0^2}\frac{\hat{r}_i\hat{r}_j}{r}\frac{\partial^2}{\partial t^2} + \frac{1}{c_0}\frac{3\hat{r}_i\hat{r}_j - \delta_{ij}}{r^2}\frac{\partial}{\partial t} + \frac{3\hat{r}_i\hat{r}_j - \delta_{ij}}{r^3}\right]\delta(g). \end{aligned}$$

Considering the case of S corresponding to the solid surface of an immersed body, thus being verified the impermeability condition $u_n = v_n$, one of the possible integral solution of eq. (2.31) reads as:

$$\begin{aligned} 4\pi\hat{p}(\mathbf{x},t) &= \frac{\partial}{\partial t}\int_S \left[\frac{\rho_0 v_n}{r|1-M_r|}\right]_\tau dS + \frac{1}{c_0}\frac{\partial}{\partial t}\int_S \left[\frac{\tilde{p}\hat{n}_i\hat{r}_i}{r|1-M_r|}\right]_\tau dS \\ &+ \int_S \left[\frac{\tilde{p}\hat{n}_i\hat{r}_i}{r^2|1-M_r|}\right]_\tau dS + \frac{1}{c_0^2}\frac{\partial^2}{\partial t^2}\int_V \left[\frac{T_{rr}}{r|1-M_r|}\right]_\tau dV \\ &+ \frac{1}{c_0}\frac{\partial}{\partial t}\int_V \left[\frac{3T_{rr}-T_{ii}}{r^2|1-M_r|}\right]_\tau dV + \int_V \left[\frac{3T_{rr}-T_{ii}}{r^3|1-M_r|}\right]_\tau dV, \end{aligned} \tag{2.34}$$

being $r = |\mathbf{x}-\mathbf{y}|$ the source-observer distance, $\hat{\mathbf{r}} = (\mathbf{x}-\mathbf{y})/r$, $\hat{\mathbf{n}}$ the (outward) unit normal vector to the surface element dS, M_r is the Mach vector projected along $\hat{\mathbf{r}}$, $T_{rr} = T_{ij}\hat{r}_i\hat{r}_j$ and T_{ii} the trace of the Lighthill tensor, which, under the assumption of negligible viscous effects, constant flow density and iso-entropic transformations for the fluid in the acoustic field, reads as:

$$T_{ij} = \rho_0 u_i u_j + (p - p_0)\delta_{ij}.$$

The integral kernels in eq. (2.34) are computed at the emission time

$$\tau = t - r/c_0 = t + \frac{|\mathbf{x}(t) - \mathbf{y}(\tau)|}{c_0}. \tag{2.35}$$

τ is the instant at which the noise impulse starts at the source point $\mathbf{y}$, to reach the observer $\mathbf{x}$ at the observer time t. The difference between observer and emission time is known as

compressibility delay and points out that sound propagates in the fluid at a finite speed and sound waves may add up.
The first integral term of eq. (2.34) is known as *thickness noise* component. It represents the noise generated by the displacement of fluid mass caused by the motion of the body. Second and third terms in eq. (2.34) depend directly on the fluid dynamic load acting on S and for this reason they are identified as a *loading noise* component. Last three volume integrals are known as *quadrupole noise* component and take into account all the possible non linear sources occurring in the flow field.

2.3.4 FW-H porous formulation

Equation (2.31) was proposed by Ffowcs Williams and Hawkings in their original manuscript in 1969, but the idea of calculating the corresponding surface terms on a radiant domain external to the body was implemented later, see [17, 7]. By considering an external *porous* surface $S = S_p$ the flow is allowed across the discontinuity surface and the impermeability condition is not verified, meaning that $u_n \neq v_n$. Under this assumption and recombining the terms, the integral solution of 2.31 reads as:

$$\begin{aligned} 4\pi\hat{p}(\mathbf{x},t) &= \frac{\partial}{\partial t}\int_{S_p}\left[\frac{\rho_0 U_i \hat{n}_i}{r|1-M_r|}\right]_\tau dS_p \\ &+ \frac{1}{c_0}\frac{\partial}{\partial t}\int_{S_p}\left[\frac{L_{ij}\hat{n}_j\hat{r}_i}{r|1-M_r|}\right]_\tau dS_p + \int_{S_p}\left[\frac{L_{ij}\hat{n}_j\hat{r}_i}{r^2|1-M_r|}\right]_\tau dS_p + \hat{p}_{3D}. \end{aligned} \tag{2.36}$$

being

$$\begin{aligned} U_i &= \left(1-\frac{\rho}{\rho_0}\right)v_i + \frac{\rho}{\rho_0}u_i, \\ L_{ij} &= [\rho_0 u_i\,(u_j - v_j) + P_{ij}], \end{aligned}$$

where $P_{ij} = (p-p_0)\delta_{ij} - \sigma_{ij}$ is the compressive stress tensor, with $p - p_0$ the flow pressure perturbation with respect to the reference value p_0, σ_{ij} the viscous stress tensor and δ_{ij} the Kronecker delta. Last term $\hat{p}_{3D}$ refers to a volume integration which should be evaluated on the region external to the porous surface S_p. It would account for the possible noise sources present outside S_p and consists of the volume integrals that appear in equation (2.34). Generally, the control surface S_p is chosen wide enough so as to embed all the noise sources present in the flow, making the contribution of $\hat{p}_{3D}$ negligible.

2.3.5 Advective FW-H formulation

When the background fluid moves at a constant and uniform speed the solving formulation has to be derived from the convective form of the governing equation. A clear derivation of the convective FW-H equation is reported in the paper of Najafi-Yazdi *et al.* [43], where the authors developed an integral solving formulation for the linear (surface) terms, validated it for a monopole (stationary and rotating) and a dipole in a moving medium, and

gave a detailed description of the "wind–tunnel" problem herein investigated, where both the source and the observer are at rest. Note that in that paper (as well as in most papers focused on the use of the FW-H equation), the nonlinear volume term (i.e. rhs:last component of eq. 2.31) was not included in the solving formulation, since the authors assumed its contribution to be negligible or, eventually, assessable through the porous formulation. Here, first in literature, we derive the advective formulation of the volume term for the particular case of the wind tunnel flow.
By the use of the free–space Green's function for the convective wave equation (see Blokhintsev [5]), it is possible to derive an integral form of the FW-H equation, where the acoustic pressure $\hat{p}$, at any point $\mathbf{x}$ and time t, is represented by the sum of surface ($\hat{p}_{2D}$) and volume integrals ($\hat{p}_{3D}$). Under the assumption of a fixed-in-space body and considering an uniform flow with velocity U_0 along the direction x_1 the surface terms may be written [43] as

$$\begin{aligned} 4\pi\hat{p}_{2D}(\mathbf{x},t) &= \frac{\partial}{\partial t}\int_{f=0}\left[(1-M_0\hat{r}_1)\frac{\rho_0 u_i\hat{n}_i}{r^*|1-M_r|}\right]_\tau dS - U_0\int_{f=0}\left[\frac{\rho_0 u_i\hat{n}_i\hat{r}_1^*}{r^{*2}|1-M_r|}\right]_\tau dS \\ &+ \frac{1}{c_0}\frac{\partial}{\partial t}\int_{f=0}\left[\frac{L_{ij}^*\hat{n}_j\hat{r}_i}{r^*|1-M_r|}\right]_\tau dS + \int_{f=0}\left[\frac{L_{ij}^*\hat{n}_j\hat{r}_i^*}{r^{*2}|1-M_r|}\right]_\tau dS, \end{aligned} \tag{2.37}$$

u_i indicates the i component of the fluid perturbation velocity $\mathbf{u}$, $\hat{r}$ and $\hat{r}^*$ are unit radiation vectors (see next section 2.3.6), the appearance of their first components $\hat{r}_1$ and $\hat{r}_1^*$ is due to the mean flow which advects the pressure acoustic field along the x-axis direction, r and r^* are the module of the radiation vectors $\mathbf{r}$ and $\mathbf{r}^*$ respectively, $M_0 = U_0/c_0$ is the inlet Mach number and c_0 is the sound speed.
The tensor L_{ij}^* appearing in (2.37) is given by

$$L_{ij}^* = [\rho_0 u_i\,(u_j + U_0\delta_{1j} - v_j) + P_{ij}],$$

The volume integrals assume the form

$$\begin{aligned} 4\pi\hat{p}_{3D}(\mathbf{x},t) &= \frac{1}{c_0^2}\frac{\partial^2}{\partial t^2}\int_{f>0}\left\{T_{ij}\left[\frac{\hat{r}_i\hat{r}_j}{r^*|1-M_r|}\right]\right\}_\tau dV \\ &+ \frac{1}{c_0}\frac{\partial}{\partial t}\int_{f>0}\left\{T_{ij}\left[\frac{2\hat{r}_i\hat{r}_j^*}{r^{*2}} + \frac{\hat{r}_i^*\hat{r}_j^* - R_{ij}^*}{\beta^2 r^{*2}|1-M_r|}\right]\right\}_\tau dV \\ &+ \int_{f>0}\left\{T_{ij}\left[\frac{3\hat{r}_i^*\hat{r}_j^* - R_{ij}^*}{r^{*3}|1-M_r|}\right]\right\}_\tau dV. \end{aligned} \tag{2.38}$$

Equation (2.38) contains the second–order tensors R_{ij}^* which is described in the next section. It is worth noting that, to the best of our knowledge, equation (2.38) has never been formulated in previous work.
Once again, particular attention has to be paid to the meaning of function f, representing the integration domain. The points in space such that $f(\mathbf{x},t) = 0$ may describe a surface S coincident with the surface of the body–source or, alternatively, a closed (porous) surface S_p, embedding the body together with a fluid region around it, acting as a radiating

domain. In the former case, the impermeability condition ($u_n = v_n$) and the assumption of a fixed-in-space body ($\mathbf{v} = 0$), reduce the pressure term $\hat{p}_{2D}$ to the advective Curle formulation:

$$4\pi\hat{p}_{2D}(\mathbf{x},t) = \frac{1}{c_0}\frac{\partial}{\partial t}\int_S \left[\frac{\tilde{p}\hat{n}_i\hat{r}_i}{r^*}\right]_\tau dS + \int_S \left[\frac{\tilde{p}\hat{n}_i\hat{r}_i^*}{r^{*2}}\right]_\tau dS \tag{2.39}$$

On the contrary, in the latter case, the domain should embed the body and "all" possible flow noise sources, in such a way to make the contribution of $\hat{p}_{3D}(\mathbf{x},t)$ (now evaluated over a volume external to S_p) equal to zero.

2.3.6 Advective FW-H equation - Derivation of nonlinear terms

In this section we report some details about the mathematical manipulation of the convective FW-H equation and, in particular, the procedure which allows to write down the integral form of the nonlinear terms (2.38). The convective FW-H equation may be easily obtained from the conservation laws of mass and momentum, by accounting for the presence of a medium moving at a constant velocity $\mathbf{U}_0$; then, at each point, the fluid velocity is $\mathbf{U}_0 + \mathbf{u}$, being $\mathbf{u}$ the local perturbation velocity, and the equation reads [43]

$$\Box_C^2\hat{p}(\mathbf{x},t) = \left(\frac{\partial}{\partial t} + U_{0j}\frac{\partial}{\partial x_j}\right)[Q_k\hat{n}_k\delta(f)] - \frac{\partial}{\partial x_i}[L_{ij}\hat{n}_j\delta(f)] + \frac{\partial^2}{\partial x_i\partial x_j}[T_{ij}H(f)] \tag{2.40}$$

where all derivatives have to be accounted for in a "generalized" sense, being $\delta(f)$ and $H(f)$ the Dirac and Heaviside functions, respectively, and

$$\Box_C^2 = \left[\frac{\partial^2}{\partial t^2} - c_0^2\frac{\partial^2}{\partial x_i\partial x_j} + 2U_{0j}\frac{\partial^2}{\partial t\partial x_j} + U_{0i}U_{0j}\frac{\partial^2}{\partial x_i\partial x_j}\right]$$

represents the convective form of the D'Alembert operator. Furthermore

$$\begin{aligned} Q_k &= [\rho\,(u_k + U_{0k} - v_k) + \rho_0\,(v_k - U_{0k})] \\ L_{ij} &= [\rho u_i\,(u_j + U_{0j} - v_j) + P_{ij}] \\ T_{ij} &= \left[\rho u_i u_j + P_{ij} - c_0^2\tilde{\rho}\delta_{ij}\right] \end{aligned}$$

where P_{ij} is the compressive stress tensor, $\tilde{\rho}$ the perturbation density, c_0 the sound speed and δ_{ij} the Kronecker delta. Without loss of generality, it can be assumed that the mean flow velocity $\mathbf{U}_0$ is along the positive x_1-direction. By using the convective form of the free-space Green's function

$$G(\mathbf{x},t;\mathbf{y},\tau) = \frac{\delta(g)}{4\pi r^*} \qquad \text{with} \qquad g = \tau - t + \frac{r}{c_0},$$

where $(\mathbf{x},t)$ and $(\mathbf{y},\tau)$ are the observer and source position and time, respectively, and

$$\begin{aligned} r^* &= \sqrt{(x_1-y_1)^2 + \beta^2\left[(x_2-y_2)^2 + (x_3-y_3)^2\right]}, \\ r &= \frac{-M_0\,(x_1-y_1) + r^*}{\beta^2}, \qquad \beta = \sqrt{1-M_0^2} \end{aligned} \tag{2.41}$$

with the components of the unit radiant vectors given by

$$\hat{r}_1^* = \frac{(x_1 - y_1)}{r^*}\,, \quad \hat{r}_2^* = \beta^2 \frac{(x_2 - y_2)}{r^*}\,, \quad \hat{r}_3^* = \beta^2 \frac{(x_3 - y_3)}{r^*} \tag{2.42}$$

and

$$\hat{r}_1 = -\frac{M_0}{\beta^2} + \frac{1}{\beta^2}\frac{(x_1 - y_1)}{r^*} \quad , \quad \hat{r}_2 = \frac{(x_2 - y_2)}{r^*} \quad , \quad \hat{r}_3 = \frac{(x_3 - y_3)}{r^*} \quad , \tag{2.43}$$

equation (2.40) may be turned into an integral form. The first two source terms on the right–hand–side give rise to the surface integrals of equation (2.37) and the procedure is described in detail in [43]. An analogous transformation may be carried out on the third (quadrupole) term, which, in essence, requires the manipulation of the double spatial derivative of the Green function

$$\frac{\partial^2}{\partial x_i \partial x_j}\left[\frac{\delta(g)}{r^*}\right]$$

Starting from

$$\frac{\partial}{\partial x_i}\left[\frac{\delta(g)}{r^*}\right] = -\frac{\hat{r}_i}{c_0 r^*}\frac{\partial}{\partial t}\left[\delta(g)\right] - \frac{\hat{r}_i^*}{r^{*2}}\delta(g)$$

we have

$$\begin{aligned}
\frac{\partial}{\partial x_j}\left\{\frac{\partial}{\partial x_i}\left[\frac{\delta(g)}{r^*}\right]\right\} &= \frac{\partial}{\partial x_j}\left\{-\frac{1}{c_0}\frac{\hat{r}_i}{r^*}\frac{\partial}{\partial t}\left[\delta(g)\right] - \frac{\hat{r}_i^*}{r^{*2}}\delta(g)\right\} = \\
&- \frac{1}{c_0}\frac{\partial}{\partial x_j}\left[\frac{\hat{r}_i}{r^*}\right]\cdot\left\{\frac{\partial}{\partial t}\left[\delta(g)\right]\right\} - \frac{1}{c_0}\frac{\hat{r}_i}{r^*}\cdot\left\{\frac{\partial}{\partial x_j}\left(\frac{\partial}{\partial t}\left[\delta(g)\right]\right)\right\} \\
&- \frac{\partial}{\partial x_j}\left[\frac{\hat{r}_i^*}{r^{*2}}\right]\cdot\left\{\delta(g)\right\} - \frac{\hat{r}_i^*}{r^{*2}}\cdot\left\{\frac{\partial}{\partial x_j}\left[\delta(g)\right]\right\}
\end{aligned}$$

From the relations

$$\begin{aligned}
\frac{\partial}{\partial x_j}\left[\frac{\hat{r}_i}{r^*}\right] &= -\frac{1}{r^*}\frac{\partial \hat{r}_i}{\partial x_j} - \frac{\hat{r}_i \hat{r}_j^*}{r^{*2}} \\
\frac{\partial}{\partial x_j}\left(\frac{\partial}{\partial t}\left[\delta(g)\right]\right) &= -\frac{\hat{r}_j}{c_0}\frac{\partial^2}{\partial t^2}\left[\delta(g)\right] \\
\frac{\partial}{\partial x_j}\left[\frac{\hat{r}_i^*}{r^{*2}}\right] &= \frac{1}{r^{*2}}\frac{\partial \hat{r}_i^*}{\partial x_j} - 2\frac{\hat{r}_i^* \hat{r}_j^*}{r^{*3}} \\
\frac{\partial}{\partial x_j}\left[\delta(g)\right] &= -\frac{\hat{r}_j}{c_0}\frac{\partial}{\partial t}\left[\delta(g)\right]
\end{aligned}$$

we obtain

$$\frac{\partial^2}{\partial x_i \partial x_j}\left[\frac{\delta(g)}{r^*}\right] = \frac{1}{c_0^2}\frac{\hat{r}_i \hat{r}_j}{r^*}\frac{\partial^2}{\partial t^2}\left[\delta(g)\right] + \frac{1}{c_0}\left[\frac{2\hat{r}_i \hat{r}_j^*}{r^{*2}} - \frac{1}{r^*}\frac{\partial \hat{r}_i}{\partial x_j}\right]\frac{\partial}{\partial t}\left[\delta(g)\right] + \left[\frac{2\hat{r}_i^* \hat{r}_j^*}{r^{*3}} - \frac{1}{r^{*2}}\frac{\partial \hat{r}_i^*}{\partial x_j}\right]\delta(g) \tag{2.44}$$

Concerning the spatial derivative of $\hat{r}_i^*$, we have

$$\begin{aligned}\frac{\partial \hat{r}_i^*}{\partial x_j} &= \frac{\partial}{\partial x_j}\left[\frac{r_i^*}{r^*}\right] = \frac{1}{r^*}\frac{\partial r_i^*}{\partial x_j} - \frac{r_i^*}{r^{*2}}\frac{\partial r^*}{\partial x_j} = \frac{1}{r^*}\frac{\partial r_i^*}{\partial x_j} - \frac{\hat{r}_i^*\hat{r}_j^*}{r^*} \\ &= \frac{1}{r^*}\begin{bmatrix}1 & 0 & 0\\ 0 & \beta^2 & 0\\ 0 & 0 & \beta^2\end{bmatrix} - \frac{\hat{r}_i^*\hat{r}_j^*}{r^*} = \frac{1}{r^*}\left[R_{ij}^* - \hat{r}_i^*\hat{r}_j^*\right] \end{aligned} \tag{2.45}$$

where we have set

$$R_{ij}^* = \begin{bmatrix}1 & 0 & 0\\ 0 & \beta^2 & 0\\ 0 & 0 & \beta^2\end{bmatrix}$$

On the other hand, by reminding (2.42) and (2.43), it is easy to see

$$\hat{r}_1 = -\frac{M_0}{\beta^2} + \frac{1}{\beta^2}\hat{r}_1^* \quad ; \quad \hat{r}_2 = \frac{1}{\beta^2}\hat{r}_2^* \quad ; \quad \hat{r}_3 = \frac{1}{\beta^2}\hat{r}_3^*$$

so that

$$\frac{\partial \hat{\mathbf{r}}}{\partial x_j} = \frac{1}{\beta^2}\frac{\partial \hat{\mathbf{r}}^*}{\partial x_j} = \frac{1}{\beta^2 r^*}\left[R_{ij}^* - \hat{r}_i^*\hat{r}_j^*\right]$$

Finally, equation (2.44) reads

$$\begin{aligned}\frac{\partial^2}{\partial x_i \partial x_j}\left[\frac{\delta(g)}{r^*}\right] &= +\frac{1}{c_0^2}\frac{\hat{r}_i\hat{r}_j}{r^*}\frac{\partial^2}{\partial t^2}\left[\delta(g)\right] \\ &+ \frac{1}{c_0}\left[\frac{2\hat{r}_i\hat{r}_j^*}{r^{*2}} + \frac{1}{\beta^2 r^{*2}}\left(\hat{r}_i^*\hat{r}_j^* - R_{ij}^*\right)\right]\frac{\partial}{\partial t}\left[\delta(g)\right] \\ &+ \left[\frac{3\hat{r}_i^*\hat{r}_j^* - R_{ij}^*}{r^{*3}}\right]\delta(g)\end{aligned} \tag{2.46}$$

To obtain eq. (2.38) one needs to consider integration for parts to in order to move the derivative operator on the Green's function, considering that the Lighthill tensor (and its gradient) is null on the boundary of the open set $\Omega = \{\mathbf{x} : f(\mathbf{x}, t) > 0\}$.
It's worth pointing out that under the assumption $M_0 << 1$ we have $\beta \approx 1$ and, consequently, $r = r^*$, $R_{ij}^* = \delta_{ij}$; then, equation (2.46) reduces to the classical form

$$\frac{\partial^2}{\partial x_i \partial x_j}\left[\frac{\delta(g)}{r}\right] = +\frac{1}{c_0^2}\frac{\hat{r}_i\hat{r}_j}{r}\frac{\partial^2}{\partial t^2}\left[\delta(g)\right] + \frac{1}{c_0}\left[\frac{3\hat{r}_i\hat{r}_j - \delta_{ij}}{r^2}\right]\frac{\partial}{\partial t}\left[\delta(g)\right] + \left[\frac{3\hat{r}_i\hat{r}_j - \delta_{ij}}{r^3}\right]\delta(g)$$

The product of equation (2.46) by the Lighthill tensor T_{ij} exactly gives rise to the integral kernels of equation (2.38).

Chapter 3

Assessment of FW-H solution methodologies

In this chapter the important role of the time delays occurring in the FW-H integral formulation is first discussed in section 3.1. Second section 3.2 deals with a well-known vortex-crossing problem related to the positioning of the porous domain. The following results may also be regarded as validation of the FW-H formulations involved.

3.1 Compressibility delays

In this section the FW-H porous formulation is tested for the simple case of a monopole acoustic field. The aim is to point out the dependence of the solution from the computation of the time delays. The following arguments apply to wind-tunnel cases where there is a flow around a stationary object. The need to emphasize the (not essential) role of the time delays lies in the fact that their calculation makes the acoustic post-processing extremely longer and more complex and in the case of volume integration, even unaffordable. In fact, the procedure consists of storing all the source data (pressure and velocity fields of the fluid flow) for each emission time τ. Then, a data fitting is performed over all the data to get the acoustic signal at the observer time t. The assumption that the source impulses propagate without overlapping (in time) would avoid the calculation of time delays. This assumption, as we will see, is only valid if certain (high) frequencies are no needed to be considered and can be filtered out.
According to the FW-H integral formulation, the acoustic pressure $\hat{p}$, evaluated at any point $\mathbf{x}$ and time t, results as sum of integrals, whose kernels are evaluated at the emission time τ. In particular, the porous formulation (eq. (2.36)), to highlight the role of variables $t, \tau, \mathbf{x}, \mathbf{y}$, may be synthesized as :

$$\hat{p}(\mathbf{x}, t) = \int_{S_p} [\cdots]_\tau \, dS_p(\mathbf{y}) \tag{3.1}$$

where $\tau = t - |\mathbf{x} - \mathbf{y}|/c_0$ [we omitted the dependence of $\mathbf{x}$ and $\mathbf{y}$ from t and τ respectively

because we analyze the case in which the distance source-observer $r = |\mathbf{x} - \mathbf{y}|$ is constant in time].
As known, S_p is the porous surface, where the noise sources are collected. If S_p is "small", the source is said to be *compact*. More specifically, the source is compact if $L << k$, being L the length of the source and k the wavelength corresponding to the speed of sound of the medium c_0.
In the following paragraphs different size of S_p are tested at constant c_0, for the simple case of a monopole acoustic field.

3.1.1 Radiation from a sphere - monopole

A monopole is a pressure field generated by a pulsating sphere. The pressure field is constant in the radial direction and may be represented by harmonic waves of angular frequency $\omega = 2\pi f$ traveling outward from the origin (starting at time $t_0 = 0$):

$$p(r,t) = \frac{i\rho_0 c_0 k Q}{4\pi r} e^{-i(\omega t - kr)}, \tag{3.2}$$

where Q is termed the *strength of an omni-directional (monopole) source* situated at the origin, and $Q = \frac{p_I 4\pi}{\rho_0 c_0 k}$, being p_I the sound pressure amplitude. We consider the real part of eq. (3.2) obtaining a sine wave. The radial particle velocity $u_r(r,t)$ in a spherically spreading sound field is given by Euler's equation as

$$u_r(r,t) = -\frac{1}{\rho_0} \int \frac{\partial p(r,t)}{\partial r} dt. \tag{3.3}$$

The porous domain S_p here considered is a sphere of radius R, discretized using 300×150 points in the angular directions $\varphi \times \theta$. The outward normal to the sphere surface is given by the standard spherical coordinates

$$\begin{aligned} \hat{n}_x &= \sin(\varphi)\cos(\theta) \\ \hat{n}_y &= \sin(\varphi)\sin(\theta) \\ \hat{n}_z &= \cos(\varphi) \end{aligned}$$

with $\varphi \in [0, \pi]$ and $\theta \in [0, 2\pi)$. The monopole field (eq. (3.2)) is evaluated on the porous surface S_p in order to provide source field data. The same equation offers an analytical solution which is evaluated at point $\mathbf{x}_{mic} = (100, 0, 0)$ as a reference pressure. Due to the spherical symmetry of the problem, every point of the space at a certain distance from the origin, is equivalent. We set $c_0 = 300\, m/s$.
As a first case a wave frequency equal to $f = 1\, Hz$ is considered, data (p and u_r) on a sphere of radius $R = 0.1\, m$ are collected with a time step $dt = 0.01\, s$, on a period $T = 600 \times dt\, s$. [Hereafter when the measure unit are omitted, we assume that the lengths are in meters, the time intervals in seconds and the frequencies in Hertz]. The porous formulation is considered both with the account of the time delays (referred to as $Por\_delayON$) and without computing them (referred to as $Por\_delayOFF$). Figure 3.1 shows a clear overlap of the two reconstructed signals with the analytical solution.

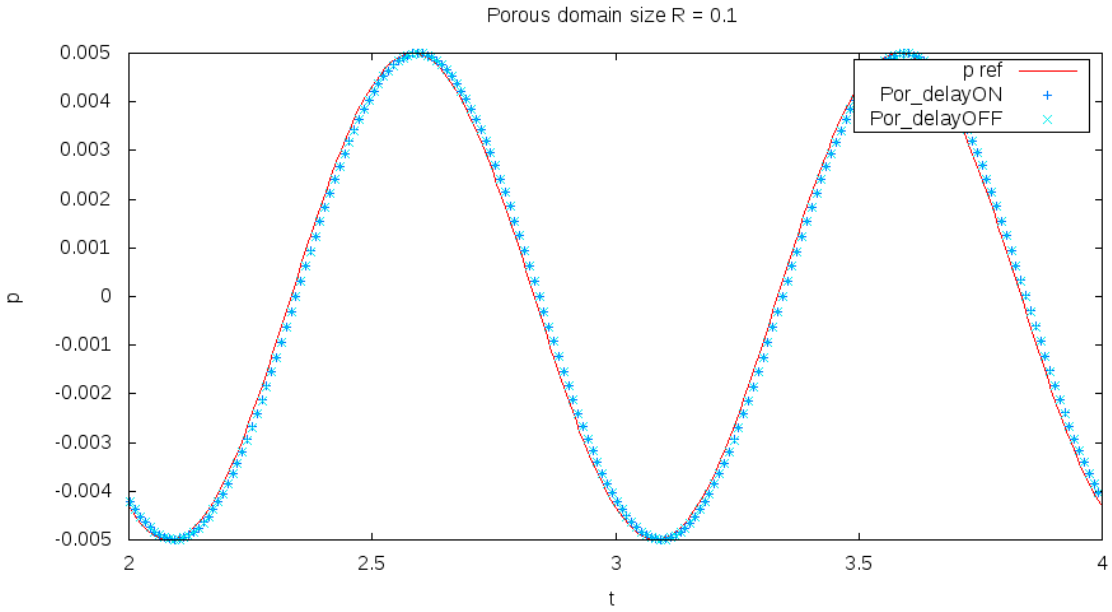

Figure 3.1: Comparison of a monopole pressure field (*p ref*) with time solution of FW-H porous formulation, in case of time delays computation activated *Por_delayON* and deactivated *Por_delayOFF*. The spherical porous domain has radius $R = 0.1$.

The agreement between *Por_delayON* and *Por_delayOFF* was expected. It is possible to generalize this event by saying that the time delays computation is needed only when

$$\frac{1}{\Delta_{del}} > f \tag{3.4}$$

Being

$$\Delta_{del} = \frac{\max\limits_{\mathbf{y}\in S_p} |\mathbf{y} - \mathbf{x}_{mic}| - \min\limits_{\mathbf{y}\in S_p} |\mathbf{y} - \mathbf{x}_{mic}|}{c_0}, \tag{3.5}$$

and f the higher frequency at which the fluid dynamic phenomena is observed. Note that if dt is the time step at which the fluid dynamic data are stored, frequency higher than $1/dt$ are filtered out.
Thus, by omitting the time delays computation, only the frequencies higher than $1/\Delta_{del}$ are erroneously reproduced.
In the present case of a spherical porous domain $\Delta_{del} = 2R/c_0$, for any point $\mathbf{x}_{mic}$. The previous radius and time step considered (0.1 and 0.01 respectively) do not satisfy eq. (3.4), thus the time delays computation is not essential. In practice, the source size is small enough with respect to the propagation velocity that the pressure radiates from the porous domain as simultaneous (compared to the observation time step) impulses.
Whether the radius of the porous domain increase up to $R = 1$, results do not change, see figure 3.2. In fact, still $\Delta_{del} = 2R/c_0 \approx 0.0066 < dt = 0.01$.

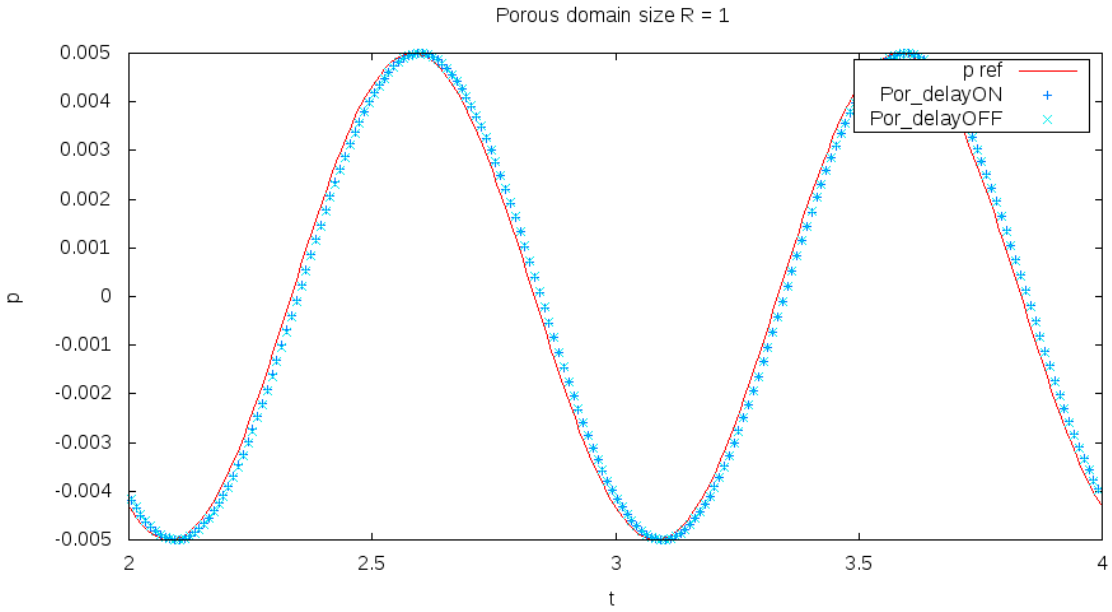

Figure 3.2: Comparison of a monopole pressure field (*p ref*) with time solution of FW-H porous formulation, in case of time delays computation activated $Por\_delayON$ and deactivated $Por\_delayOFF$. The spherical porous domain has radius $R = 1$.

The time delays, for $R = 1$, should be significant at frequencies $f > 1/0.0066 \approx 150\,Hz$. To verify this statement we may consider a pressure signal p consisting of two frequencies, a low frequency $f_l < 150\,Hz$ and a higher one $f_h > 150\,Hz$. A radial pressure field, combined of two angular frequencies, may read as:

$$p(r,t) = \frac{p_{I_l}}{4\pi r}\sin(\omega_l t - k_l r) + \frac{p_{I_h}}{4\pi r}\sin(\omega_h t - k_h r) \tag{3.6}$$

where $\omega_l = 2\pi f_l$ and $\omega_h = 2\pi f_h$, $k_l = \omega_l/c_0$ and $k_h = \omega_h/c_0$. The pressure amplitudes for the lower-frequency and the higher-frequency monopole where chosen to be respectively constant $p_{I_l} = 1$ and $p_{I_h} = 0.1$.
The pressure p, reconstructed at $\mathbf{x}_{mic}$, is shown in figure 3.3 together with the two decomposed signals, related to the two frequencies f_l and f_h. Two different double-frequency monopoles are tested, first case (top panel in figure 3.3) is composed by $f_l = 1Hz$ and $f_h = 40Hz$ and we referred to as HF signal. The second case (bottom panel in figure 3.3) is composed by $f_l = 10Hz$ and $f_h = 400Hz$, and we referred to as HHF signal.
For the reasoning above, in the first case the signals $Por\_delayON$ and $Por\_delayOFF$ still overlap. In fact both frequencies, f_l and f_h, are below the threshold of $150Hz$. Results for the HF signal case are in figure 3.4. In the second case (HHF) the signal $Por\_delayOFF$ is not able to reproduce correctly the higher frequency $f_h = 400Hz$, as shown in figure 3.5 (bottom panel) while the standard FW-H integration, with the complete calculation of

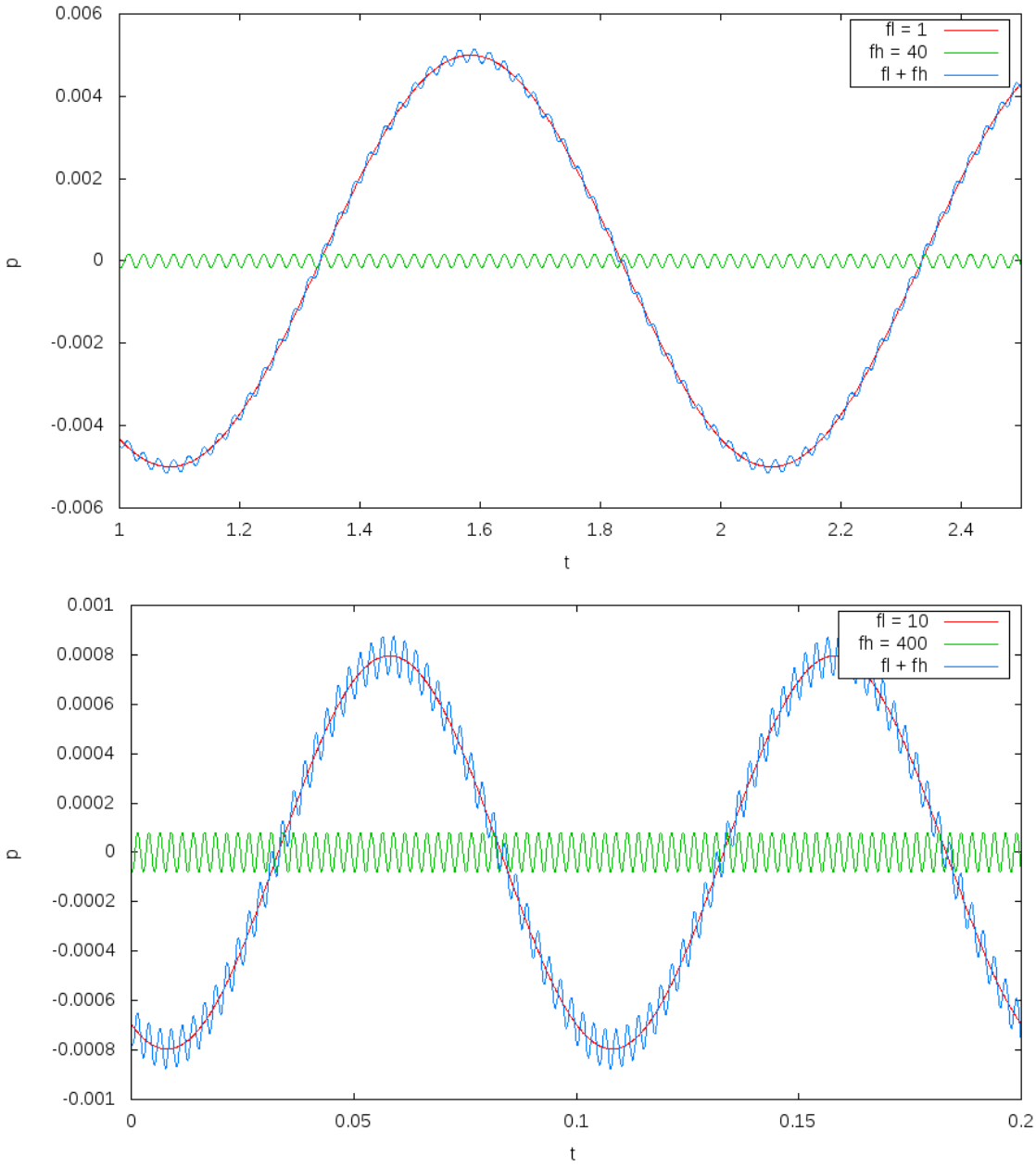

Figure 3.3: Time evolution of a monopole combined of two frequencies fl and fh. Top panel $f_l = 1Hz$ and $f_h = 40Hz$, referred to as HF signal. Bottom panel $f_l = 10Hz$ and $f_h = 400Hz$, referred to as HHF signal.

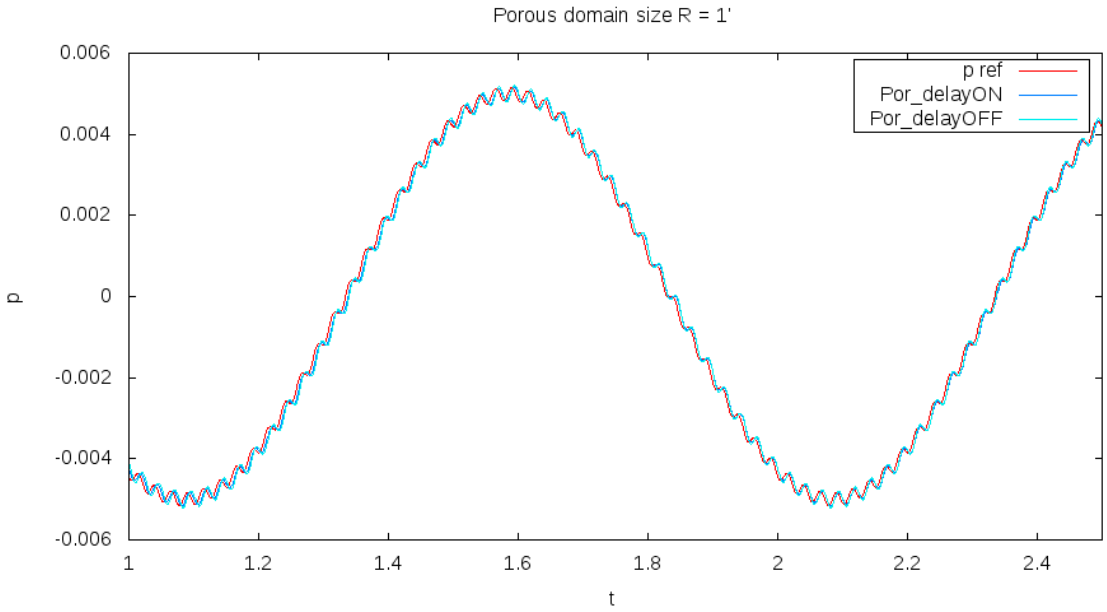

Figure 3.4: Comparison of a monopole pressure field (*p ref*) with time solution of FW-H porous formulation, in case of time delays computation activated $Por\_delayON$ and deactivated $Por\_delayOFF$. The spherical porous domain has radius $R = 1$. Reproduction of the HF signal. The spherical porous domain has radius $R = 1$.

delays ($Por\_delayOFF$ top panel), is in agreement with the analytical solution *p ref*.
As a further prove, we lower the Δ_{del} by decreasing the radius of the porous domain, making the source more compact. The choice of a radius $R = 0.1$ is adequate, in fact $\Delta_{del} = 0.2/c0 = 0.00066$ thus $1/\Delta_{del} \approx 1500Hz$. It means that the solution of the FW-H equation without time delays, on a porous domain of this size, can provide a correct signal up to $1500\,Hz$. The results are in figure 3.6.
As a last remark, we may emphasize that the considerations just made regarding the time delays for the integration on a porous domain apply to the volume integrals of the standard FW-H formulation, whether the volume is enclosed on the porous surface.
In figure 3.7 the response of the direct FW-H formulation is showed, time delays were not considered in the reconstruction of the signal. It must be said that in the acoustic field generated by a pulsating sphere there are no shear forces acting on the volume, thus, the contribution of the FW-H volume integrals is negligible. The signal in figure 3.7 is then to be attributed to the thickness term contribution. The monopole acoustic field would not be a good example to test the direct formulation.

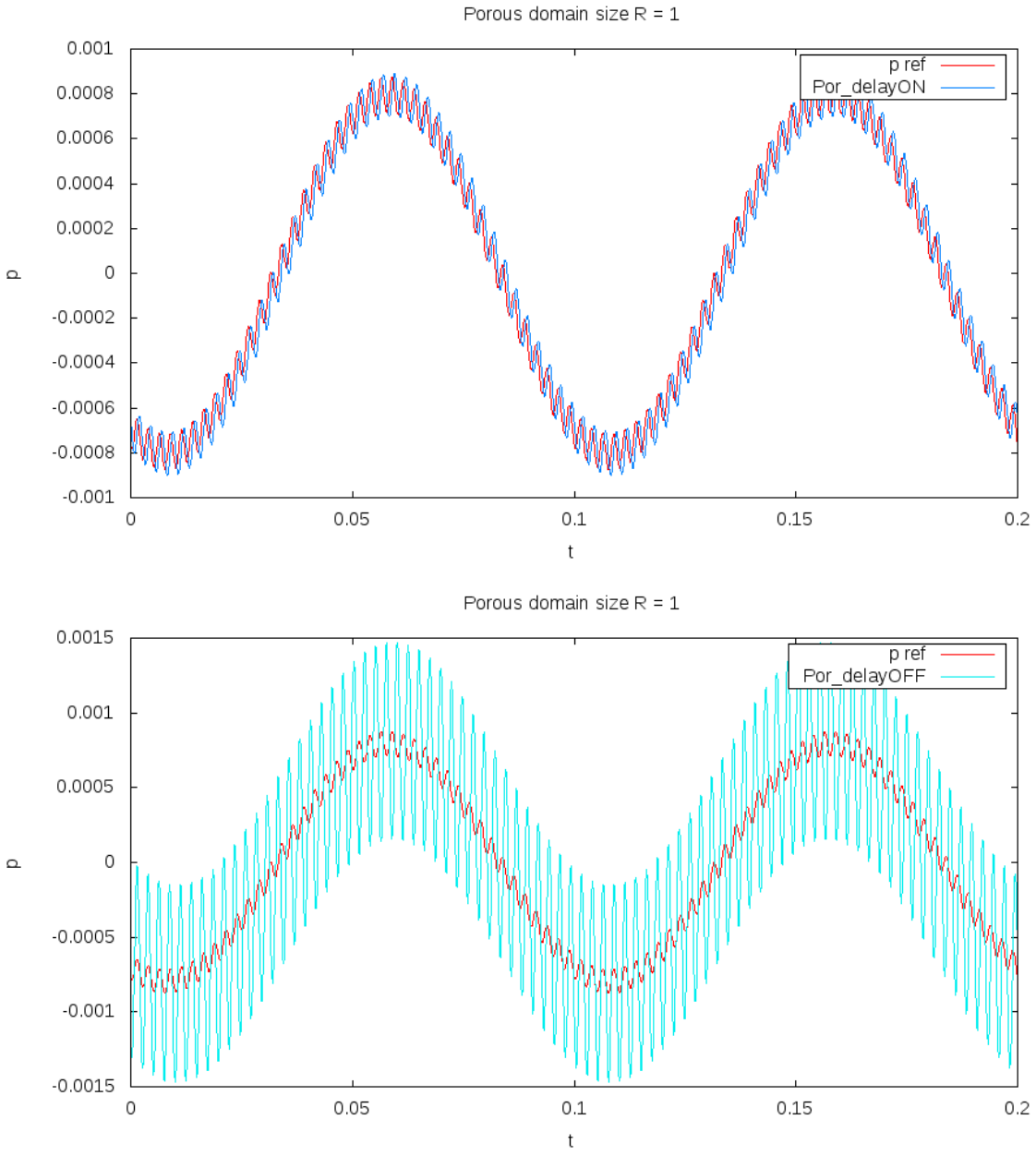

Figure 3.5: Comparison of a monopole pressure field (p *ref*) with time solution of FW-H porous formulation, in case of time delays computation activated $Por\_delayON$ (top panel) and deactivated $Por\_delayOFF$ (bottom panel). The spherical porous domain has radius $R = 1$. Reproduction of the HHF signal. The spherical porous domain has radius $R = 1$.

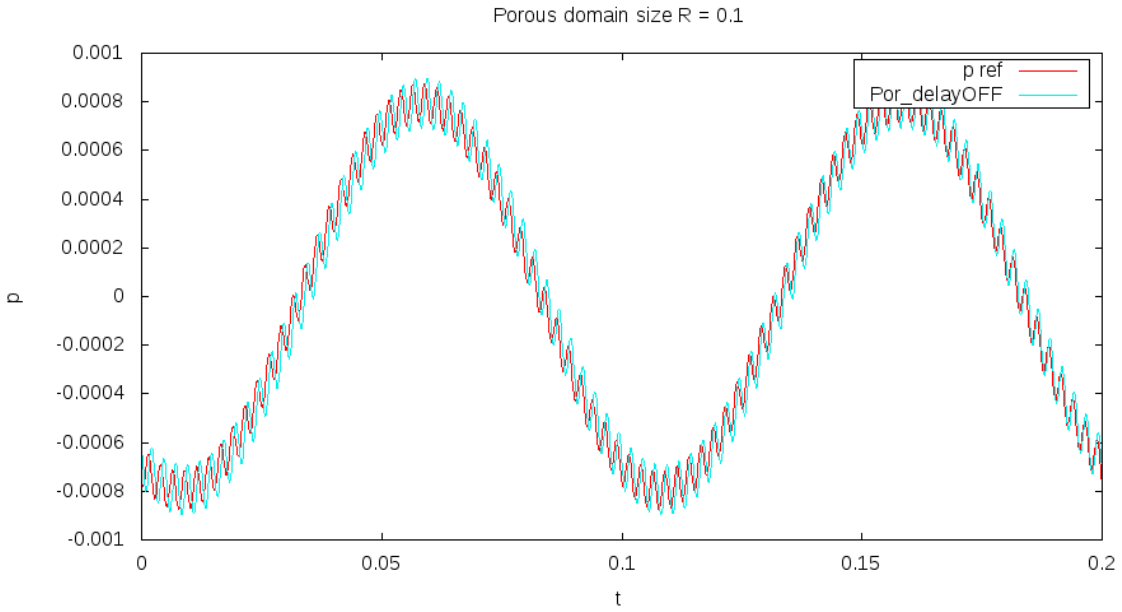

Figure 3.6: Comparison of a monopole pressure field (*p ref*) with time solution of FW-H porous formulation, in case of time delays computation deactivated $Por\_delayOFF$. Reproduction of the HHF signal. The spherical porous domain has radius $R = 0.1$.

3.2 Advected vortex

In recent numerical experiments ([44]; [37]), spurious signals are showed to affect the FW-H acoustic solution when the porous surface is immersed in a high vorticous flow. In literature, to avoid the erroneous response of the FW-H integration, some corrections to the porous formulation were proposed. The alternative, commonly adopted in literature, is to place the porous domain in a region where the vorticity of the flow results negligible. In the case of a vorticous wake persisting downstream, the "outlet" side of the porous domain is avoided, so as to have an open domain of integration.
In this section a two-dimensional potential vortex is reproduced, in order to investigate on the effect of the passage of a vortex through the boundaries of the acoustic integration domain. In particular, the spurious signal is noticed at the passage of the vortex through the porous domain, while a considerable difference is observed and justified in the case of the volume integration method.

3.2.1 Potential advected vortex

The two-dimensional incompressible potential vortex is initially centered at (x_0, y_0), and is advected by a uniform and constant velocity U. The velocity potential is given by

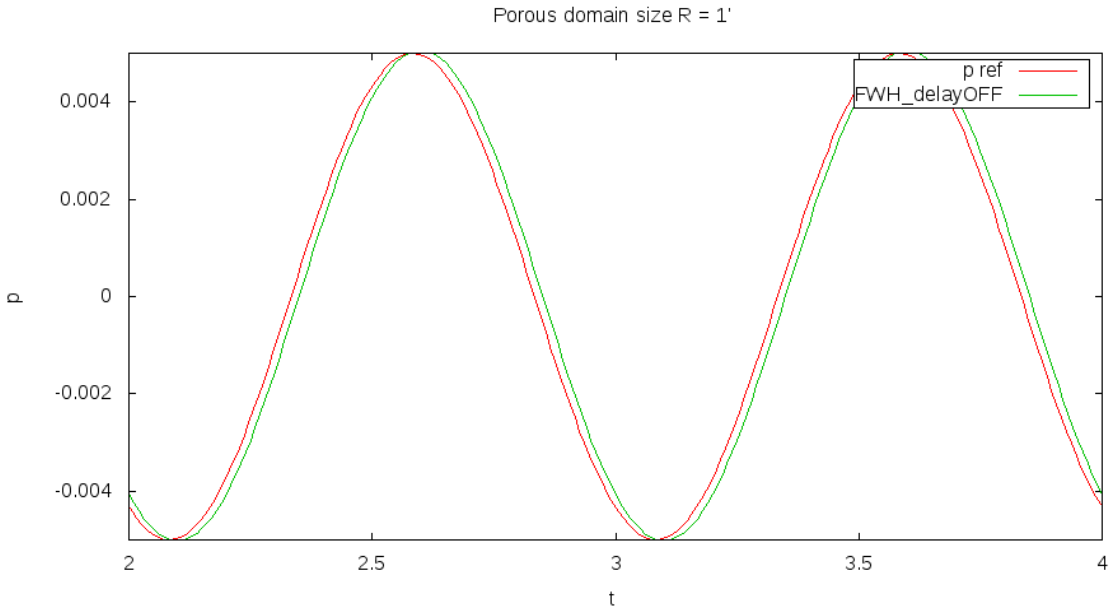

Figure 3.7: Comparison of a monopole pressure field (*p ref*) with time solution of FW-H direct formulation, in case of time delays computation deactivated. The spherical integration domain has radius $R = 1$.

$$\phi(x, y, t) = Ux - \frac{\Gamma\theta}{2\pi}. \tag{3.7}$$

The center of the vortex moves accordingly

$$\begin{aligned} \tilde{x} &= x_0 + Ut, \\ \tilde{y} &= y_0, \\ \theta &= arctg(y/x). \end{aligned}$$

The velocities are derived from the potential and the pressure is calculated from the non-linear Bernoulli equation as

$$\begin{aligned} u(x, y, t) &= U + \frac{\Gamma}{2\pi r}\sin(\theta), \\ v(x, y, t) &= -\frac{\Gamma}{2\pi r}\cos(\theta), \\ p(x, y, t) &= p_0 - \frac{\rho\Gamma^2}{8\pi^2 r^2}, \end{aligned} \tag{3.8}$$

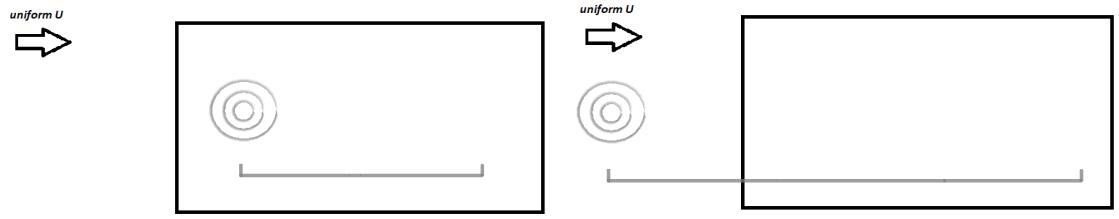

Figure 3.8: Sketch of the two cases reproduced. On the left, the vortex travels inside the rectangular integration domain. On the right, the vortex starts outside the domain, and moves inside passing through the left short side of the rectangular domain (referred to as *inlet side*).

where r is the distance from the vortex moving center $(\tilde{x}, \tilde{y})$ and $\Gamma = U\pi/100$ to ensure small perturbations.
The FW-H integration domain is rectangular and two situations are considered, as in figure 3.8 : in the first case (left panel) the vortex travels inside the integration domain thus any spurious signal is expected in this case; in the second case (right panel) the vortex center is initially positioned outside the integration domain and moves inside the box crossing the left side of the rectangular domain.
The uniform velocity is $U = 10m/s$ and is oriented along the x-axis. The rectangular domain is $100m$ high and $200m$ long, is set such as $y \in [-50, 50]$ and $x \in [0, 200]$. The microphone is positioned at $(x_{mic}, y_{mic}) = (100, 51)$, thus just one meter from the upper long side of the rectangular domain and at half length of it.

Case 1) The time step is $dt = 0.1s$ and the period of the simulation is $T_1 = 10s$. The initial position of the vortex center is $(x_0, y_0) = (50, 0)$. At the end of the period T_1 it reaches the point $(150, 0)$.

Case 2) The time step is $dt = 0.1s$ and the period of the simulation is $T_2 = 20s$. The initial position of the vortex center is $(x_0, y_0) = (-50, 0)$. At the end of the period T_2 it reaches the point $(150, 0)$.

The flow field data u, v and p given in eq. (3.8) are collected both along the perimeter of the rectangle (which represents the porous surface) and in the area contained in the rectangle (which represents the volume region).

3.2.2 Direct vs porous formulation

Direct and porous FW-H formulations are compared for the two cases. In the first case, the vortex never crosses the boundaries of the FW-H domain. As expected, the resulting signals coincide, as showed in figure 3.9. The passage of the vortex results as a lowering and rising of the pressure. The minimum, at $t = 5s$, is reached when the vortex is in correspondence of the microphone, i.e. $x_{mic} = \tilde{x}$.

In the second case, the vortex crosses the inlet side of the rectangular domain. In figure 3.10 the pressure profile reconstructed by the FW-H porous formulation, at time $t = 5s$, shows a sort of discontinuity. This spurious signal is due to the passage of the vortex through the inlet side. The FW-H direct solution looks smooth and both of the compared solutions reach the minimum pressure at time $t = 15s$, which is the time at which the vortex is in correspondence of the microphone.
We may isolate the contribution of the inlet side by integrating on this patch separately. In figure 3.11 (top panel) is noticeable how the spurious signal is due exclusively to the integration over the inlet side.
Looking at te porous equation, it is easy to recognize a term which does not have its correspondent in the direct formulation: it is, in short, the derivative in time of the surface integral of $\mathbf{u}_{\hat{n}}$, where $\mathbf{u}_{\hat{n}}$ is the velocity of the flow projected along the outward normal (unit vector) to the porous surface $\hat{n}$. In this case, the outward normal to the inlet patch is $\hat{n} = (-1, 0)$, thus the integration over this patch depends directly on the streamwise velocity u, being $\mathbf{u}_{\hat{n}} = (-u, 0)$. The streamwise velocity at the center line ($x = \tilde{x}$) of the vortex has a discontinuity, as depicted in figure 3.12. It means that, as the vortex crosses the inlet side, the term related to the velocity u contributes to the overall signal by providing a discontinuity.

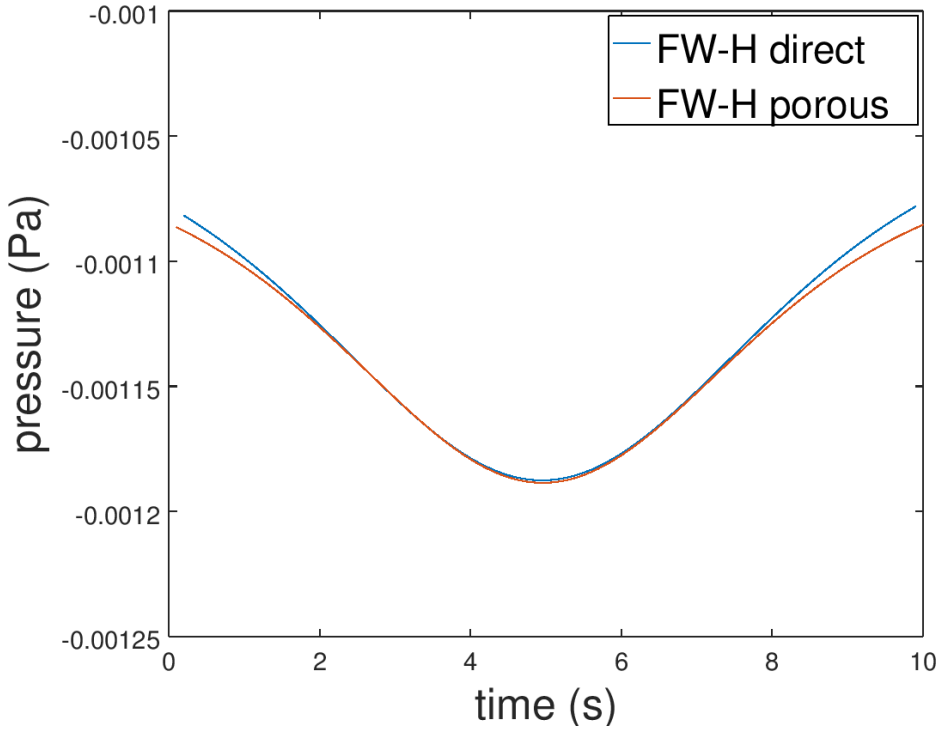

Figure 3.9: Comparison of FW-H direct and porous formulation for the case of an advected vortex which remains inside the integration domain, left panel of fig. 3.8 . Microphone positioned at (x_{mic}, y_{mic}).

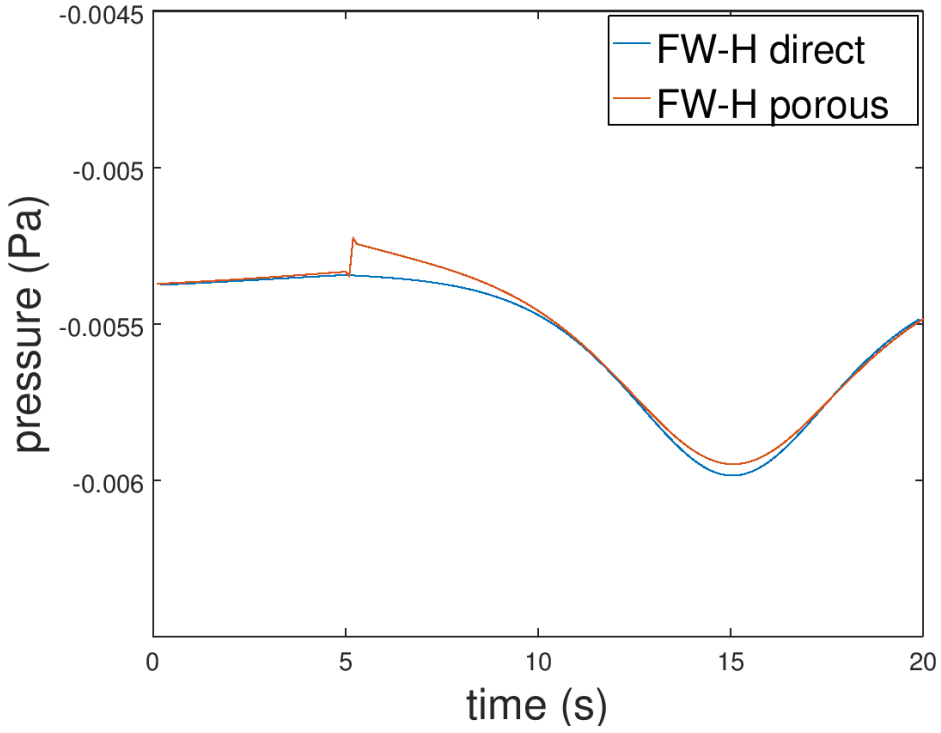

Figure 3.10: Comparison of FW-H direct and porous formulation for the case of an advected vortex crossing the integration domain, right panel of fig. 3.8 . Microphone positioned at (x_{mic}, y_{mic}).

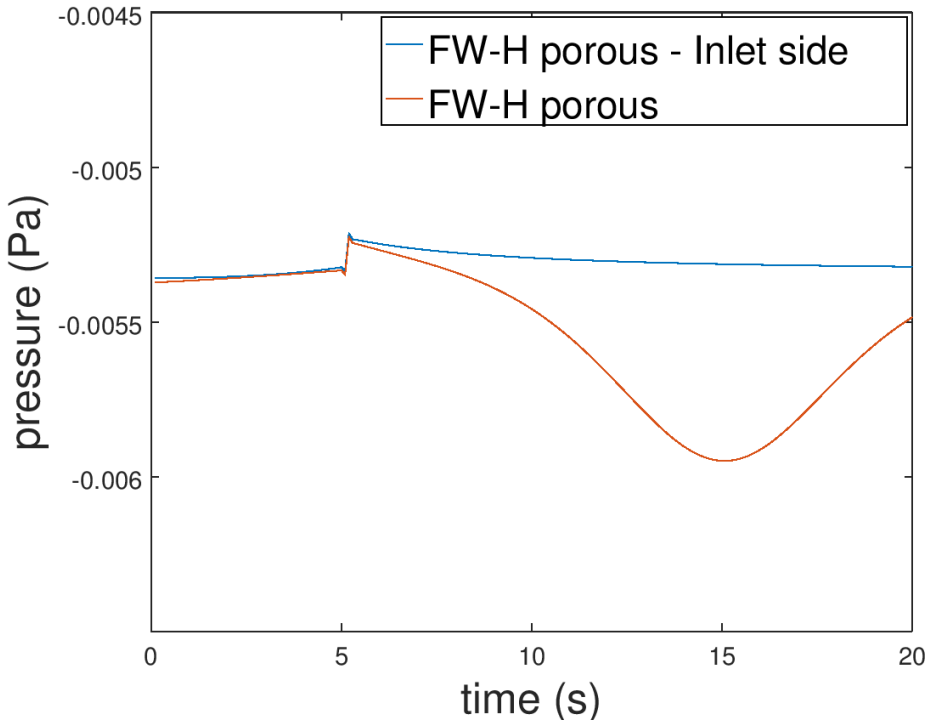

Figure 3.11: Detailed contribution of the side crossed by the vortex.

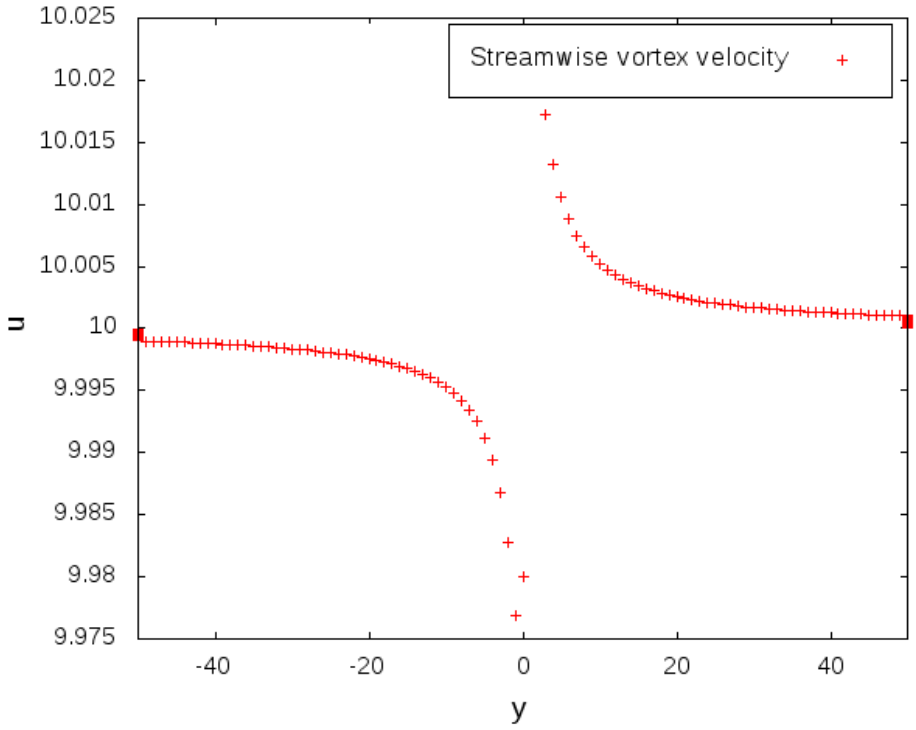

Figure 3.12: Streanwise velocity u of the advected potential vortex, along y, at fixed $x = \tilde{x}$, being $\tilde{x}$ the center of the vortex.

Chapter 4

Flow around a square cylinder

In this chapter, we consider a turbulent flow around a finite-size cylinder with square section (Figure 4.1). The inlet uniform flow, around the body, generates vorticity and turbulence which is advected downstream and the wake assumes an oscillatory pattern. As well known, the flow around an elementary geometry such as a cylinder, has always represented a benchmark for CFD simulations, especially for the periodic vortex shedding mechanism occurring in a wide range of Reynolds numbers. This mechanism is responsible of a strong tonal (named aeolian) noise and different authors adopted the Curle's (linear) formulation to analyze the flow-induced noise (see, for example, [23, 40]). Even in case of such a simple configuration, it is fundamental to account for the (non linear) contribution from the (turbulent) wake, which can affect the resulting acoustic field significantly.
The body has a finite size in the spanwise direction in order to consider a realistic configuration. The finite size produces tip vortices interacting with the vorticity field generated by the cross-stream section, making the problem different from its simplified two-dimensional counterpart. The Reynolds number is large enough to generate a fully turbulent wake, characterized by a wide energetic spectrum. However, the use of a high aspect ratio enables the comparison with analogous results available in the literature (at least for the fluid dynamic solution) at the central section of the cylinder. In order to obtain a realistic instantaneous velocity–pressure field, the fluid-dynamic simulation is carried out using wall–resolving LES (that is, a LES where the viscous sublayer developing in the near–wall region is directly resolved and no-slip boundary condition is used). As above mentioned, in fact,the vorticity field generated in a wall-resolving LES contains the frequencies relevant for the noise generation and propagation, while the subgrid-scale contribution does not appreciably affect the pressure signals. In this sense, the results of the fluid-dynamic simulation can be considered as practically free from modeling errors, thus allowing for a clean comparison between different acoustic methodologies. Due to the lack of any experimental data or analogous acoustic simulations available in literature, the noise predictions will be directly compared with the pressure provided by the underlying LES, here considered as a reference quantity; details on the feasibility of this procedure can be found in [26] and will be discussed later.

The numerical solution of the integral solving approaches discussed in section 2.3.5 are compared. In particular, we first compare the Curle and porous formulations, in order to assess the relevance of the nonlinear terms and to identify the dominant source mechanisms taking place in the flow, both near and far from the body. Then, the results from the porous method are compared with a full and direct solution of the convective equation, including the volume integrals appearing in (2.38).

4.1 Numerical setup

Both fluid dynamic and acoustic fields are solved in the framework of the OpenFOAM®library, based on Finite Volume Methods (FVM). Specifically, we use the pisoFOAM solver, with spatial derivatives discretized using second-order central differences, whereas implicit time advancement runs according to the Euler scheme. The sub-grid scales of the motion were modeled according the Smagorinsky model.
The FW-H solving formulation was implemented as a post-processing utility of the LES data. Here, for sake of completeness, a brief description of the procedure is given. The size and shape of the integration surface/volume is given as input. The algorithm reads the flow data, (i.e. velocity and pressure fields), the surface of the body and the volume of the cells over which to calculate the integrals. It calculates the integrand functions of eqs. (2.37) and (2.38) over each single element respectively and then it sums over the whole integration domains. The time derivatives appearing in eqs. (2.37) and (2.38) were calculated using both second- and forth-order schemes.
The equations are solved by a forward–in–time integration scheme: at each source point of the integration domain, the emission time τ is fixed and identified by the time step of LES run, so that the corresponding observer time t is determined by the code. Then, each signal is computed within its own time window and a data fitting procedure is implemented to calculate the resulting noise signal as the sum of single sources contributions. Due to the absence of body motion and the high value of sound speed, the compressibility delay $t - \tau$ here reduces to a time shift homogeneous in space, which does not affect the overlapping of elementary signals. In other words, the body together with its own wake, appear as a compact source and the calculation of the delays could be omitted, in order to obtain an instantaneous ("incompressible") propagation of noise: this allows for a remarkable saving of CPU time and makes the computation of the volume (quadrupole) integrals feasible and even advantageous.
Figure 4.1 shows a sketch of our test case, together with the frame of reference and geometrical parameters. The square cylinder has side $d = 0.04$ m and length $h = 30d$. It is immersed in a uniform velocity stream $U_0 = 1$ m/s, so that the Reynolds number based on the side d is $Re_d = 4000$. At the boundaries of the computational domain we set a zero-gradient condition for the pressure. The grid consists of about 3 millions of cells, a linear stretching enables high spatial resolution near the body surface. The grid spacing normal to the wall for the first layer of cells is $0.01d$ at the cylinder surface directly resolving the viscous sublayer. The mesh is stretched in the cross stream direction y, in order to have

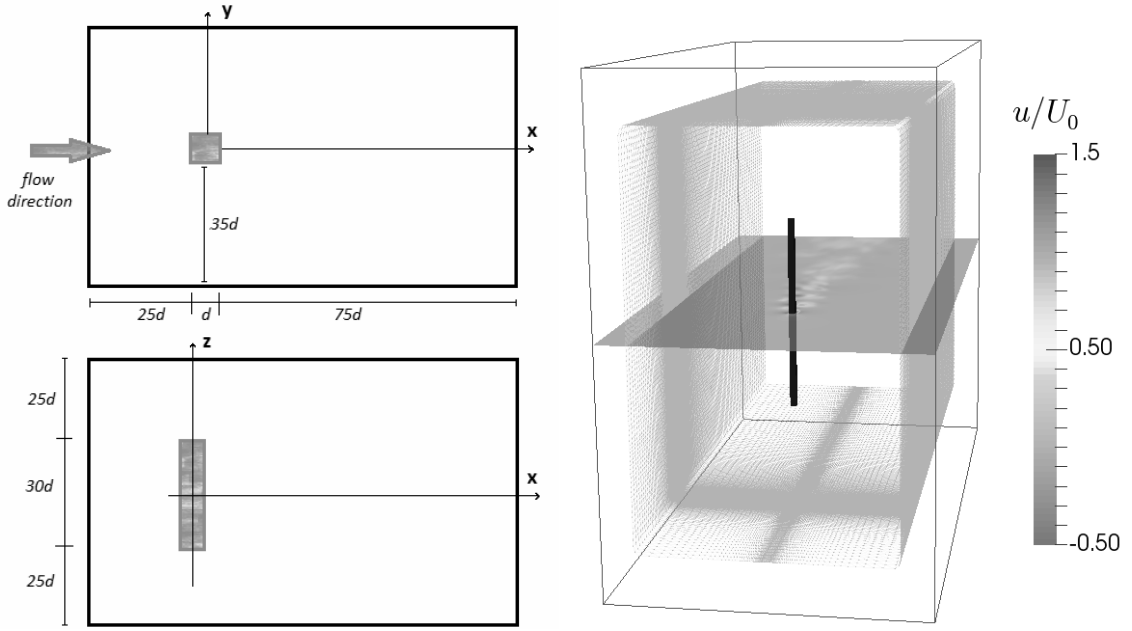

Figure 4.1: Left panel: frame of reference and geometrical parameters of the simulation. Right panel: sketch of the finite-size cylinder with square section, the computational grid is the black outline, while an example of porous domain considered for the FW-H formulation is displayed in light gray.

a cell expansion ratio of 30 between the first cell on the body and the last, at the edge of the domain. Cells are stretched also along the streamwise direction; in the wake region, at a distance of $20d$, cells are slightly elongated along the x-direction and the maximum grid size reaches $0.5d$. The resolution on the wake region may produce inaccuracies; thus we performed an additional simulation by using a grid (hereafter referred to as *homogeneous grid*) which was built starting from the previous one carrying out a redistribution of points in order to have higher resolution on the wake and coarser resolution in the boundary layer. Grid spacing Δx goes from $0.06d$ in the proximity of the cylinder to a maximum of $0.12d$, in the wake region. Remarkable differences (reported in the next section) are observed in the fluid dynamic field using the two grids, the first grid (hereafter referred to as *fine* grid) being able to give more accurate results. However, since here we are interested in the evaluation of the ability of the acoustic analogy to reconstruct the fluid dynamic field, for this aim the signal provided by the homogeneous grid may also serve as a good dataset. In fact we haven't observed any difference in the ability of the acoustic solver to reconstruct the pressure signal.
In order to keep the Courant number under the threshold of 0.5, the time step was set equal to $\Delta t = 5 \times 10^{-5}$ s. Once the flow was completely developed, data were collected in two groups: (a) a time-window of about $250t_c$ ($t_c = d/U_0$ being the inertial time scale),

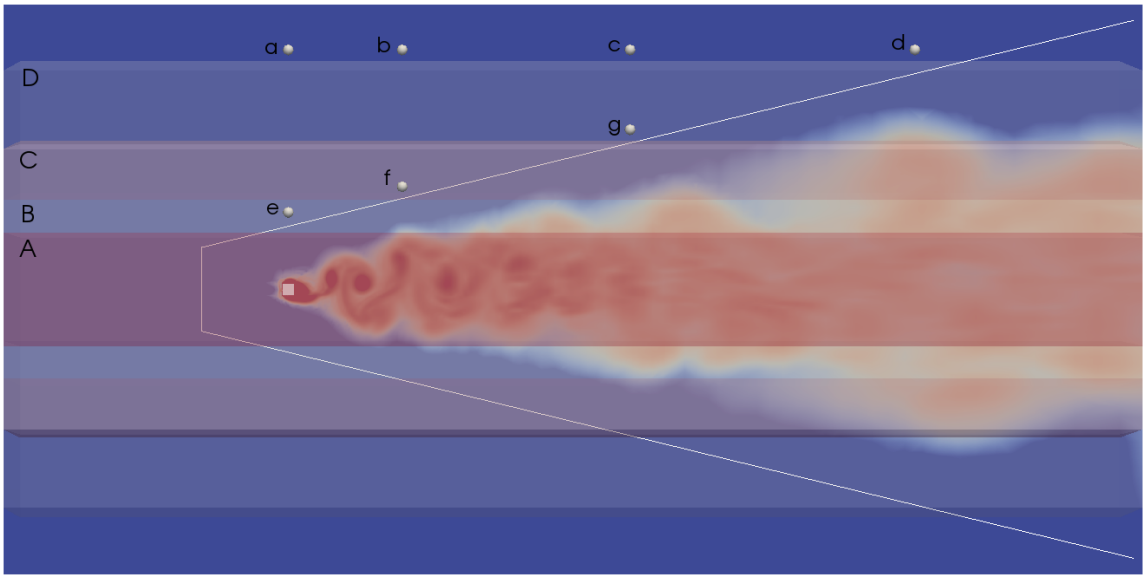

Figure 4.2: Two-dimensional sketch of the z-plane and the corresponding cross-sections of different porous domains herein adopted: four concentric rectangular open boxes A, B, C and D and a pyramid E (white line). Points $a, b, .., g$ indicate the probes.

sampled with a larger time interval $(5/4)t_c$ and (b) a time-window of about $75t_c$, sampled with a time interval $t_c/4$. These time intervals are those employed in the acoustic solver. The flow data of group (a) are used to evaluate the statistics of the turbulent field. The availability of two different datasets allows to analyze the possible influence of sampling interval on acoustic calculations.
Subsequently, the acoustic analogy was applied to determine the pressure time history at different measurement points (probes). By positioning the probes within the fluid dynamic computational domain, it was possible to compare the pressure coming from the acoustic model with that provided by the LES (incompressible) solver, the effects of compressibility delays on the resulting signature being negligible. Different domains S_p were selected to test the capability of the porous formulation, varying their own size and shape. These domains are open both at inlet and downstream of the cylinder, thus violating the theoretical requirement for Sp to be closed. Nonetheless, as already mentioned in section 3.2, the closure of S_P may give rise to relevant spurious noise components and the removal of the domain regions crossing the wake is rather a common practice in the application of the porous formulation (see, among the others [3]). On the other hand, our aim here is not to deal with the mentioned end-cap problem, rather to assess the reliability and accuracy of different FW-H-based numerical approaches.
Figure 4.2 shows a side view of the porous domains used for calculations: four concentric rectangular boxes and a pyramidal box. Box D and pyramid E embed the whole turbulent

Table 4.1: Coordinates of probes at $z = 0$ (in terms of the side d of the square section), shown in Figure 4.2.

	(a)	(b)	(c)	(d)	(e)	(f)	(g)
x	0	10d	30d	55d	0	10d	30d
y	21d	21d	21d	21d	6d	9d	13d

wake. We also used a "direct" approach, by computing the volume terms of the FW-H equation, and in order to compare the direct and porous solutions, the 3D integrals were always calculated over the volume enclosed by the corresponding porous domain. The noise predictions were carried out at different probes, located in the plane $z = 0$ and always selecting the y coordinate in order to set the distance of the probe from the permeable domain S_p to one diameter (see Figure 4.2). For clarity, the coordinates of these measurement points are listed in Table 5.1. Finally, without loss of generality, all acoustic calculations refer to air: the fluid density was set to 1.234 Kg/m^3, while the speed of sound is equal to 340 m/s.

4.2 Fluid dynamic results

A turbulent flow around a finite-size cylinder with a square section does not exhibit any direction of homogeneity; nevertheless, due to the selected aspect ratio of the body, the behavior of the flow is comparable to the benchmark case of a 2D square section, at least in the central sections of the cylinder (around $z = 0$). This suggests to average over longitudinal $x - y$ planes along the spanwise direction z, within a limited space interval far from the edges of the body. We make it in the range $-5d \leq z \leq 5d$. Quantities averaged this way in space and over the time-window (a), are denoted with the symbol $\langle . \rangle$. The computed lift (C_L) and drag (C_D) force coefficients are shown in Figure 4.3 for the fine and coarse mesh respectively, while their mean and rms values are listed in Table 4.2. The two meshes give quite different results for both coefficients. The simulation based on the coarse grid exhibits a slightly larger time of vortex release, quantified by a smaller value of the Strouhal number $St = fd/U_0$. This quantity is computed from the power spectrum of the lift force coefficient (bottom panel of Figure 4.3). The fine grid case predicts a Strouhal number close to 0.132, in good agreement with data of Okajima [45]. Specifically, the authors found a constant Strouhal number of 0.133 for a square section placed in a uniform flow, with 0.5% of free stream turbulence within the range of Reynold numbers $1000 < Re_d < 20000$.
Figure 4.4 shows the space-time averaged non-dimensional streamwise velocity component $\langle u \rangle$ along y-lines, at various streamwise locations over the square section. Unfortunately, no reference data were found to validate these profiles, but the fine grid seems to indicate a better resolved velocity field in the near-wall region.

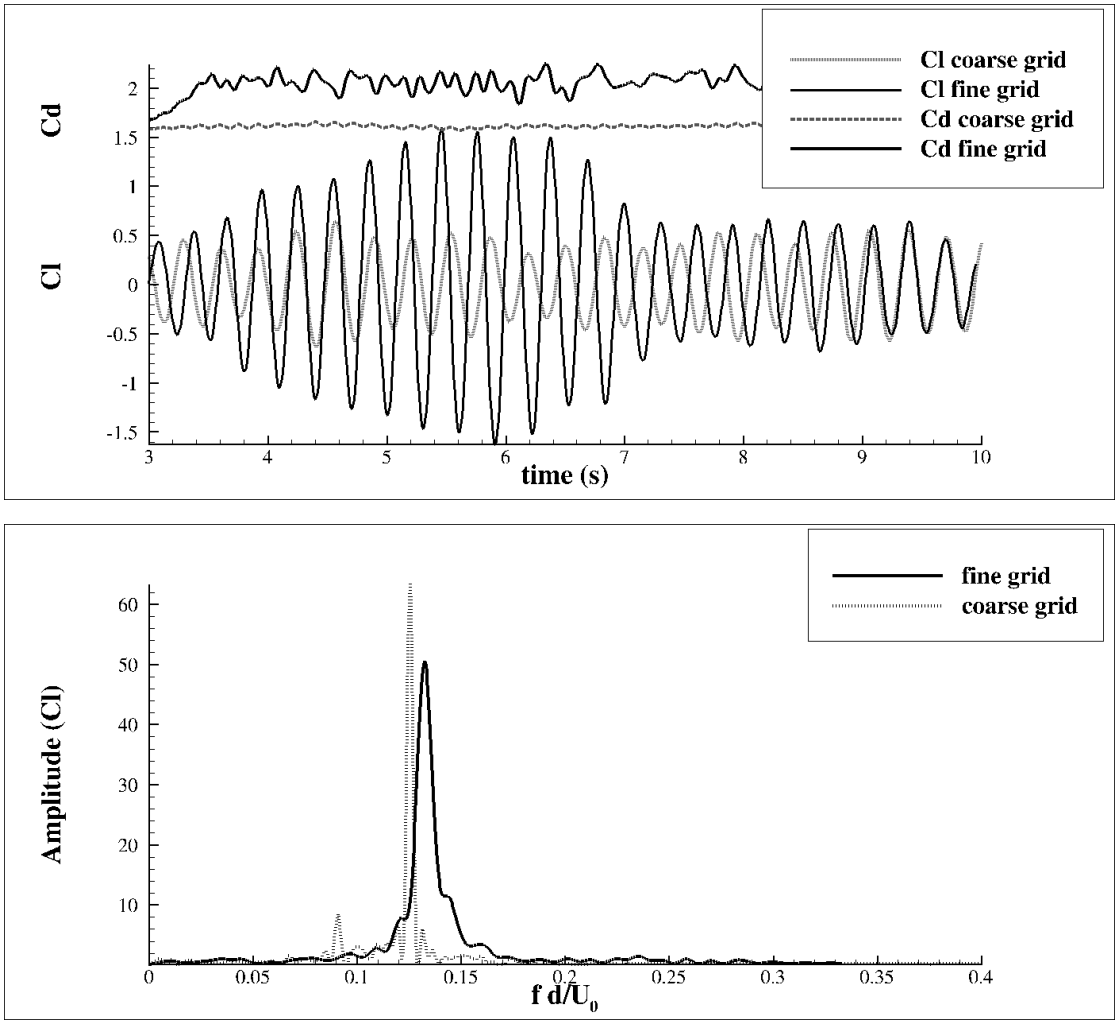

Figure 4.3: Top panel: Time evolution of lift C_l and drag C_d force coefficients. Bottom panel: power spectrum of the lift coefficient C_l which reveals a Strouhal number of 0.132 in case of the fine grid.

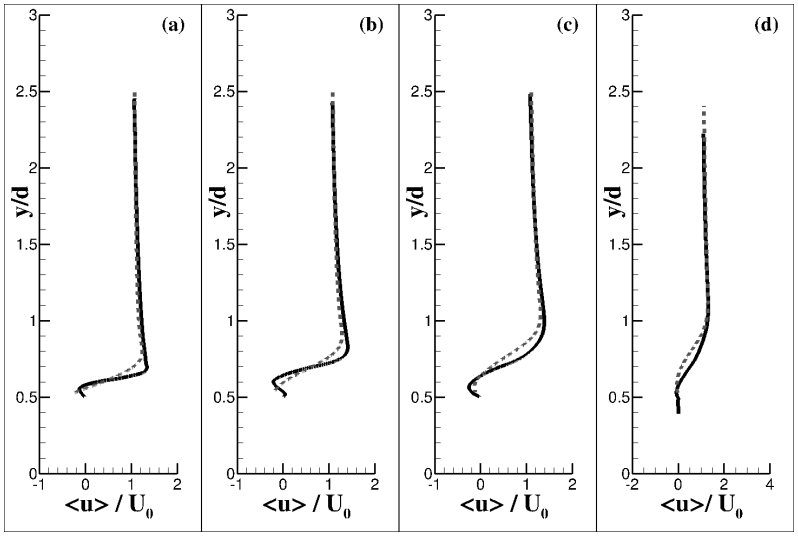

Figure 4.4: Space-time averaged streamwise velocity component $\langle u \rangle$ made non-dimensional with U_0 along the y-direction over the square section: (a) $x = -0.375d$; (b) $x = -0.125d$; (c) $x = 0.25d$; (d) $0.5d$. Coarse grid (gray dashed line), fine grid (solid black line).

Table 4.2: Mean and rms of lift C_l and drag C_d force coefficients.

	$C_{l_{rms}}$	$\bar{C}_l$	$C_{d_{rms}}$	$\bar{C}_d$
fine grid	0.5089	$4.01e^{-4}$	$1.14e^{-2}$	2.073
coarse grid	0.098	$-3.23e^{-4}$	$7.06e^{-4}$	1.607

A comparison between the streamlines obtained in the two simulations (fine versus coarse) is in Figure 4.5. The fine grid simulation (top panel of Figure 4.5) gives flow separation at both front corners. Shallow recirculation regions are observed over the streamwise-oriented surfaces, while two large recirculation regions appear in the wake. The end of this latter separated region is at approximately $x/d = 1$. Note that the coarse grid is not able to completely resolve the boundary layer on the surface of the section and predicts a reattachment point moved further downstream, at approximately $x/d = 2$; also, the grid coarseness is not able to resolve the small recirculation zones over the streamwise-oriented body surfaces.
The contours of space-time averaged velocity components $\langle u \rangle$ and $\langle v \rangle$ are reported in Figure 4.6 together with their root mean square values. The quantities are made non dimensional with the inlet freestream velocity U_0. The maps refer to the fine grid simulation. The small asymmetries in the contour maps are probably due to the acquisition time-window asynchronous with respect to the vortex shedding cycle. Figure 4.6 (c) show the presence of high fluctuations levels in the shear layers developing at the edge of the separation regions. Large values of v_{rms} instead occur on the centerline of the wake, approximately at $x/d = 1.5$, which is behind the reattachment point (Figure 4.6(d)). The shape of the wake, as well as the spatial distribution of the rms of velocity components, are in qualitatively good agreement with previous studies, see for example Oudheusden [46].

4.3 Acoustic results

As a first evidence of non-linear sources occurring in the flow, the term $(\partial^2/\partial x_i \partial x_j)T_{ij}$, based on the Lighthill tensor of eq. (2.35) and the module of vorticity $|\Omega|$ are illustrated in Figure 4.7. The two quantities appear well correlated, with high vorticity regions corresponding to areas of large values of the module of the Lighthill tensor. Note that regions of high vorticity are characterized by very low pressure. This analysis suggests that a quadrupole contribution is expected to be large in this regions.
As above mentioned, the probes are positioned within the fluid dynamic mesh in order to use the LES pressure as a reference data. It might be argued that a direct comparison between FW-H and LES pressure signals is questionable, since we are comparing a noise prediction implying flow compressibility with a pressure signal obtained under the incompressible flow assumption. In practice, the probes are placed at fairly small distances from the acoustic source. Thus, due to the high speed of sound with respect to fluid velocity, to the limited dimension of the mesh and the absence of body motion, the effects of com-

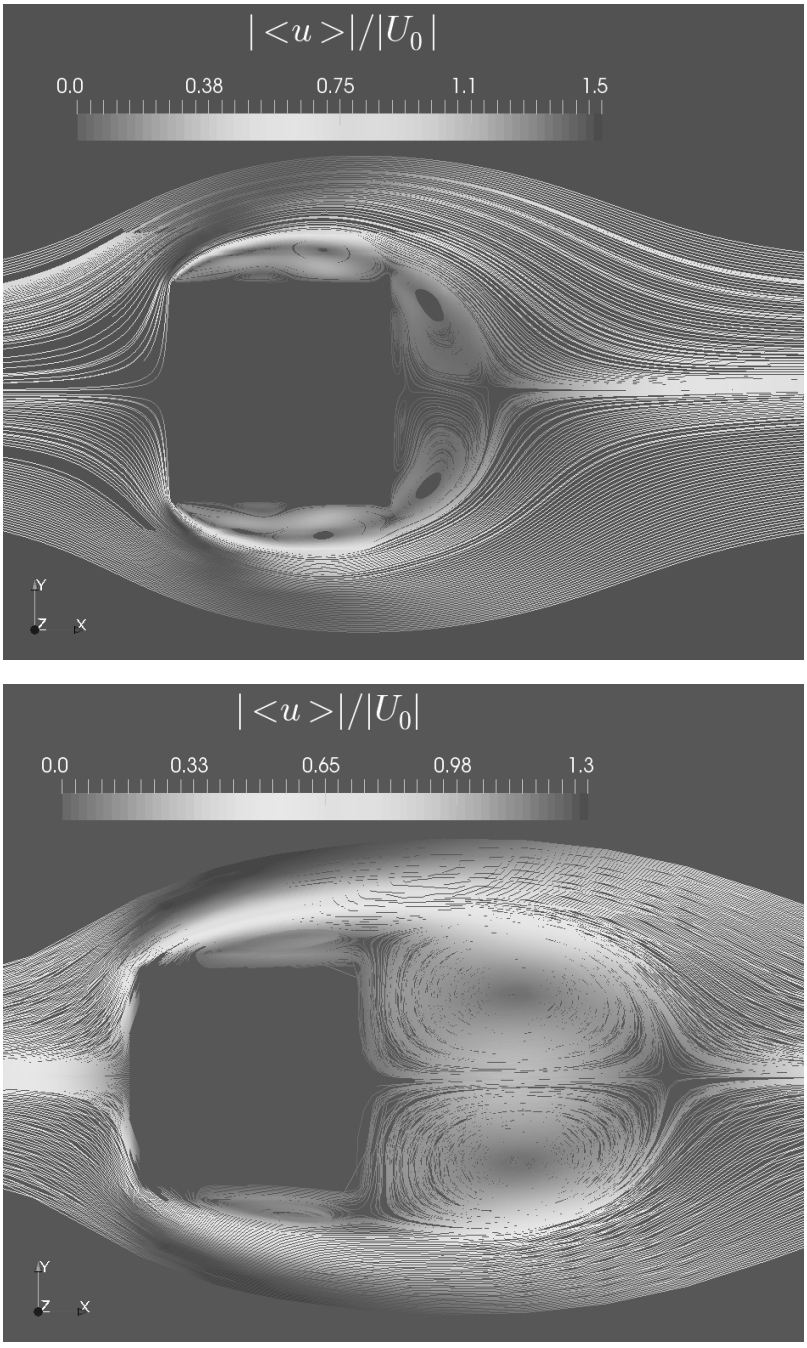

Figure 4.5: Mean flow streamlines together with contour map of the space-time averaged velocity magnitude made non-dimensional with $|U_0|$. Top panel: Fine grid simulation; bottom panel: coarse grid simulation.

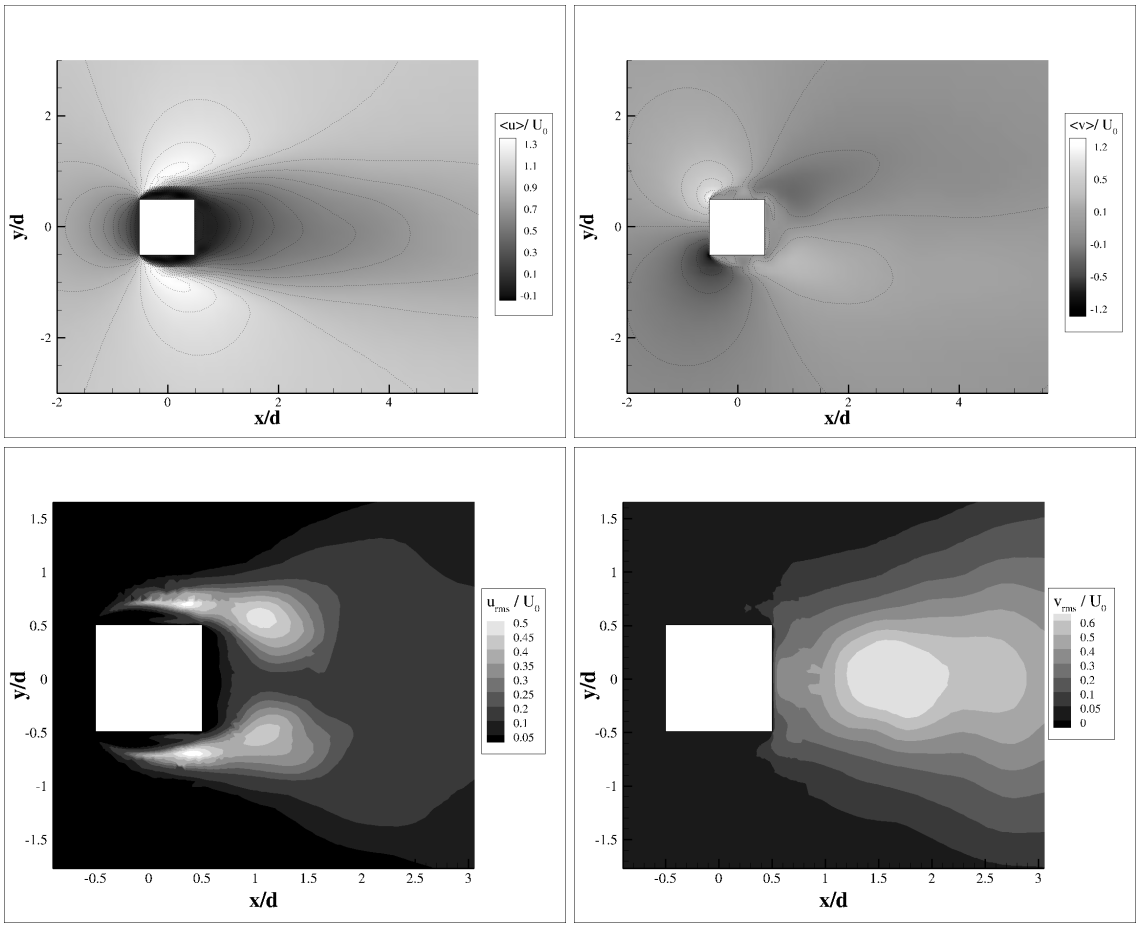

Figure 4.6: Contours of space-time averaged quantities: (a) $\langle u \rangle / U_0$; (b) $\langle v \rangle / U_0$; (c) u_{rms}/U_0; (d) v_{rms}/U_0. Fine grid simulation.

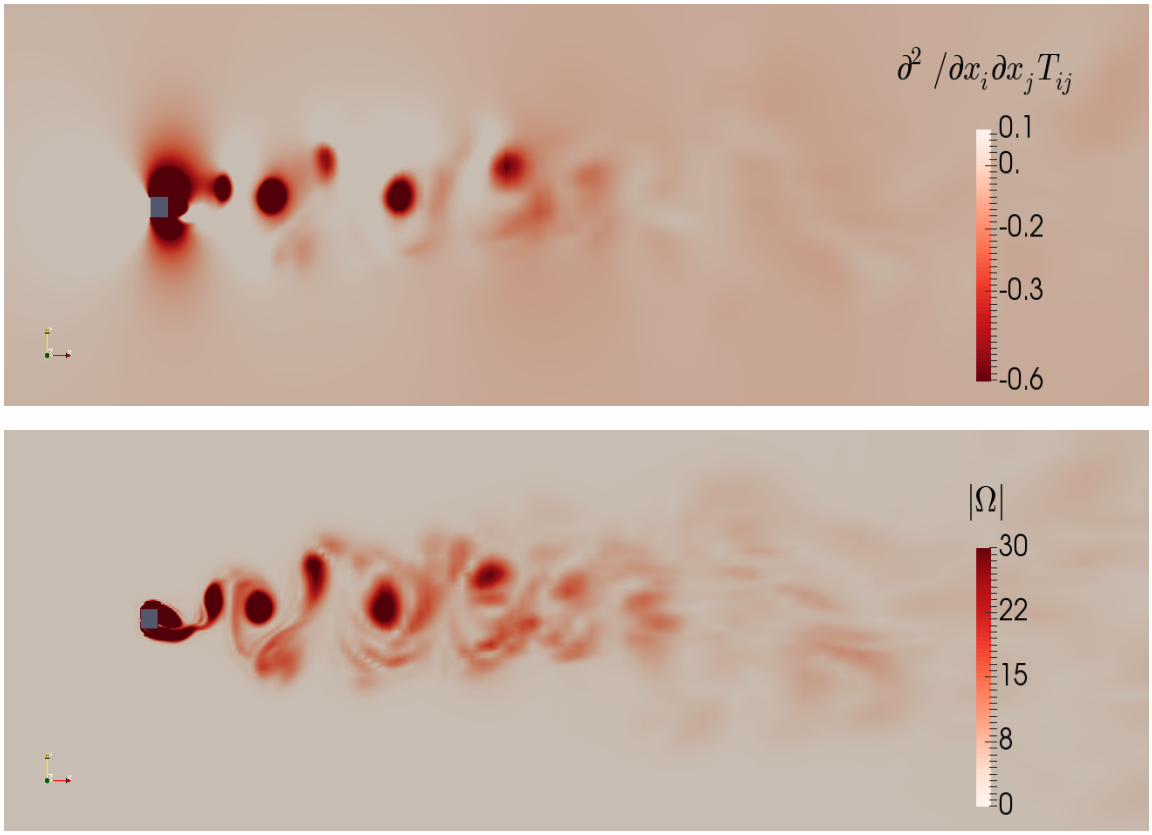

Figure 4.7: Contour plot of instantaneous $\frac{\partial^2}{\partial x_i \partial x_j} T_{ij}$ (top panel) and magnitude of the vorticity $|\Omega|$ (bottom panel).

pressibility on the resulting noise can be neglected. The noise predictions determined by assuming $\tau = t$ or, alternatively, by computing the retarded times as $\tau = t - R/c_0$, are indiscernible and match the LES reference data.
First, we analyze the noise signatures provided by the Curle (linear) formulation, that is the solution of eq. (2.39), at the probes depicted in Figure 4.2, by using the time-window (a) characterized by the large time interval. At probe e, located just above the middle of the square section ($x = 0, y = 6d, z = 0$) the agreement between the LES pressure and the Curle solution is very good, both in terms of amplitude and of resulting waveform (top panel of Figure 4.8). This suggests that close to the body the dominant source mechanisms are related to the loads acting on its surface. It is interesting to note the excellent agreement of pressure peak values, in spite of the higher difference in time resolution of fluid dynamic and acoustic fields and the presence of time derivatives in the integrals of eq. (2.39).
Nevertheless, as we move far from the body, this agreement vanishes. The bottom panel of Figure 4.8 shows the pressure signatures at probe g, still positioned above the middle of the body but in the downstream region ($x = 30d, y = 13d, z = 0$). Here the LES pressure signal exhibits a more irregular pattern indicating the presence of high frequencies, while the Curle solution is still dominated by the fundamental frequency of the vortex shedding and produces a remarkable underestimation of pressure peaks. This behavior becomes even more evident by increasing the distance from the cylinder. Figures 4.9 and 4.10 show the time histories computed with the smaller time interval (group (b) discussed in Section 4.1) and the corresponding spectra of pressure at probes $a - d$ of Figure 4.2, whose coordinates are in Table 5.1. Note the persistent, smooth waveforms predicted by eq. (2.39) and the underestimation of pressure peaks, here present also at probe a located just above the body at $x = 0$. The results in the frequency domain confirm the occurrence of additional components, different from the frequency related to vortex shedding, $f = 3.3s^{-1}$, which, anyway, is well predicted by both LES and Curle solutions close to the body source. These results show the inadequacy of a linear solution for the prediction of acoustic noise in the class of problems herein investigated. Close to the cylinder, the acoustic field is dominated by the fluid dynamic loads on body surface and by the fundamental frequency of vortex shedding in the downstream region. However, moving far from it, additional nonlinear sources get relevant. At this stage, it is clear that an accurate assessment of the acoustic (far) field requires accounting for the contribution of nonlinear, quadrupole sources.
This task can be achieved in two different ways: through the porous formulation, namely eq. (2.39) now integrated on a domain S_p embedding the body and the noise sources, or by adding to the Curle expression the volume terms of eq. (2.38). Also we remark that a complete porous formulation needs the 3D terms contribution from the external volume. The proper choice of the domain S_p plays an important role. Looking at Figure 4.2, the wake spreads and progressively expands downstream, making a "rectangular" domain (like A, B or C) to cross the wake, unless we use a sufficiently large box (like D), able to apparently enclose the whole vortical and turbulent field propagating downstream. There, however, the fluid dynamic data must reckon with the spatial limits of the mesh and the effects of numerical boundary conditions. Furthermore, as already discussed, the solutions has to deal with the end-cap problem and occurrence of spurious noise components due to

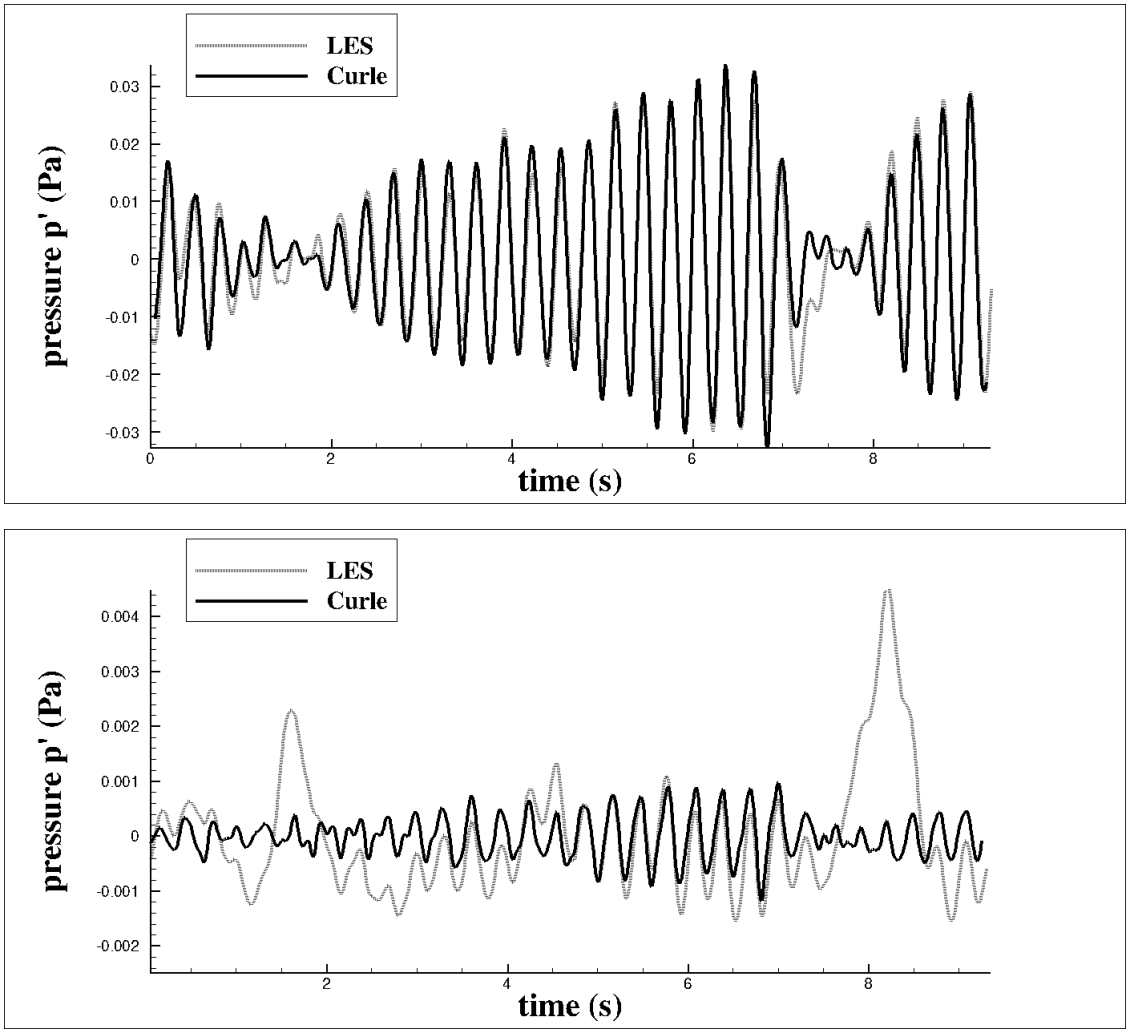

Figure 4.8: Pressure time signals obtained by LES and Curle (linear) solution at probes e (top panel) and g (bottom panel) of Figure 4.2.

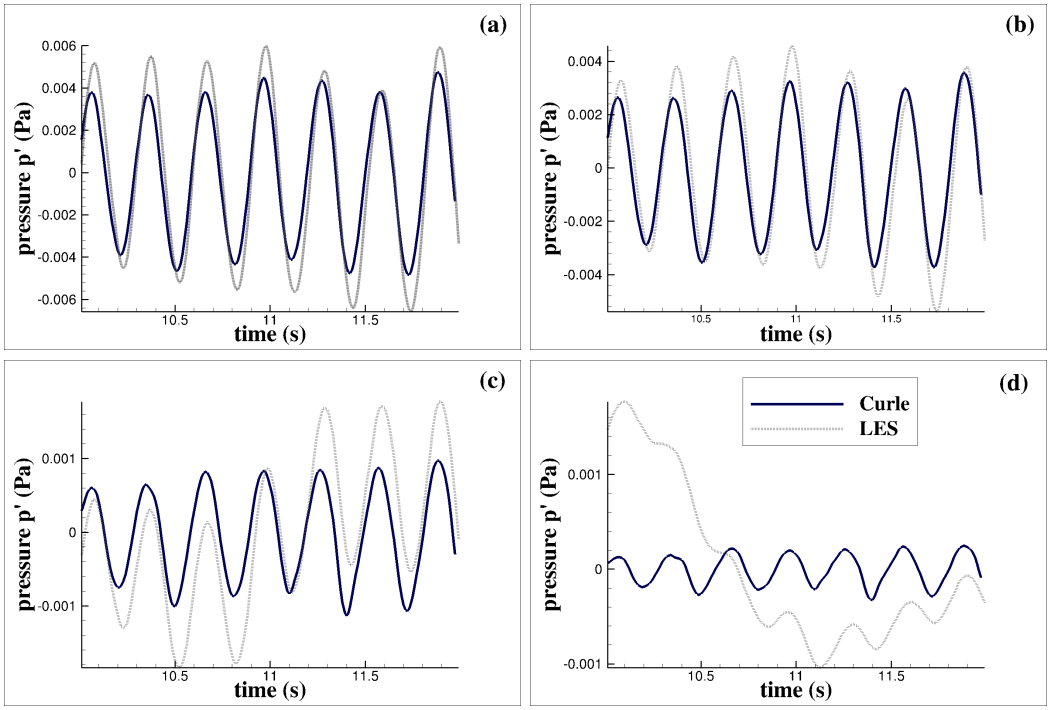

Figure 4.9: Pressure time signals obtained by LES and Curle (linear) solution at probes $a - d$ (in panels (a) to (d) respectively) of Figure 4.2.

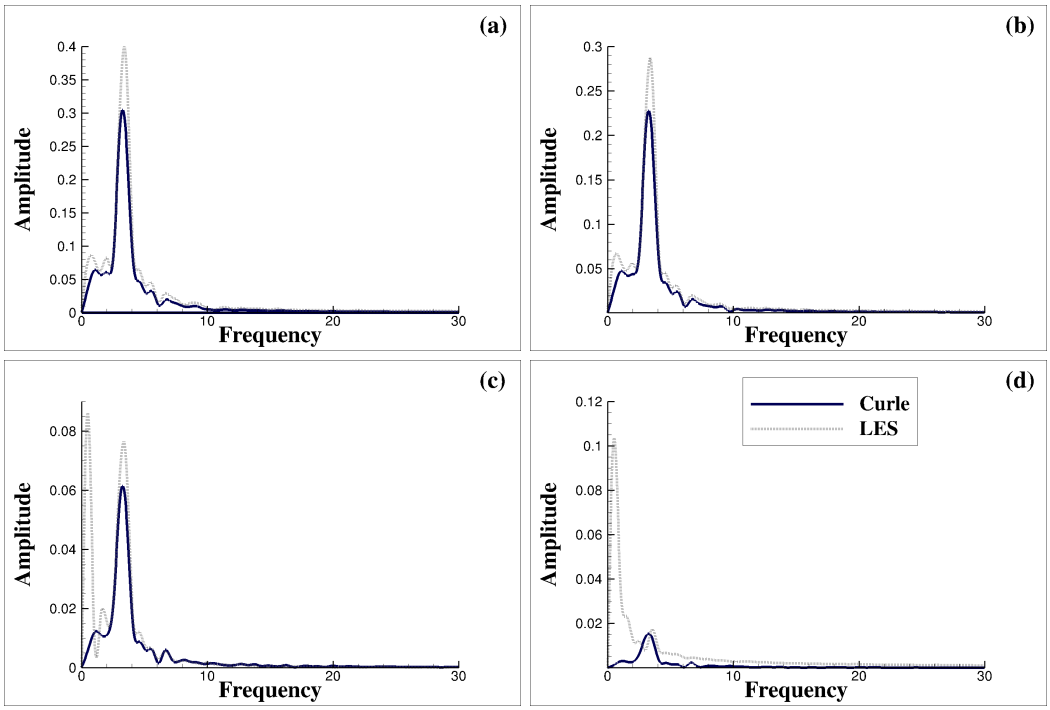

Figure 4.10: Pressure spectra obtained by LES and Curle (linear) solution at probes $a - d$ (in panels (a) to (d) respectively) of Figure 4.2.

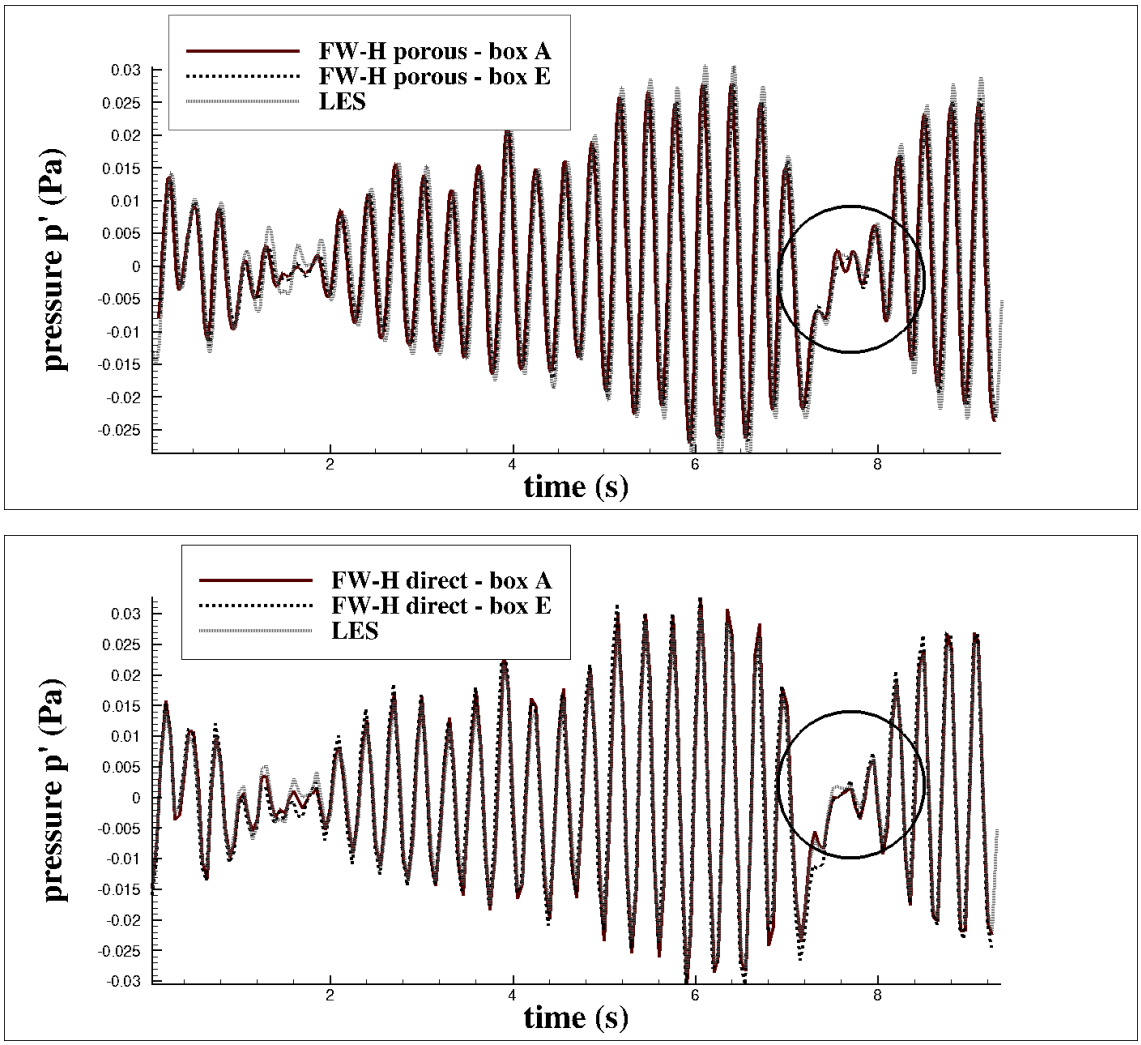

Figure 4.11: Pressure time signals obtained by LES, porous (top panel) and direct (bottom panel) solutions at probe e, rectangular (box A) and pyramidal (box E) integration domains of Figure 4.2.

the transverse (orthogonal to the flow direction) cutting of the wake.
Figure 4.11 contains time signals at probe e of Figure 4.2: the pressure time signal obtained by LES; the noise prediction provided by the porous formulation by using the rectangular (box A) and the pyramidal (box E) domains; the direct solution of the FW-H equation, carried out by adding the 3D terms integrated over the volumes enclosed by surfaces (box A) and (box E) respectively. The porous solution captures well the main features of the resulting pressure signal, although it slightly underestimates the pressure peaks; the results are unaffected by the choice (rectangular versus pyramidal) of the domain. The direct solution is a bit superior to the porous one, exhibiting an excellent agreement with the fluid dynamic reference data. This is not unexpected, since at probe e the linear solution is already very close to the reference (LES) pressure. However, the contribution from nonlinear sources is able reconstruct accurately the time signal even in the restricted time window highlighted in the picture by a circle, where the linear solution fails (see Figure 4.8).
The behavior does not change moving at probe f as depicted in Figure 4.12. The direct method appears superior to the porous one.
Analysis at probe g, further downstream with respect to the probe f is shown in Figs. 4.14 and 4.13 for different porous domains (A,B,C,E of Figure 4.2).
The porous solution for domain A is not accurate; the use of domain B slightly improves accuracy (Figure 4.13, top panel). The results on domains C and E are even better and similar to each other, although still far from the reference values (Figure 4.14, top panel). Overall, the acoustic solutions with the porous method slowly converges to the reference one when the surface approaches the probe. Also, the fact that the wake may cross the porous surface in the region far downstream the probe, appears irrelevant for the quality of the results, thus suggesting a dominant transversal (orthogonal to the flow direction) directivity of the nonlinear sources.
The direct solution behaves substantially better that the porous one (Figs. 4.13 and 4.14 bottom panels). The solution appears much more robust with respect to the variation of the size of the integration volume. However the best agreement with reference data is obtained when the integration volume has the pyramidal shape (domain E), able to wrap entirely the nonlinear sources. Note that both methods fail to reproduce the two large pressure peaks present in the LES signal (namely at $t \sim 1.8$ and $t \sim 8.3$). Inspection at the instantaneous turbulent field (not reported here), shows that the pressure peaks are associated to advection of large scale vortices across all the domains considered approaching the probe's location. In other worlds, the two turbulent events make the probe immersed within the nonlinear sources, thus making ineffective the FW-H analogy.
The accuracy of the FW-H direct solution with respect to the porous formulation further increases moving far from the cylinder. Figure 4.15 shows the pressure time signals at the furthest probes (a-d). The acoustic prediction is here performed using the smaller time interval (time-window of group (b)), using the largest rectangular domain D depicted in Figure 4.2. The figure clearly shows the reliability of the direct method when compared to the less accurate porous method. In particular, the underestimation of the peak values achieved by using the porous solution can be significant. These results can be better

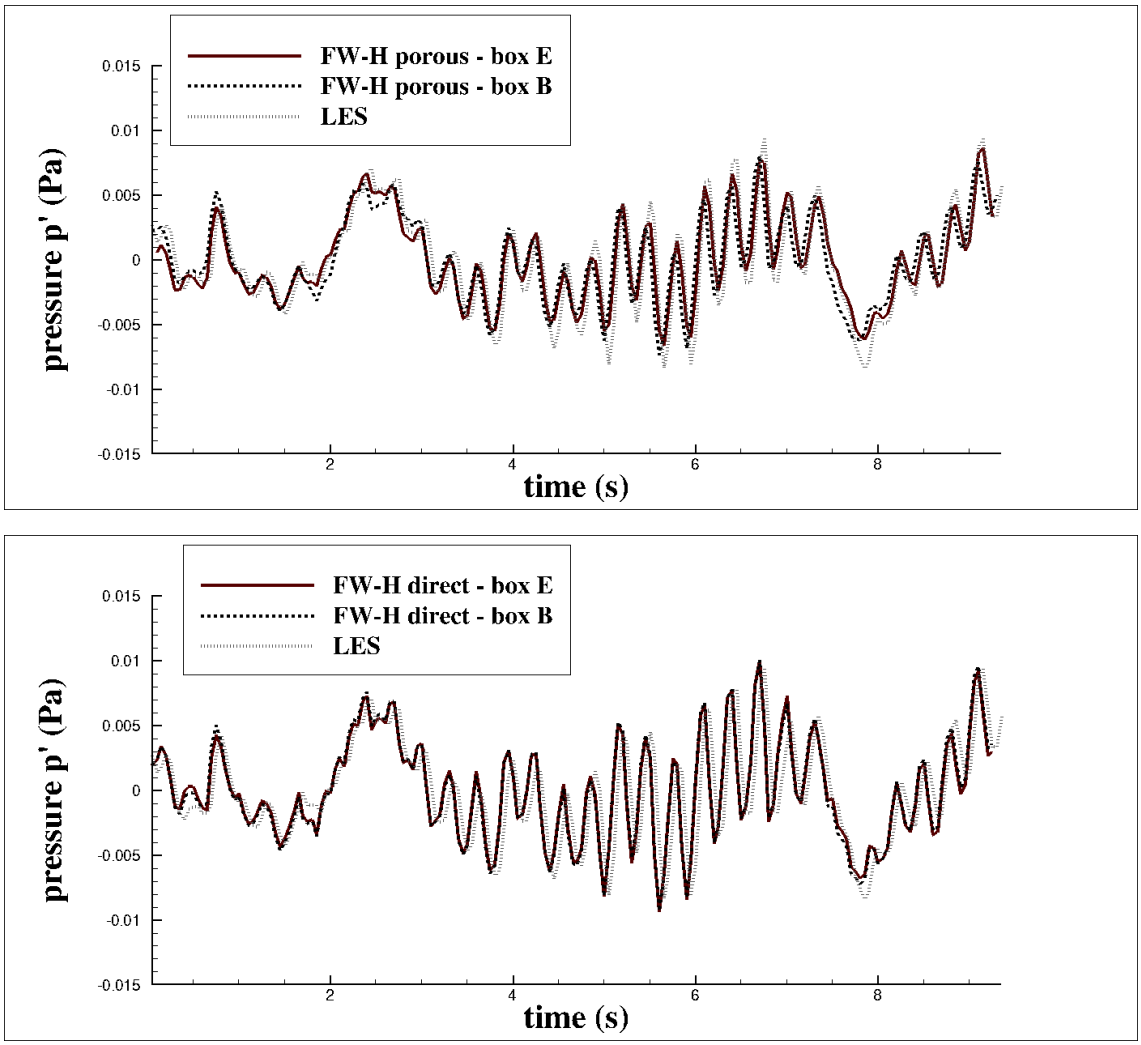

Figure 4.12: Pressure time signals obtained by LES, porous (top panel) and direct (bottom panel) solutions at probe f, rectangular (box B) and pyramidal (box E) integration domains of Figure 4.2.

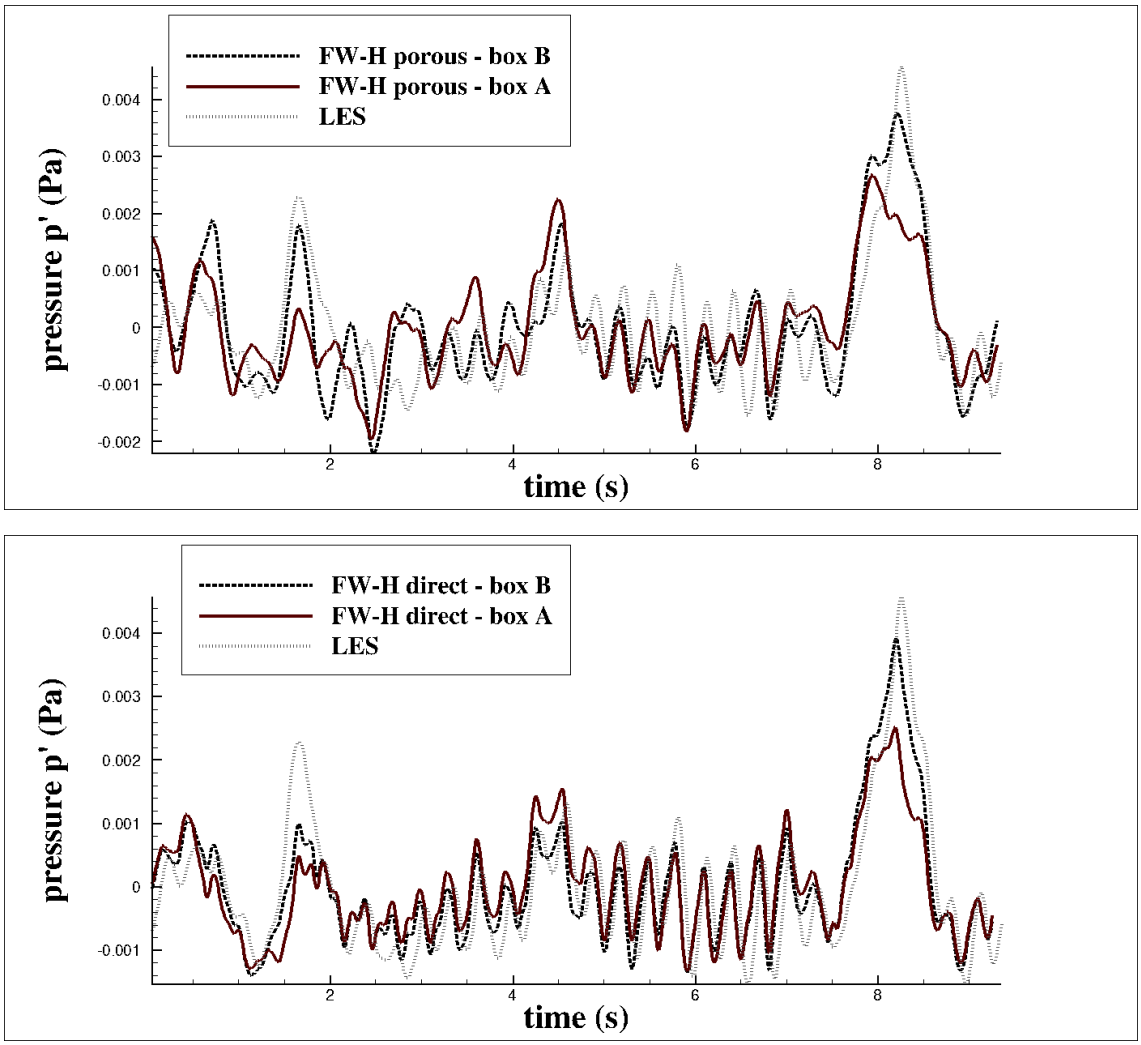

Figure 4.13: Pressure time signals obtained by LES, porous (top panel) and direct (bottom panel) solutions at probe g. rectangular (box A) and (box B) integration domains of Figure 4.2.

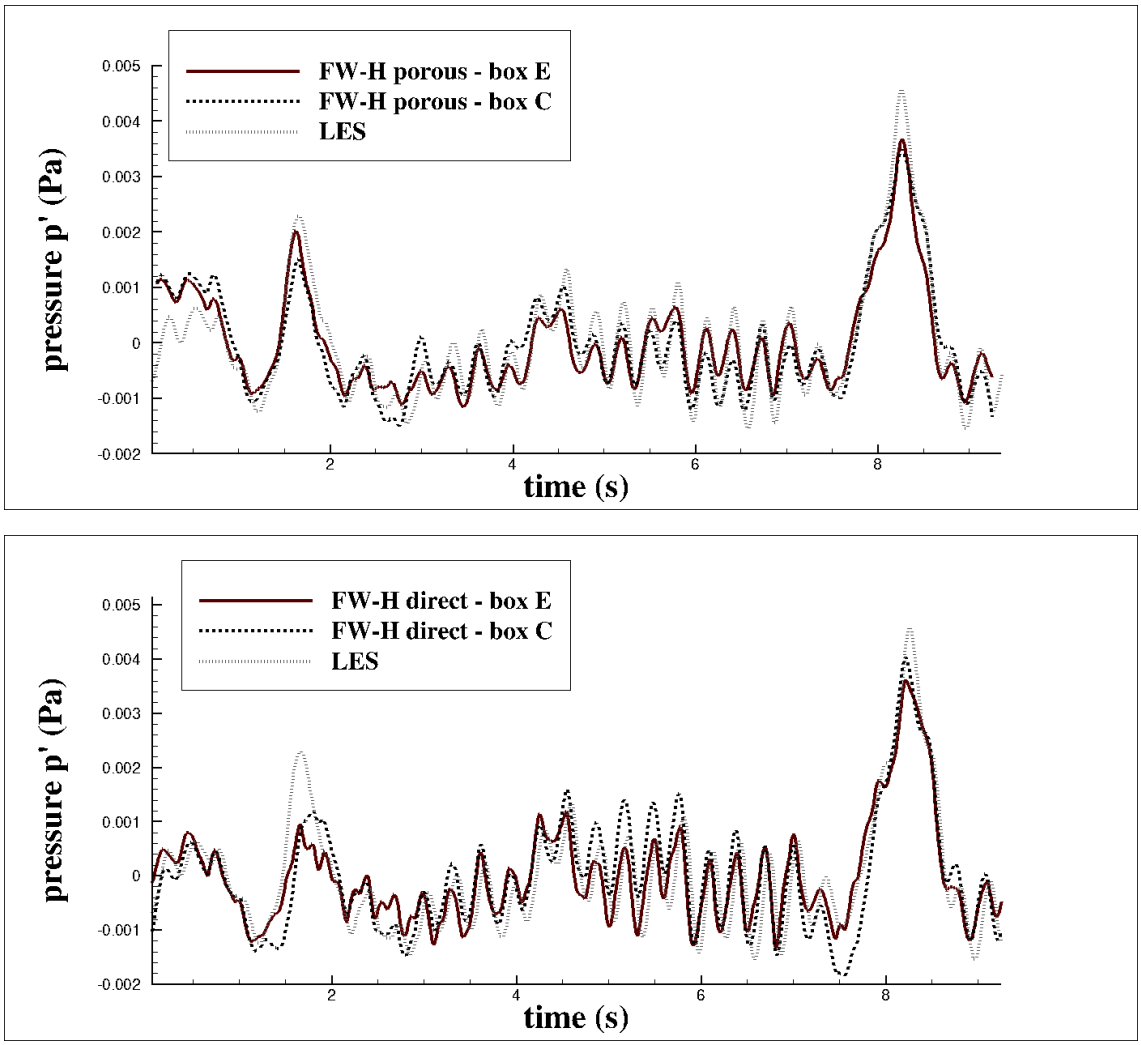

Figure 4.14: Pressure time signals obtained by LES, porous (top panel) and direct (bottom panel) solutions at probe g, rectangular (box C) and pyramidal (box E) integration domains of Figure 4.2.

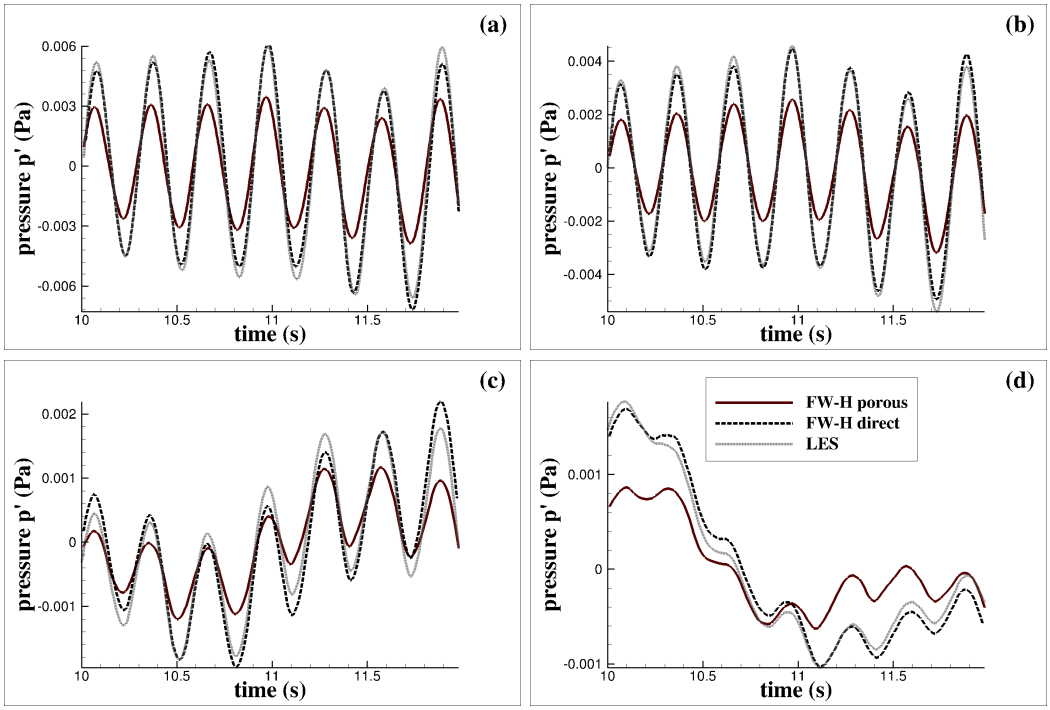

Figure 4.15: Pressure time signals obtained by LES, porous (top panel) and direct (bottom panel) solutions at probes a to d in panels (a) to (d) respectively. Rectangular (box D) integration domain of Figure 4.2.

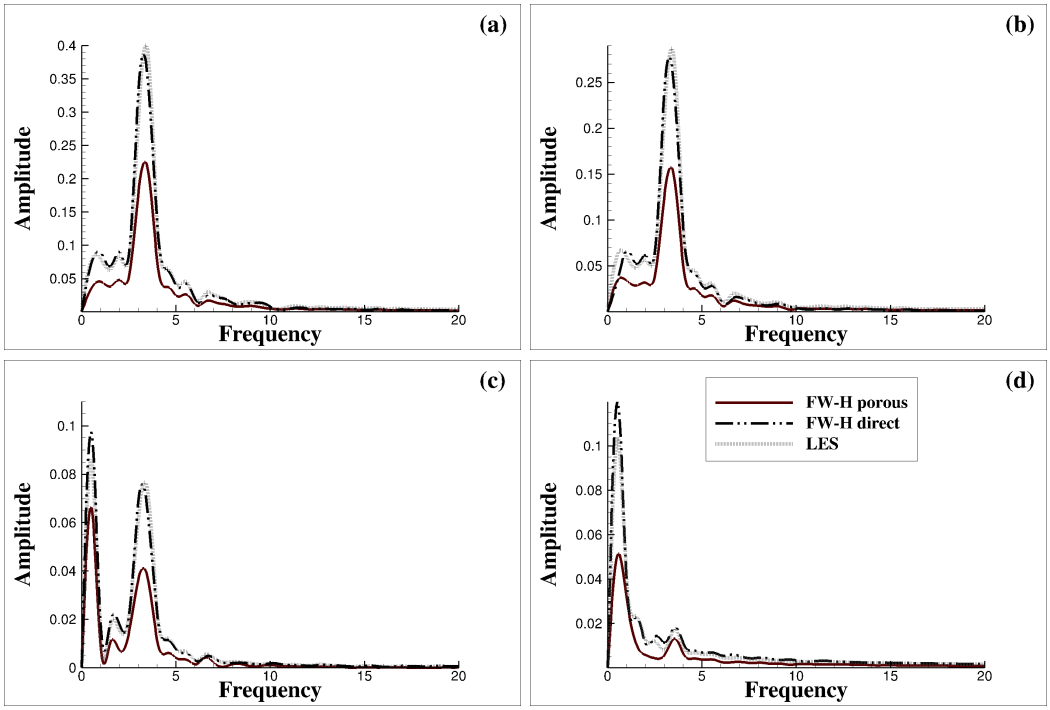

Figure 4.16: Pressure spectra obtained by LES, porous (top panel) and direct (bottom panel) solutions at probes a to d in panels (a) to (d) respectively. Rectangular (box D) integration domain of Figure 4.2.

Table 4.3: L_2 norm of time signals $p'(t)$ of Figure 4.19 coming from FW-H porous and FW-H porous complete formulations, normalized by the L_2 norm of the FW-H direct time signal.

	(a)	(b)	(c)	(d)
$L2 - Por$	0.66	0.67	0.72	0.54
$L2 - PorCompl$	0.85	0.87	0.96	1.02

appreciated in the frequency domain (Figure 4.16). Unlike the Curle solution (see Figure 4.10), at probes c and d the porous approach correctly identifies the relevant frequencies of the resulting noise, but their amplitude is not correctly predicted; on the contrary, the spectrum provided by the direct method matches very well the corresponding LES one, thus confirming the dominant nonlinear nature of the acoustic far field and the robustness of the direct approach.

Concerning the mentioned end-cap problem and the spurious noise components due to the downstream closure of the integration domain, Figure 4.17 shows the pressure time signals (top panel) and the corresponding spectra (bottom panel) at point (d), by using the largest domain D, closed at the downstream section. The presence of the end-cap from one side does not improve the accuracy with respect to the amplitude of the pressure signal, and, from the other side, introduces spurious frequencies which make the prediction even less accurate. This effect is well known in literature and, as mentioned in Section 3.2, recent techniques have proved to be successful at least in 2D fluid-dynamic problems. However it has to be pointed out that the implementation of these techniques may be not straightforward and that the extension to fully 3D cases is still under investigation.

Finally, we consider the complete porous formulation. We recall the original formulation of the porous method which should take into account the volume around the porous surface, as additional source of noise. Thus, we consider equations (2.37) and (2.38), with $f = 0$ describing a porous surface instead of the body surface. The standard use of the porous formulation does not consider the 3D terms contribution coming from the external volume, under the assumption that the terms in eq. (2.38) are negligible. This may not be the case when turbulence and vorticity propagate in the far field.

We add to the 2D integrals related to a permeable pyramidal surface the 3D integrals provided by the "complementary" external volume. Figure 4.18 depicts this particular combination: a pyramidal domain is adopted as a porous surface, the additional external volume corresponds to the region enclosed by the rectangular domain (box D).

In Figure 4.19 results are shown for the complete porous formulation used to evaluate pressure field at probes $a - d$. It is compared to the porous formulation evaluated on the pyramidal domain and the FW-H direct formulation integrated on the whole volume enclosed by domain D. The last was found to be in agreement with the LES reference signals. The contribution from the complementary volume improves the acoustic solutions, especially at the farthest probe d. This confirms that the nonlinear sources are more spread

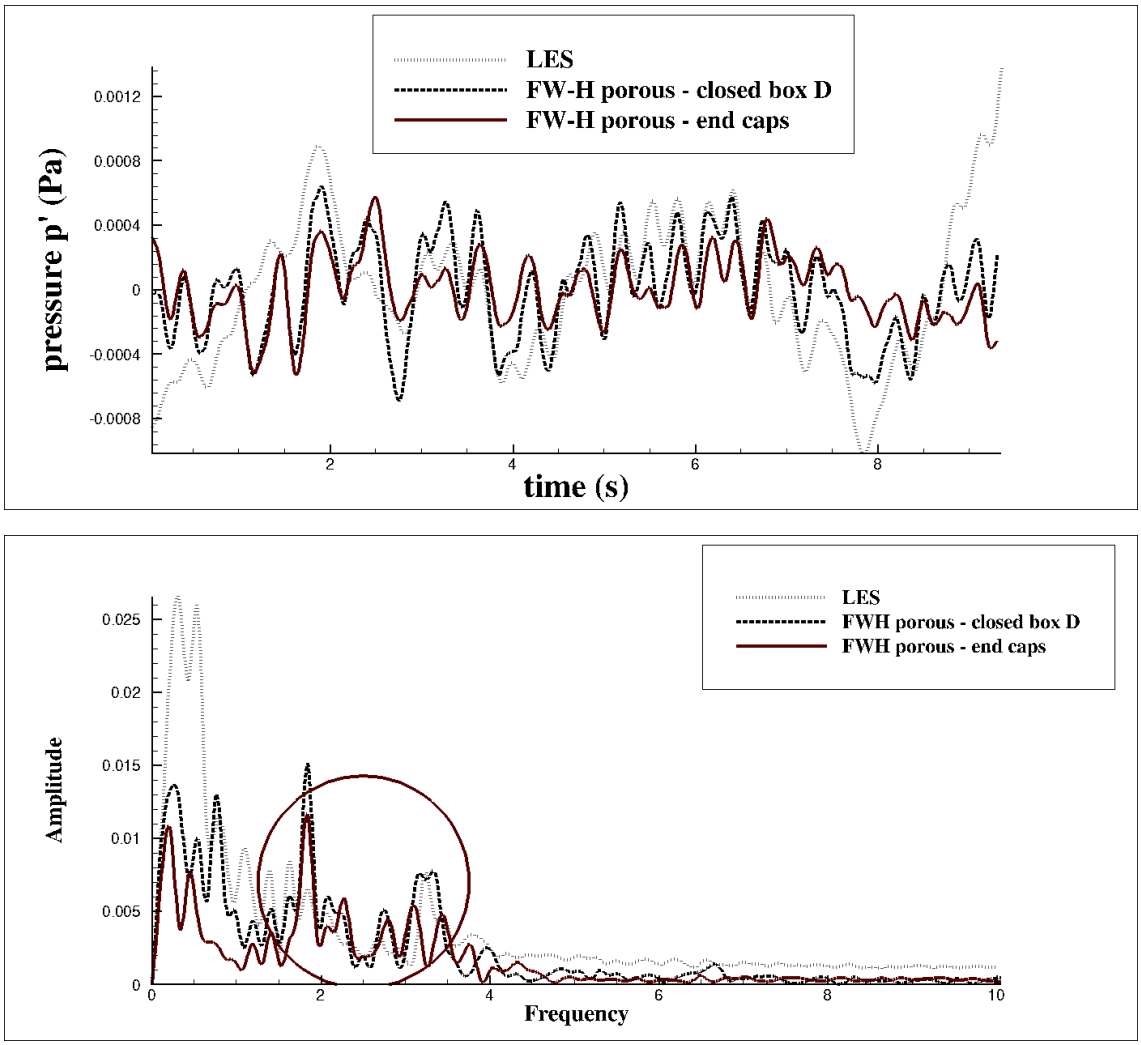

Figure 4.17: Pressure time signals (top panel) and spectra (bottom panel) obtained by: LES, porous formulation evaluated on closed domain (box D), porous formulation restricted to the end-cap contribution.

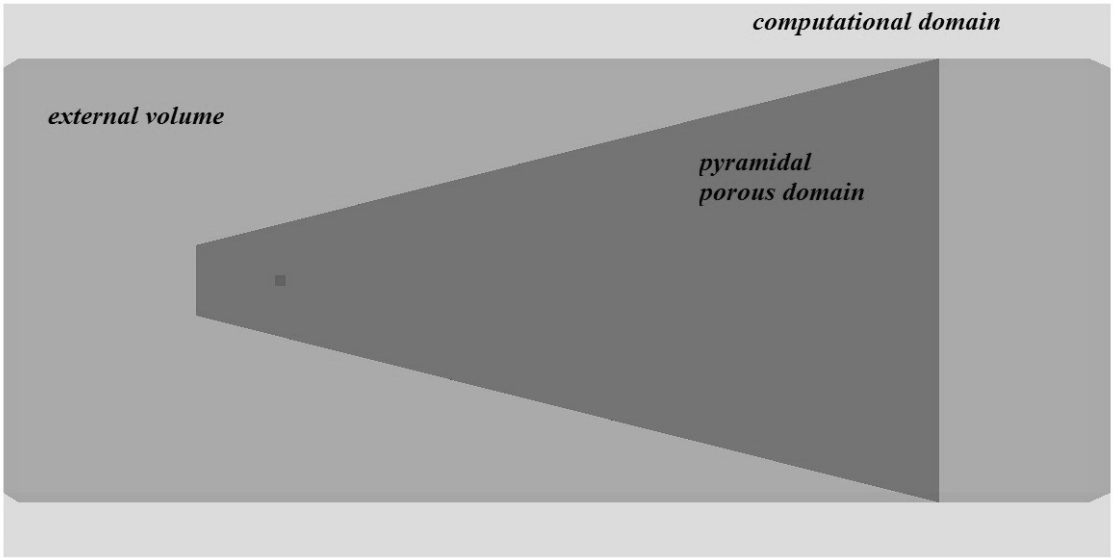

Figure 4.18: Sketch of the domains adopted for the complete porous formulation. A pyramidal porous surface and a surrounding external volume, enclosed in the box D of Figure 4.2.

in the field than one can infer from the visual analysis of Figure 4.7 and the choice of a porous domain apparently embedding the whole vorticity and turbulence field does not guarantee an accurate prediction of noise. To better appreciate the signals differences of Figure 4.19, in Table 4.3 we report the L_2 norm of the time signal $p'(t)$, defined as $|p'(t)|_{L_2} = (\int p'(t)^2 dt)^{\frac{1}{2}}$, corresponding to the FW-H porous $(L2 - Por)$ and the FW-H porous complete $(L2 - PorCompl)$ formulations, normalized by the L_2 norm of the FW-H direct time signal.
The underestimation given by the porous formulation is not fully balanced by the sum of the volume terms. This means that the porous formulation seems "intrinsically weak" compared to the direct solution and this result appears to be a basic drawback of the methodology, regardless of the end-cap problem or of the choice of a suitable integration domain. This weakness is of numerical nature. Even though, from a theoretical point of view, the porous and direct integral formulations are fully equivalent, the type of data and the way they are used can not be inconsequential on numerical result. The volume integration manages the whole, three-dimensional field, locally accounting for any nonlinear source mechanism (in particular, the velocity gradients): in this case, the FW-H equation just appears as an alternative way to solve the Navier-Stokes equations far from the body, in flow regions characterized by small pressure perturbations. Indeed, the direct solution exhibits a very satisfactory agreement with LES data in all positions herein investigated. In the porous approach, on the contrary, nonlinear sources are projected on an external

surface: however careful this projection could be, it carries any unavoidable numerical inaccuracy of fluid dynamic simulation and, represents a loss of information, compared to the volume integration.
The essential role played by the nonlinear sources is also confirmed by depicting the root mean square (rms) values of pressure on different points placed on concentric circles around the body at $200d$, $300d$ and $600d$, just to show the main directivity features of the acoustic far field. Figures 4.20 and 4.21 show the comparison of these values, as determined by Curle (left picture) approach and porous (right picture) one, on plane $z = 0$ and $y = 0$, respectively. Along the flow direction (plane $z = 0$), the Curle formulation provides a typical two-lobed map, very similar to a dipole, clearly related to the fluctuations of pressure on the body surface and the alternate mechanism of vortex shedding from the cylinder (Figure 4.20); on the contrary, the contribution from nonlinear sources makes the noise map more similar to a monopole, exhibiting a generally more intense and uniform acoustic field in the rear part of the body. The same features can be observed in the plane $y = 0$ (Figure 4.21), concerning the plane $y = 0$, where approaches give an elongated shapes in correspondence to the edges of the 3D (finite) cylinder. Once again, however, the noise levels provided by the porous approach are notably higher with respect to the linear solution. We remark that the far-field noise was evaluated also by switching the time delays computation off, thus assuming instantaneous instantaneous noise propagation. No differences were observed comparing these signals with those obtained considering time delays. Results achieved in our study indicate the direct solution of the FW-H equation

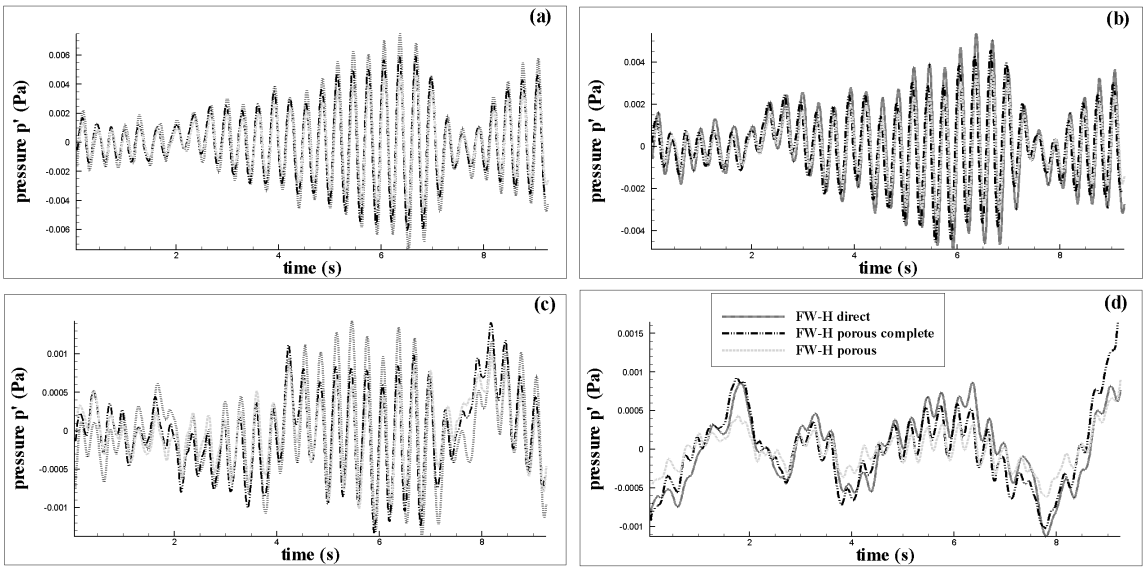

Figure 4.19: Pressure time signals at probes $a - d$ (in panels (a) to (d) respectively) determined by adding to the porous solution on the pyramidal 2D surface the volume integrals computed on the 3D "external volume".

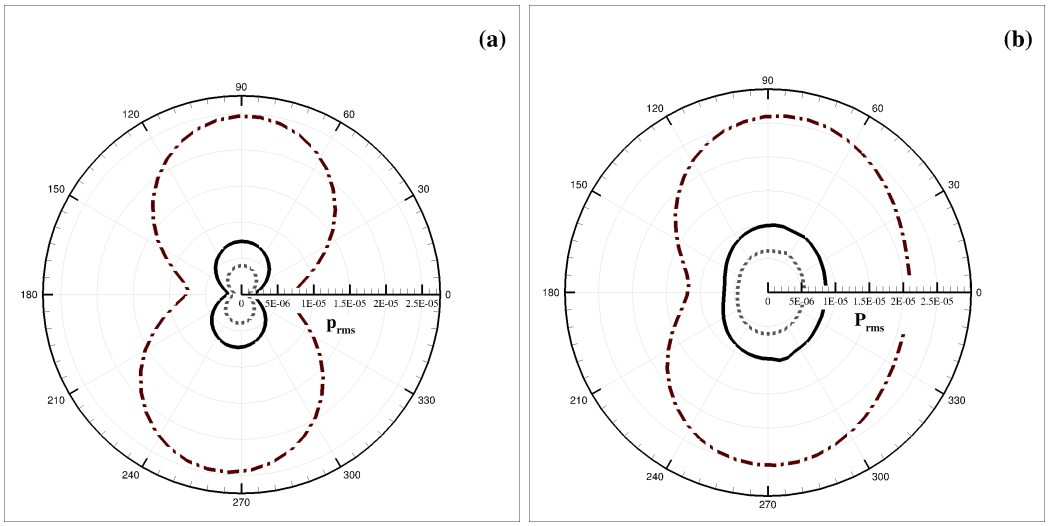

Figure 4.20: The pressure rms values determined by Curle (left panel) and porous (right panel) methods, on the $z = 0$ plane, at a distance of $200d$ (dashed line), $300d$ (solid line) and $600d$ (dash-dotted line) from the cylinder.

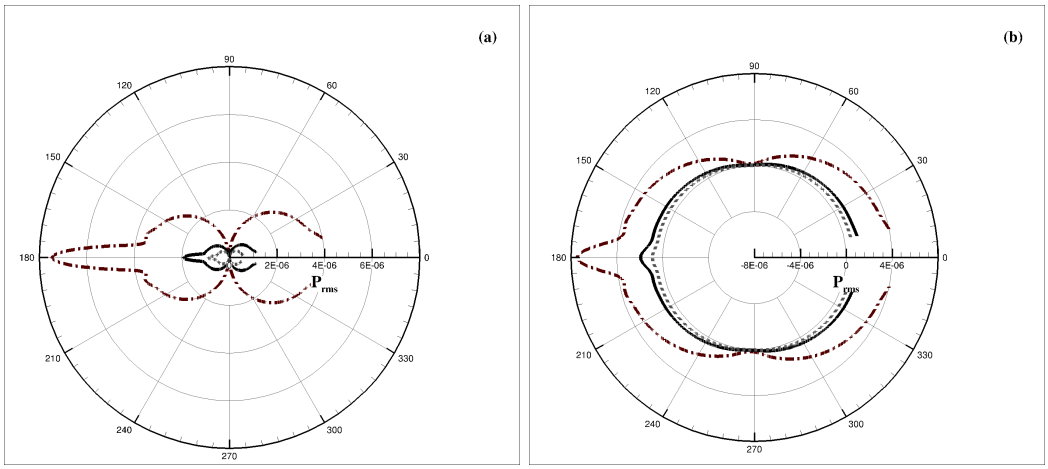

Figure 4.21: The pressure rms values determined by Curle (left panel) and porous (right panel) methods, on the $y = 0$ plane, at a distance of $200d$ (dashed line), $300d$ (solid line) and $600d$ (dash-dotted line) from the cylinder.

as the most reliable approach to compute the noise emitted by the body and nonlinear sources. In fact, the porous formulation is less accurate on its own, is sensitive to the choice of the integration domain whose determination may be not straightforward in presence of complex noise sources and it may suffer for the end-cap problem. On the other hand, the computational resources required by the evaluation of the quadrupole volume integral may be much higher with respect to the faster surface integration of the porous approach. This is true when the compressibility delays must be included in the solution, especially if a noise map is required.
In fact, the unsteadiness of the fluid dynamic problems requires the use of a forward in time integration scheme to solve eq. (2.38): the computation of τ is very simple and fast, but the time shift forces to store the signal from each elementary volume and, successively to perform a time data fitting over millions of cells. This procedure has to be applied at any measurement point and the computational cost may easily become unsustainable. In principle, the compressibility delays should never be omitted. In practice, however, their effects can be really negligible, as confirmed, in the proposed test case, by the perfect overlapping of signatures determined by removing or by accounting them and, ultimately, by the good agreement of noise predictions with LES (incompressible) pressure. Of course, the adequacy of the assumption $t = \tau$ depends on the problem under consideration and, in particular, the possible body source velocity, the speed of sound and the distance of the measurement point. As well known from Aeroacoustics, for example, any assessment of noise from a jet or a helicopter rotor based on such a simplification would be unreliable, even at short distances, due to the concerned source velocity and the sound propagation speed in air ($c_0 = 340$ m/s). Nevertheless, in many other applications this assumption is fully plausible and can be conveniently adopted. It is the case, for example, of noise predictions from wind turbines or marine propellers (for which the rotational speed is very low and the nonlinear sources can play a dominant role, see Ianniello [27]), or the ship noise certification tests, where the body source moves very slowly, the sound has to be measured few hundreds meters from the ship and the sound speed underwater is approximately $c_0 = 1500$ m/s. In our particular case, the compressibility delays were found to be negligible, for the evaluation of the noise pressure in both in the near and in the far field. Thus, in these (and other) cases, a full, direct solution of the FW-H equation is probably the most accurate and even convenient way to perform a numerical assessment of the acoustic field.
Another problem with the use of the direct solution is associated to the possible presence of discontinuities in the region of noise generation, among the others, shock waves in air and collapse of cavitation bubbles in liquids, producing spurious noise in the solution.
From this point of view, the complete porous formulation which includes the 3D integration over the volume external to the porous surface may be a valid compromise between accuracy and feasibility. From one hand it substantially reduced the dimension of the volume over which the 3D terms must be evaluated, probably making acceptable the computational cost, even in presence of not negligible time delays. From the other hand it allows to embed the possible discontinuities within the porous surface, leaving to the 3D volume integrals the role of correction of the porous solution.
As last observations, we would like to emphasize the independence of the acoustic results

from the time and space resolution herein adopted. The acoustic results here reported are relative to two groups of fluid dynamic data, time-window (a) and (b) described at the end of Section 4.1, used as input data for the acoustic solver. Other data with different time intervals were tested, but results are not showed here. The effectiveness of the acoustic methods proved to be independent on the type of time interval chosen. Moreover, regarding the porous domains, different grids were tested. The finest porous grid is of about 120×10^3 panels and was extracted directly from the fluid dynamic grid. While, the coarser porous grid is of about 60×10^3 panels, the flow data were sampled on the grid by using different interpolation schemes. No difference was observed related to the refinement of the grid or to the interpolation scheme. Finally, we employed the fluid dynamic data obtained using the less accurate coarse grid to carry out an acoustic analysis analogous to the one showed for the fine grid. The discussion for the fine grid holds for coarse grid as well.

Chapter 5

Hydroacoustic noise from different geometries

In spite of the geometrical simplification, the study of hydrodynamic noise generated around simple bodies is significant, because it can exploit fundamental aspects of the topology of the flow field which, in turn, rules generation and propagation of hydrodynamic noise. In this study three elementary geometries were considered, immersed in a flow in the turbulent regime: a sphere, a cube and a prolate spheroid at zero angle of attack. The sphere produces massive separation at the rear of the body and a wake characterized by overlapping of vortex shedding and energetic turbulence generated by a shear layer; the cube behaves similarly to the sphere, apart the substantial difference given by the presence of the sharp corners, which may give a contribution to noise generation; the prolate spheroid is aligned with the main current and develops a small separation region in the leading edge region and a wake much less intense than in the other cases. For sake of comparison, the Reynolds number, based on the square root of the reference (frontal) area, the uniform inlet velocity, and the viscosity, is $Re_A = \sqrt{(A)}U_0/\nu = 4430$ for the three objects. The fluid dynamic field is solved using wall-resolving Large Eddy simulation able to reproduce the energetic part of the energy spectrum, which mostly contributes to the noise (see [47] and [58]). The acoustic field is reconstructed by using the FW-H equation, computing directly the volume (quadrupole) terms.
The chapter is organized as follows. Section 5.1 contains the general features of the numerical setup. Section 5.2 contains: validation of the results for the fluid dynamic field on the sphere together with a test on the acoustic model adopted (subsection 5.2.1), and a comparison of the acoustic far-field generated by the three different objects (subsection 5.2.2)

5.1 Numerical setup

Both fluid dynamic and acoustic fields are solved in the framework of the OpenFOAM® library. A brief description is given at the beginning of section 4.1. The sub-grid scales

for these simulations were modeled according the dynamic Lagrangian model. The PISO algorithm, including the SGS closure, has been customized at the laboratory of Industrial and Environmental Fluid Mechanics (IE-Fluids) of the University of Trieste, and details can be found in [11].
As previously discussed, due to the absence of body motion, to the high value of sound speed and to the small length scale of the body, the compressibility delay $t - \tau$ practically reduces to a time shift homogeneous in space, which does not affect the composition of elementary signals. In fact, after switching off the computation of the compressibility delay, so as to have practically instantaneous source propagation, we noted that results were practically identical. In other words, the body together with its own wake appear as a compact source and the calculation of the delays can be omitted.
We consider three bodies, respectively a sphere, a cube and a 0 angle of attack prolate spheroid. The sphere diameter is $D = 0.01$ m. It is immersed in a water stream with velocity $U_0 = 0.5$ m/s and kinematic viscosity $\nu = 1.0 \times 10^{-6} m^2/s$, so that the Reynolds number based on the sphere diameter D is $Re_D = 5000$. In order to compare the three different geometries, the Reynolds number based on the square root of the reference (frontal) area is the same for the three configurations $Re_A = \sqrt{A} U_0/\nu = 4430$. The side of the cube is $l = 0.008$ m, the minor-axis of the ellipsoid is equal to the sphere diameter D and its major-axis is $6D$.
The computational domain for the sphere and the cube is a box with dimensions $16D \times 16D \times 16D$ along the x, y and z axes respectively. The domain for the prolate spheroid is $24D \times 16D \times 16D$ along the three directions. At the boundaries of the computational domain we set a zero-gradient condition for the pressure but at the outlet, where pressure is set to zero. The velocity is set to U_0 at the inlet, stress-free condition is set at the lateral boundaries and zero gradient condition is set for the velocity components at the outlet.
In order to evaluate the accuracy of the simulations, for the case of the sphere, for which available experimental and numerical reference data are available, two unstructured, body-fitted grids were used: a coarse one (CG) consisting of about 5 millions of cells and a fine one (FG) consisting of about 8 millions of cells. The meshes were built employing the utility of OpenFoam *snappyHexMesh*. In the CG case, the grid spacing normal to the wall for the first layer of cells is $0.001D$ at the body surface directly resolving the viscous sub-layer; a refinement box around the body was considered so as to obtain, in the wake region, a grid size of about $0.1D$ at a distance of $8D$. Out of the region of interest a coarser grid allows the increase of the dimensions of the domain, reducing possible disturbance effects coming from the boundaries. An *A posteriori* analysis showed that about 5 grid points where placed within 10 wall units ($y^* = \nu/u_\tau$ with $u_\tau = \sqrt{\tau_w/\rho_0}$ and τ_w the mean shear stress) off the wall. In the FG case, same conditions were considered in the proximity of the body surface, hence the first layer of cells is $0.001D$, but a refinement was carried out in a rectangular region which embeds the sphere and its wake, up to $9D$ downstream, so as to have a grid size less than $0.05D$ at a distance of $8D$, about 8 grid points within 10 wall units off the body and also smaller grid size in the plane parallel to the body surface. A constant time step $\Delta t = 5 \times 10^{-5}$ s was used for the CG case, whereas it was reduced to $\Delta t = 10^{-5}$ for the FG case. In both cases, the Courant number was kept smaller than

0.5. The flow around the sphere, after about 80 characteristic times D/U_0, was completely developed. After that, statistics were accumulated, collecting the flow data for additional $40D/U_0$ (coarse grid) and $20D/U_0$ (fine grid), sampled every $0.1D/U_0$. The pressure and velocity fields were then employed for the acoustic analysis.
The analysis of the results obtained with the two grids and comparisons with reference data (reported in the next Section) show that the FG was able to give results more accurate than the CG.
For this reason, the cases of the cube and of the prolate spheroid were run using a fine grid of about 8 million cells, built in a way similar to the case of the sphere. For the flow around the cube, the flow data were collected every $0.25D/U_0$ over a period of $20D/U_0$; for the prolate spheroid data collection was performed every $0.2D/U_0$ over a period of $35D/U_0$.
The data obtained in the three cases were employed as input for the acoustic solver. The acoustic analogy was applied to determine the acoustic pressure time-history at different measurement points (named microphones or probes). As mentioned, calculations refer to water. For the acoustic field the fluid density is set to 1000 Kg/m^3, while the speed of sound is equal to 1400 m/s.

5.2 Results

This section is composed of three subsections. The first one describes the main features of the turbulent flow around the sphere and validate our numerical results against the available literature data of [55], [30] and [57] . To test the adequacy of the mesh two different simulations were performed, one on the CG of about 5 million of cells and one on the FG of about 8 million of cells. The subsection also shows the validation of the acoustic solver using LES reference data for the sphere case.
The second subsections contains the analysis of the acoustic far-field produced by the three geometries, at different microphones. The third subsection contains a discussion on qualitatively difference between 2D- and 3D-shaped wakes with respect to the far field noise.

5.2.1 Validation of the fluid dynamic and acoustic solvers - sphere case

The subcritical flow around a sphere undergoes laminar separation near the equator and exhibits an instability appearing as a progressive wave motion with alternate fluctuations produced by the shear at the edge of the separation present in the wake region. The large scale (sinuous) instability of the wake is commonly referred to as “vortex shedding”, though measurements and smoke visualizations of [30] showed no evidence of discrete vortex shedding behind the sphere. The mode associated with the small-scale shear-layer Kelvin–Helmholtz instability at the edge of the recirculation region, is responsible for the distortion of the large-vortex structures, for production of small scales and, eventually, for transition to turbulence in the detached shear layers.
Experiments clearly show that the two instability modes co-exist up to a certain Reynolds number in the subcritical regime, although there is disagreement on its actual value. [1]

did not detect the high frequency mode beyond $Re = 6000$; [59] did not observe it beyond $Re = 1.5 \times 10^4$ whereas [14] were able to capture it at $Re = 3 \times 10^4$. The measurements of [30] and [2] showed the presence of the two modes up to $Re = 10^5$.
The Strouhal number corresponding to the shedding spiral mode remains approximately in the range $0.18 - 0.2$. However, according to the experimental data of [1], in the range $Re = 6 \times 10^3$ to 3×10^4, the Strouhal number rises from $St = 0.125$ to $St = 0.18$. In experimental studies, a higher frequency component is also observable, associated with the development of the Kelvin–Helmholtz instabilities in the detached shear layers, ($St \geq 1.3$). A numerical simulation may need a high level of grid refinement in the shear layer region to detect the small-scale instability, as in the DNS study of [57].
We compare our results obtained with two grids with the reference DNS data of [57] and the experimental data of [30], both at the same value of the Reynolds number as in our case.
Hereafter, quantities averaged in time and over a direction in space are denoted with the symbol $\langle . \rangle$. The mean streamwise velocity $\langle u \rangle$ (made non-dimensional with U_0) along the radial direction, is depicted at three different positions along the x-axis: $x = 0$, $x = 0.5D$ and $x = 2D$ (figure 5.1). As in [57], the mean velocity profiles are calculated over the cross-stream planes $x = const$ averaging over the circumferential direction at constant distance from the axis of symmetry with coordinates $y = 0, z = 0$. Note that the radial direction depicted in the figure does not coincide with that one defined in spherical coordinates. The origin of the Cartesian frame of reference is at the center of the sphere, hence the plane $x = 0$ corresponds to the equatorial plane of the sphere normal to the inlet velocity.
Although the CG is able to give results in reasonable agreement with the DNS data, the FG reproduces much better the velocity profiles. This is particularly true at the equatorial plane where the FG perfectly reproduces the thin boundary layer developing along the wall-normal direction and at the leading edge ($x = 0.5D$). In the wake, a small disagreement is present, which may also be attributed to differences in the geometrical configurations. Specifically, we consider an isolated sphere, whereas in the DNS the authors considered a solid stick supporting the sphere at the rear, likewise in laboratory experiments.
The distribution of the skin friction coefficient $C_\tau = \langle \tau_w \rangle Re/\rho_0 U_0^2$ and of the pressure coefficient $C_p = (p - p_0)/0.5\rho_0 U_0^2$ (p_0 is the pressure at the inlet) around the circumferential direction are in figures 5.2 and 5.3 respectively. These quantities are averaged over time and azimuthal direction. The skin friction coefficient is compared with DNS data of [57]; the comparison is very good also for this quantity for the FG. Conversely, some disagreements appear for the CG case. This occurs both in the region of attached flow as well as in the separation region, where the change of sign of the shear stress is not reproduced with accuracy. The pressure coefficient is compared with experimental data of [30]. In both cases, our LESs reproduce very well the angular distribution of the coefficient as well as of its minimum, well captured at $\theta = 71^o$.
The lift coefficient $Cl = F_y/(0.5\rho_0 U^2 A)$ obtained in our simulations exhibits an oscillatory behavior (figure 5.4, top panel). Here y and z are a couple of mutually orthogonal axes contained in a plane orthogonal to the axis x running along the freestream direction (see figure 5.7). The shape of the signal obtained with the FG suggests the presence of a larger

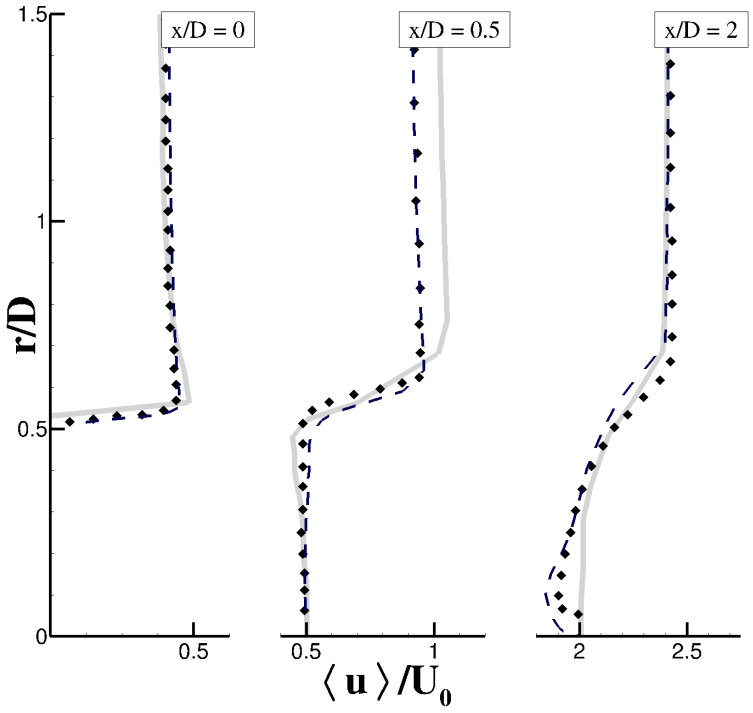

Figure 5.1: Mean streamwise velocity (made nondimensional with U_0) along the radial direction at three different positions along the x-axis: $x = 0$, $x = 0.5D$ and $x = 2D$. CG, solid line; FG, dashed line; DNS results of [57], dots. Note that, according to the notation used in [57], the radial direction runs in planes orthogonal to the x-axis and is centered at the symmetry line $y = 0, z = 0$, like in cylindrical coordinates.

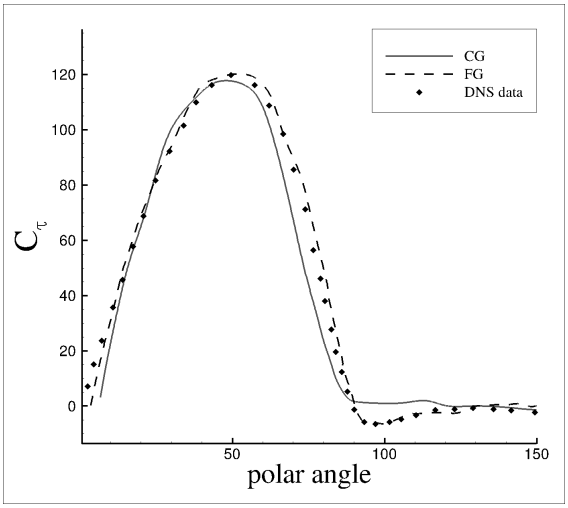

Figure 5.2: Friction coefficient along the circumferential direction expressed in Degrees (0 is the trailing edge, 90 is at the equator, 180 (not shown) is the trailing edge): CG, solid line; FG, dashed line; DNS results of [57], dots.

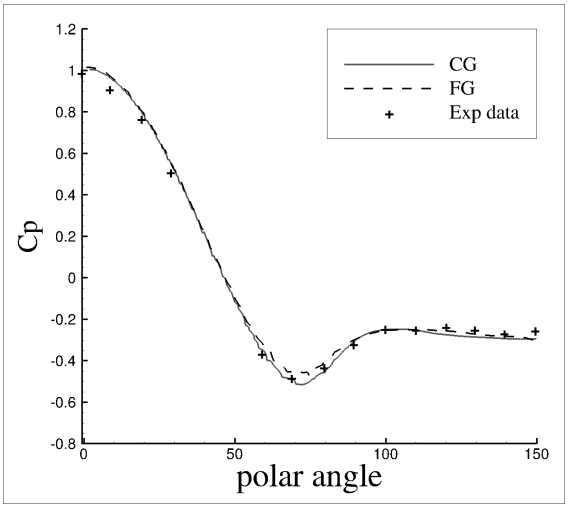

Figure 5.3: Pressure coefficient along the circumferential direction expressed in Degrees (0 is the trailing edge, 90 is at the equator, 180 (not shown) is the trailing edge): CG, solid line; FG, dashed line; experimental data of [30], (crosses).

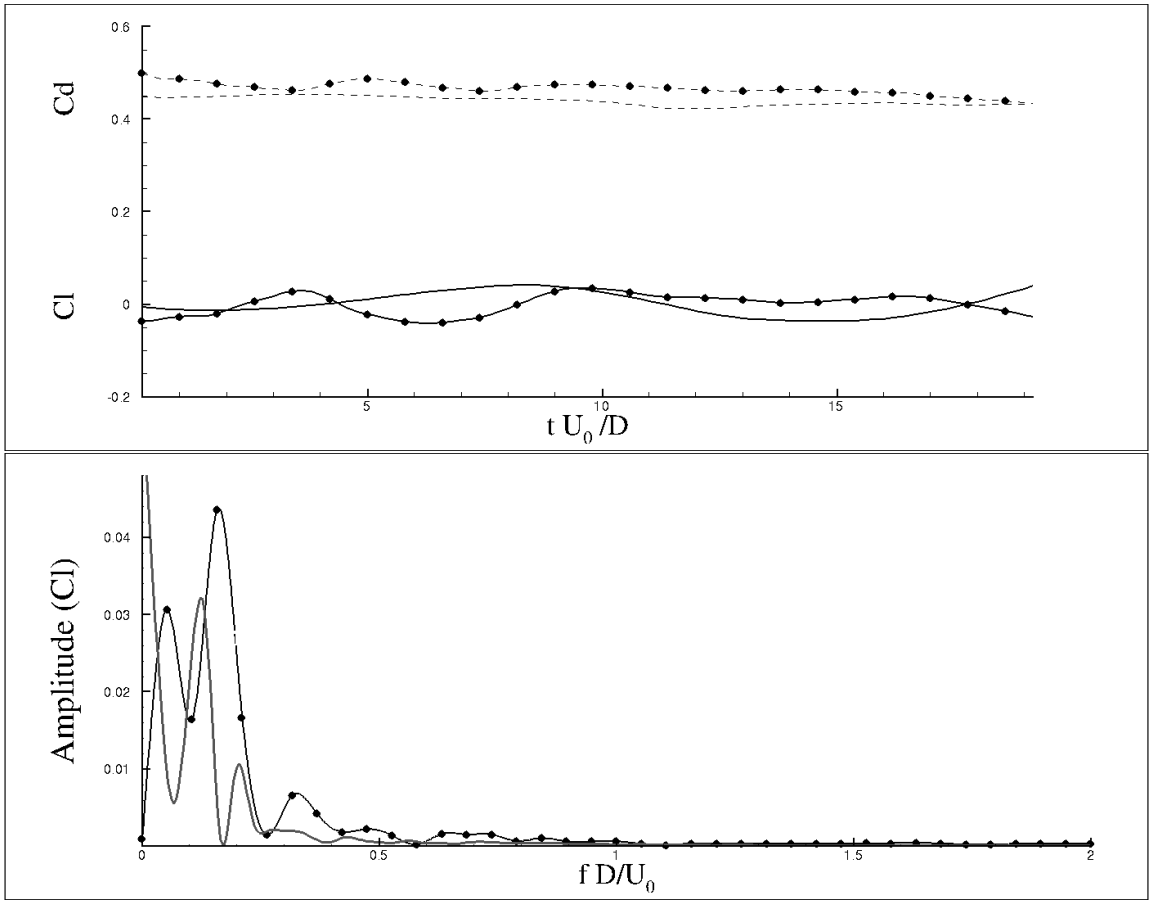

Figure 5.4: Time record of the lift coefficient Cl and drag coefficient Cd for the sphere (top panel). Cl in the frequency domain (bottom panel). CG, lines; FG, lines with dots.

number of discrete frequencies. In fact, figure 5.4 (bottom panel) reveals the presence of three main peaks in case of FG. The three peaks correspond to $St = 0.07, 0.16$ and 0.32. The CG is not able to reproduce such dynamics, giving two main peaks only, corresponding to the values of $St = 0.127$ and 0.2 respectively.
The drag coefficient $C_d = F_x/(0.5\rho_0 U^2 A)$ also exhibits a weakly oscillatory behavior. The mean value of the drag coefficient is 0.47 for the FG and 0.43 for the CG. Both values are in agreement with literature results (in the range 0.4 - 0.5 for Reynolds numbers in the range $10^3 \div 2 \times 10^5$.
To summarize, overall, our LES results exhibit a good agreement with reference DNS and experimental data. As expected, the FG exhibits a better agreement with reference data than the CG. Specifically the FG is able to reproduce a richer frequency contain of the signal. For this reason, the simulation for the other geometries (cube and prolate spheroid) are carried out on a fine grid, shaped likewise the sphere case.

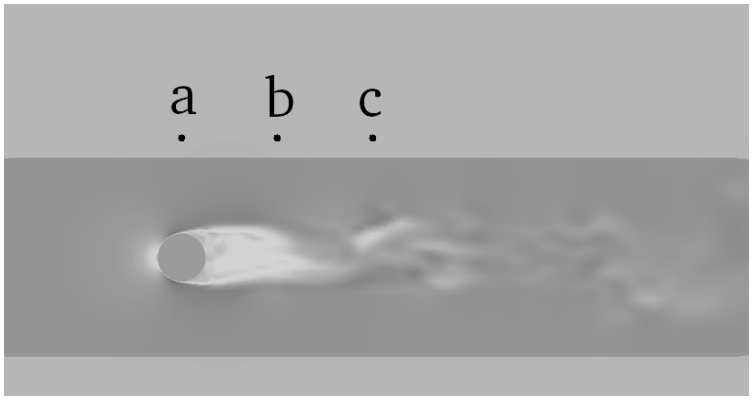

Figure 5.5: Validation tests for the acoustic solver. Longitudinal cut (plane $z = 0$) of the computational domain with a cut of the box (in evidence) used for the volume integration of the quadrupole term: the probes locations are a (0, $2D$, 0), b ($2D$, $2D$, 0) and c ($4D$, $2D$, 0).

For sake of completeness, we repeat some validation tests on the FW-H formulation considering the flow herein investigated. Specifically, we test the acoustic solver by a direct comparison of the pressure signals provided by the FW-H equation with the hydrodynamic pressure provided by LES for three probes with coordinates (0, $2D$, 0), ($2D$, $2D$, 0) and ($4D$, $2D$, 0) respectively. The volume domain considered for solving the quadrupole terms of acoustic equation, that cannot contain the microphone, is sketched in figure 5.5, which shows the section $z = 0$ of the computational domain.
Along the z-axis it is $14D$ long, it covers the entire length along the x-axis, and along the y-axis the domain is $3D$ wide. The volume thus extends up to $0.5D$ from the probes. The results of the validation test are shown in figure 5.6. Specifically we show the spectra level obtained with the two signals. The amplitude is reported in the logarithmic unit decibels (dB). The spectrum level was calculated as $20 \times \log_{10}(FFT(p')/p_{ref})$, where FFT denotes the Fast Fourier Transform of the signal (that was normalized by the number of sample points) and $p_{ref} = 1\mu Pa$ is the reference pressure adopted for underwater sound pressure level measurements. On the left panels we report the comparison for the CG, on the right panels we show the results for the FG. The agreement between the signals is very good in both cases, although in case of FG the reconstruction of the signal appears slightly better, in particular in the range of high frequencies. This is in agreement with the findings of [8] who emphasized the need of fine grids for an accurate reconstruction of the signal.
Hereafter, when referring to LES data for the sphere, we implicitly make reference to those obtained with the fine grid.
Note that the frequency-dependent hearing threshold of human ears in underwater conditions is relatively high, $84 - 100\ dB$, when referenced to $1\,\mu Pa$, and the ambient noise is in the range of $60 - 100\,dB$.

5.2.2 Comparative analysis for the three bodies

First, we show instantaneous streamtracers for the three bodies investigated, to give a qualitative sight of the flow at the rear of the three objects (figure 5.7). Flow separation is substantially different in the three cases: the separation angle on the sphere is about

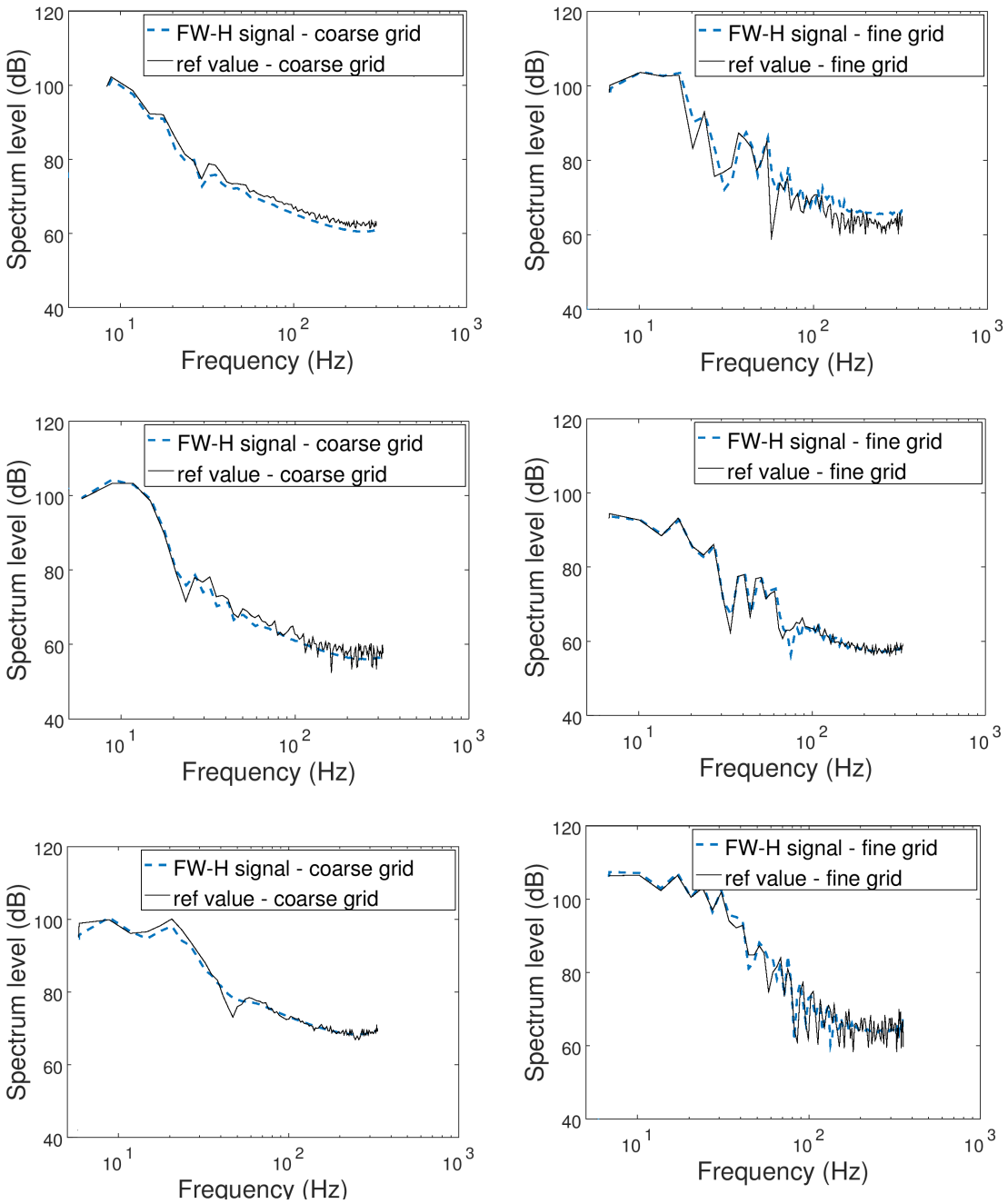

Figure 5.6: Validation tests for the acoustic solver. Sound spectrum level predicted by LES (solid line) and by the FW-H equation (dashed line) at probes: a (0, $2D$, 0), top panel; b ($2D$, $2D$, 0), center panel; c, ($4D$, $2D$, 0) bottom panel.

90^o; the main recirculation beyond the sphere covers a long region up to $x = 2D$ where the mean flow reattaches, while smaller recirculation spots are present in the proximity of the surface. The snapshot captures a large vortex released at the top side of the sphere and a number of small structures close to the body surface, result of the small-scale shear layer developing beyond separation. The flow over the cube separates at the front corners causing a widening of the mean flow which tends to reattach about $1D$ in the downstream region. Small-scale vorticity is appreciable over the free stream-oriented surfaces. Finally, the streamlined profile of the prolate spheroid gives rise to a recirculation region in the very rear part of the body, small compared to that of the previous cases. The main vortex behind the spheroid (depicted in figure 5.7) has a diameter of about $0.28D$ compared to those behind the sphere ($\sim 1D$) and behind the cube ($\sim 0.8D$). The flow over the prolate spheroid separates at $x = 2.7D$, at the ending part of the body.

In order to get a qualitative view of the turbulent wake, contour plots of the resolved turbulent kinetic energy $k = \frac{1}{2}(\langle u'u' \rangle + \langle v'v' \rangle + \langle w'w' \rangle)$ (the symbol $'$ denotes resolved fluctuations) are depicted in figure 5.8. The time window over which the quantity was calculated is not enough to obtain convergent second-order statistics, however, for the scopes of the present paper, the figure gives useful information. Three planes, orthogonal to the flow direction, were selected for this analysis, located respectively at distances D, $3D$ and $6D$ respectively, from the trailing edge of the bodies.

For a certain body, the region of high k intensifies and increases in size moving downstream (panels from the left to the right). At a certain distance from the trailing edge, for the three bodies (panels from the top to the bottom) we observe that the cube produces the highest level of k in a wider region. The intensity of the wake behind the sphere is comparable to that of the cube although a bit smaller in size. The prolate spheroid produces small levels of k over a small region (note the different spatial scales of the bottom panels with respect to the others in figure 5.8). These differences are expected to affect the acoustic signals.

In order to study the acoustic far-field we analyzed the pressure signals reconstructed by the FW-H equation at 6 different probes, whose coordinates are in table 5.1. Two probes are over the longitudinal axis x in the far wake (A_0 and A_1); two over the transversal axis y in the far field (C_0 and C_1) and two over a diagonal oriented at 45 degrees in the $x-y$ plane (B_0 and B_1), in the far field. The domain considered to compute the quadrupole terms of the FW-H equation is the volume centered over the body and enclosed in a box with dimension $12D \times 12D$ in the y, z directions, and running along the entire computational domain along the x-axis.

The time-signals of the bluff bodies turn out to be the most intense and richest in frequencies (figure 5.9). The sphere and cube produce equivalent far-field noise. The noise radiated by the prolate spheroid is substantially smaller than that of the other bodies.

As well known, the FW-H equation consists of a sum of linear terms, related to the integration on the body surface (loading noise), and nonlinear terms, corresponding to a volume integration on the flow-source region. Thus, it may be interesting to evaluate the separate contributions coming from the different terms.

We show the spectrum level from the linear source terms in figure 5.10 and from the nonlinear sources in figure 5.11 respectively. Overall, the analysis of figure 5.10 suggests that the

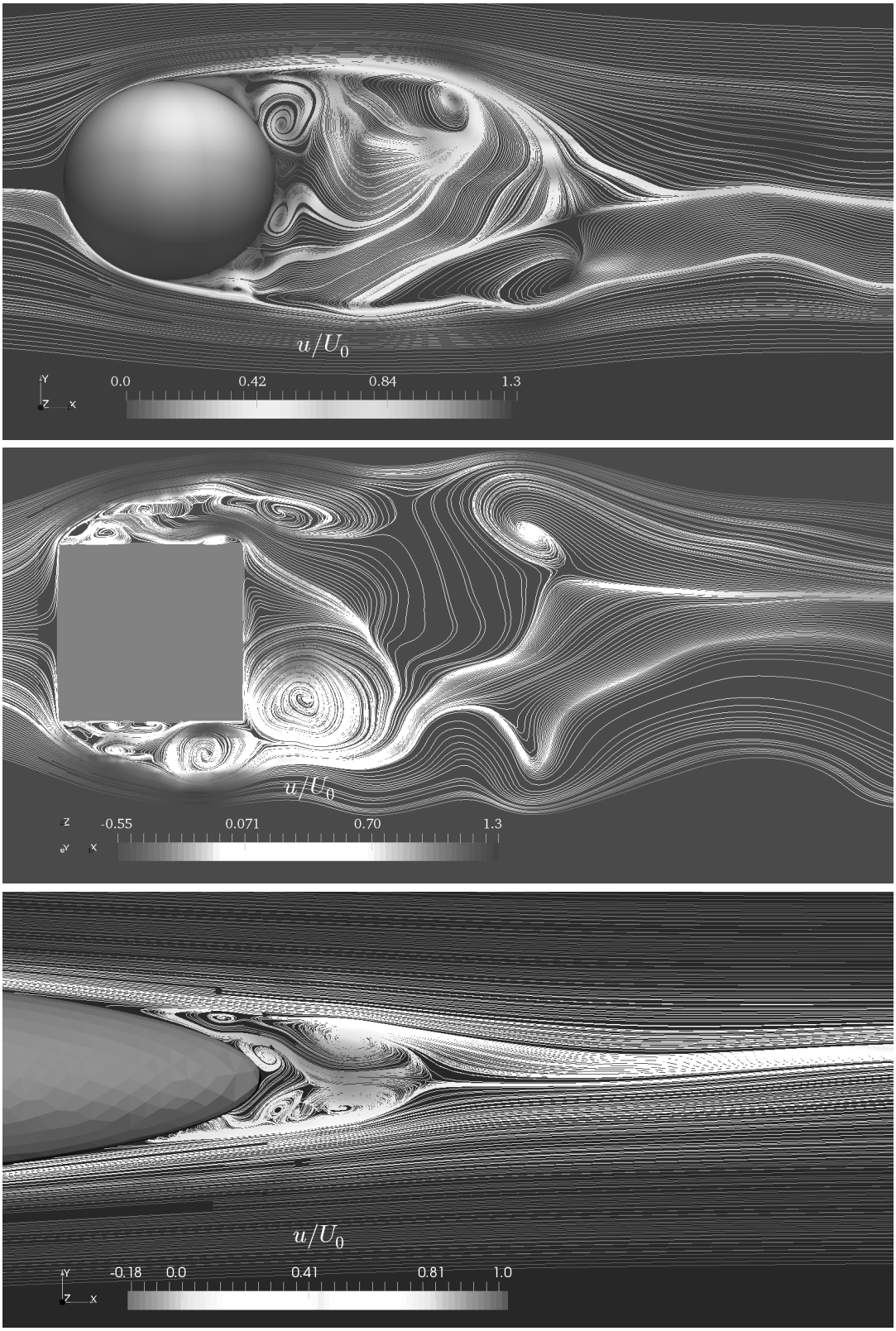

Figure 5.7: Snapshots of the flow around sphere (top panel), cube (middle panel) and prolate spheroid (bottom panel). Instantaneous streamtracers together with contour of the streamwise velocity, made non-dimensional with the inflow velocity U_0.

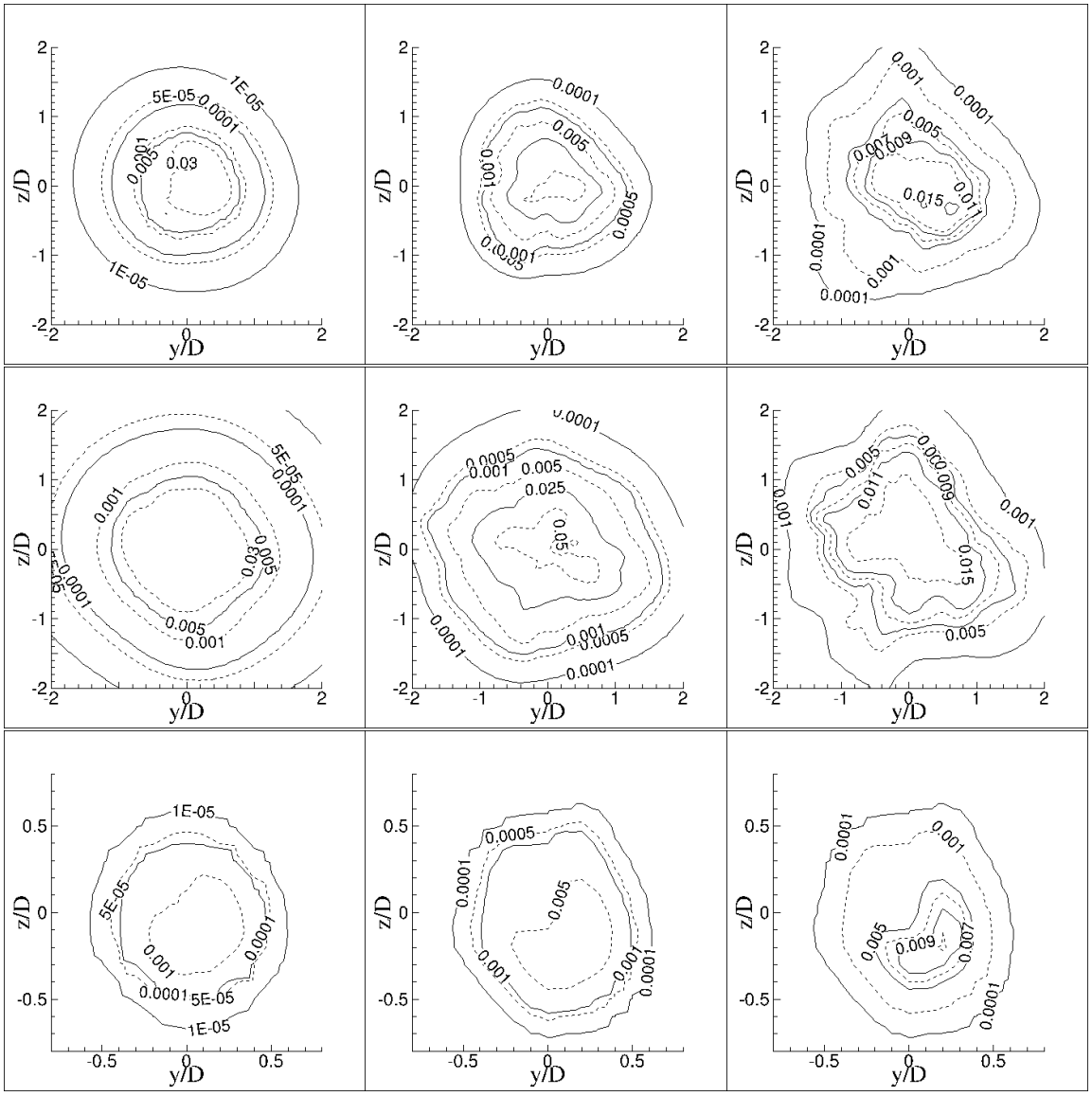

Figure 5.8: Contouring of the resolved non-dimensional turbulent kinetic energy k/U_0^2 over three planes orthogonal to the streamwise direction, at a distances $x = D$, $3D$, and $6D$ from the trailing edge of the bodies (from left to right panels): Sphere (top panels); cube (middle panels); prolate spheroid (bottom panels).

loading noise deriving from the bluff bodies is substantially larger than that coming from the streamlined body, thus confirming that its elongated, hydrodynamic shape produces a very low (loading) noise. This occurs at all probe positions investigated. Further, the energy content in the high frequencies appears a bit larger in the case of the cube than for the sphere. This may be the effect of the small scale vorticity developing because of the sharp corners. In fact, the high frequencies appear more the linear part of the signal, while nonlinear terms seem to provide mainly low frequencies.
The sound spectrum level of the non-linear part of the signal (figure 5.11) gives information on the sound level mostly generated by the wakes developing downstream. The loudness of the wakes appear comparable among the three cases downstream the bodies in the far wake (microphones A_0 and A_1). Conversely, at noticeable distance from the bodies, along the transversal directions (microphones B_1 to C_2), the wakes generated by the bluff bodies appear more loudly than that of the prolate spheroid. This suggests a sort of directivity of the noise generated by the hydrodinamically streamlined body, compared to the two cases of bluff bodies.
Finally, we observe that, for bluff bodies, the linear contribution to the far field noise is always more significant than its non-linear counterpart. The opposite is true for the prolate spheroid, due to the very weak loading noise generated by this body. In general, this behavior may be explained by referring to the FW-H equation, where, as well known, the far field components of linear terms decay as $1/r$ (r being the source-observer distance), while the decay of the nonlinear source contributions is notoriously much faster.

	A0	A1	B0	B1	C0	C1
x	50D	100D	50D	100D	0	0
y	0	0	50D	100D	50D	100D

Table 5.1: Coordinates of probes at $z = 0$ placed in the far field for the analysis of the radiated noise.

5.2.3 Cube versus square cylinder

This section is devoted to a preliminary comparison between the hydroacoustic field generated by the cube, as presented in the previous section, and by an elongated cylinder with a squared section, studied in the previous chapter 4.
It has to be pointed out that in the cylinder case the acoustic analysis of the pressure signals was carried out considering air as a medium. Also, the inlet velocity as well as the dimension of the body were different from those of the cube. Consequently, for making the present comparison consistent, first we re-processed the pressure signal relative to the cylinder considering water as the carrying fluid. Then we present the results in non-dimensional form, thus showing the spectrum of the pressure made non dimensional with $\rho_0 U_0^2$ as a function of the non-dimensional frequency fd/U_0.
Figure 5.12 shows a comparison between velocity fields determined in fully developed conditions for the two cases. Specifically, the comparison is shown on the longitudinal $x - y$

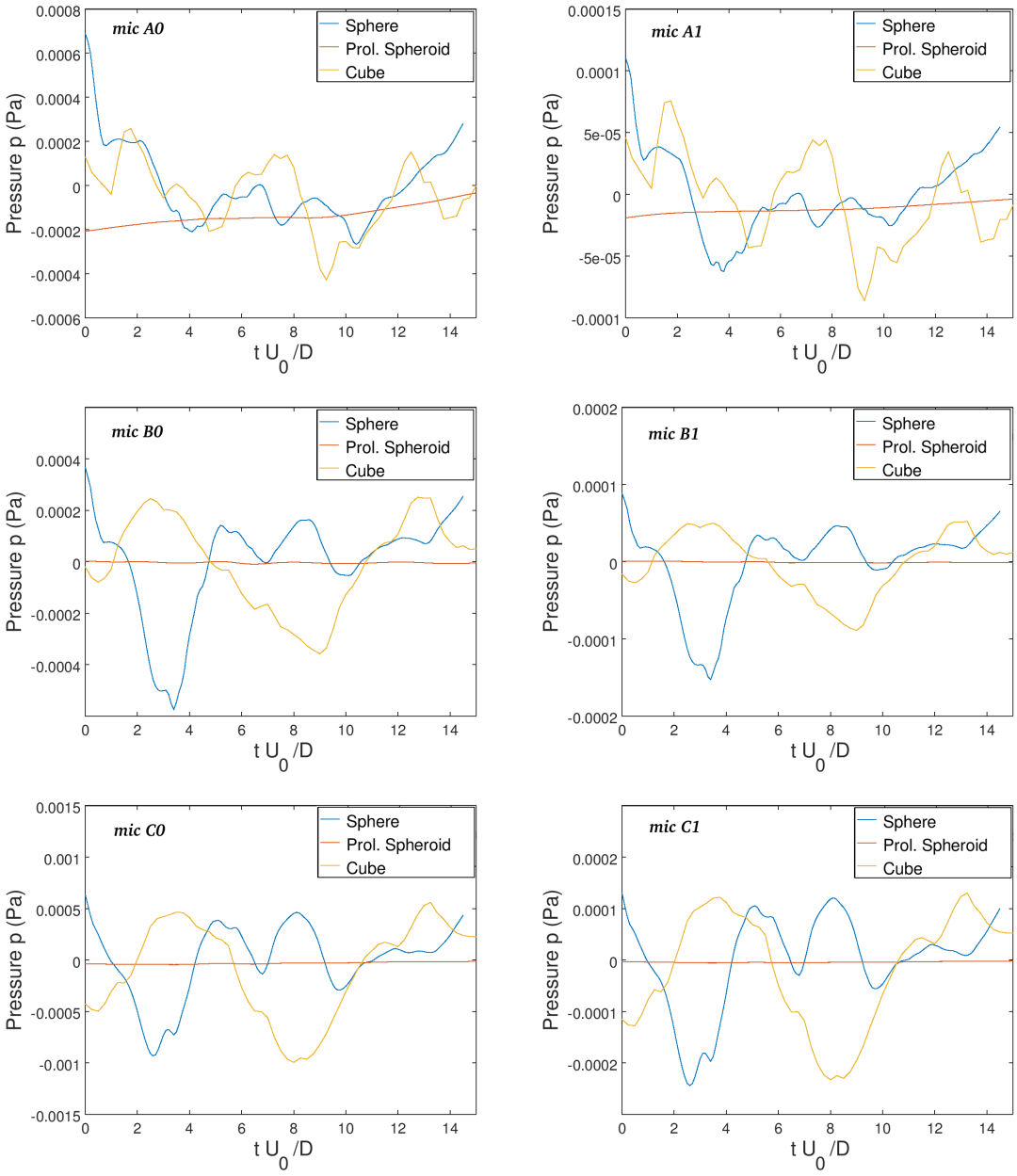

Figure 5.9: Pressure signal reconstructed by the FW-H equation at 6 different probes $A0, .., C1$, their coordinates are in table 5.1.

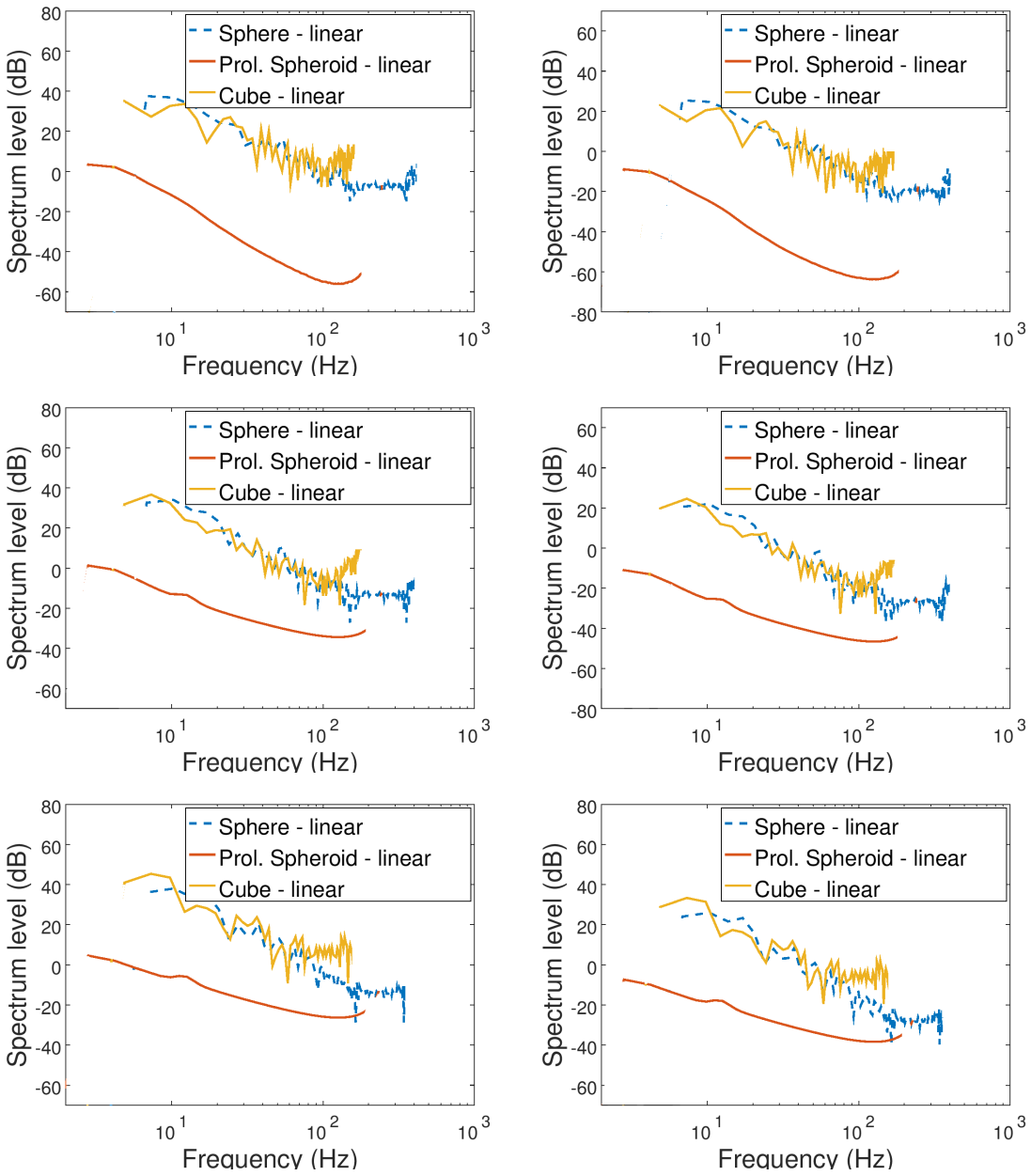

Figure 5.10: Sound spectrum level of the linear terms of FW-H in at all probes probes of table 5.1.

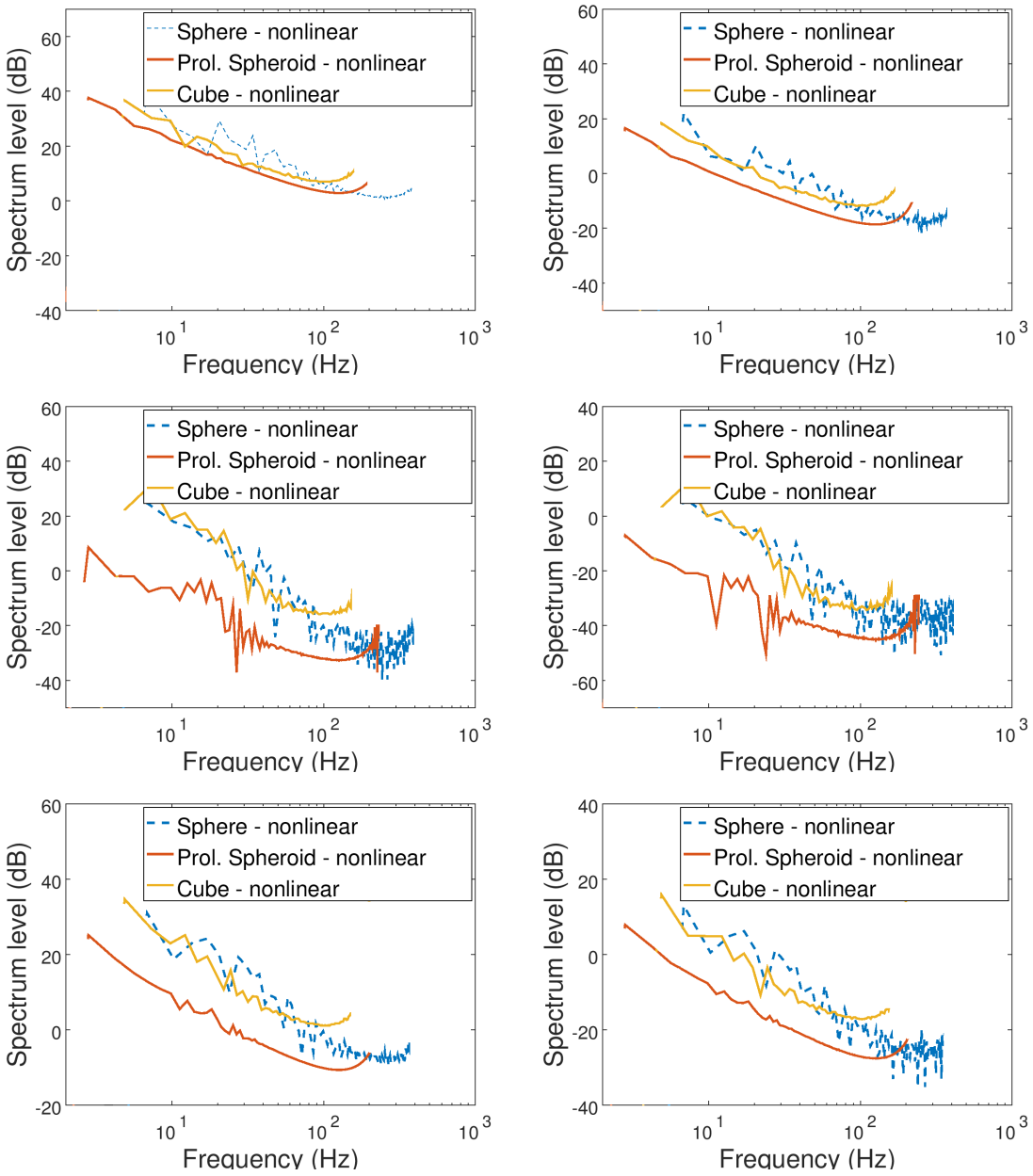

Figure 5.11: Sound spectrum level of the non-linear terms of FW-H in at all probes probes of table 5.1.

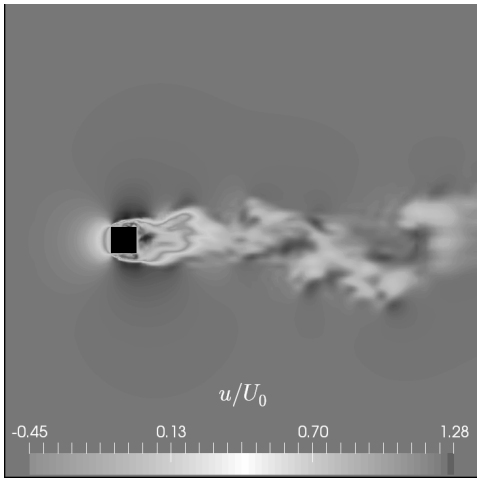

Figure 5.12: Comparison of instantaneous streamwise velocity u, made non-dimensional by the inlet uniform velocity U_0, in the case of a flow around a cube (left panel) and flow around a square cylinder (bottom panel).

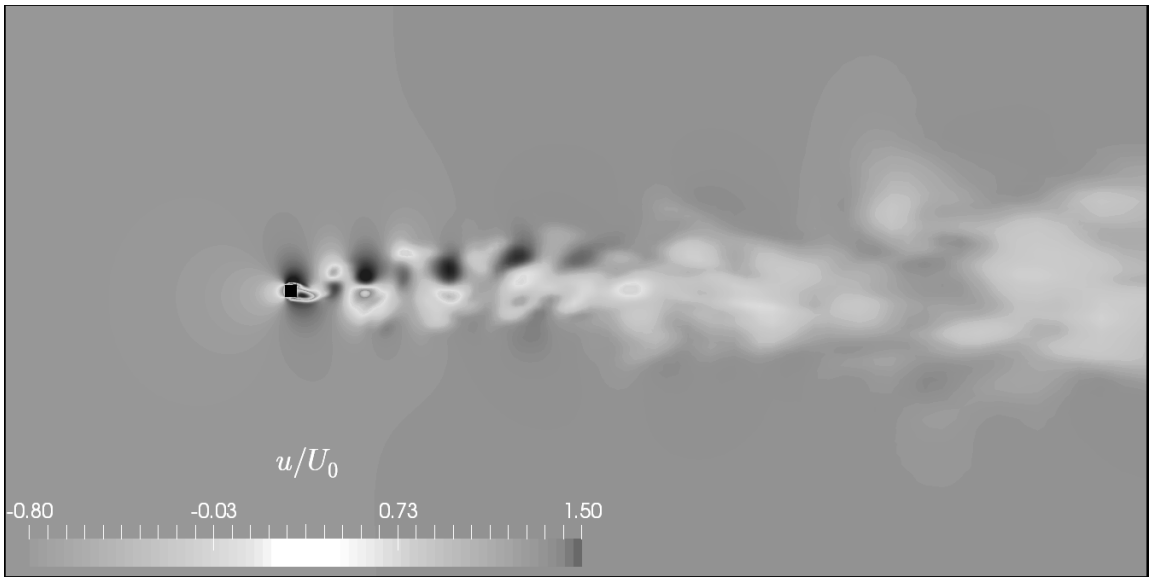

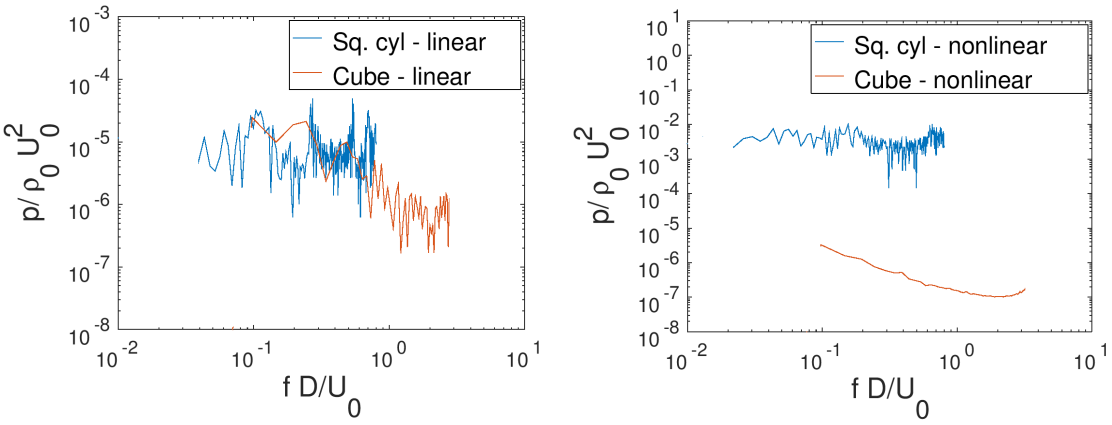

Figure 5.13: Comparison of linear terms (left panel) and nonlinear terms (right panel) of the FW-H reconstructed signal in the frequency domain, at a distance of $100D$ (probe $A1$ in table 5.1). Case of a flow around the cube (dash dot line) and a square cylinder (solid line).

mid-plane of the two computational domains. As expected, in the mid-section the flow downstream the cylinder is characterized by the presence of a persisting and oscillating wake, which becomes progressively wider and finally breaks, turning into a rather chaotic and turbulent flow. On the other hand, the wake behind the cube is more irregular and, above all, spreads out much earlier in the field, thus providing a much weaker occurrence of nonlinear noise sources in a region limited in space.
Figure 5.13 shows a comparison between the noise non-dimensional spectra at probe $A1$ (located $100D$ downstream of the body), corresponding to both linear (left panel) and nonlinear (right panel) FW-H source terms. Apart the extent of the spectra in the frequency domain, related, from one side, to the extension of the available time window and, from the other side, to the sampling time interval, the figures give very useful information. The loading terms given by the two bodies overlap in the regions of non-dimensional frequencies in common. This is not surprising, since the loading term is mainly related to the shape of the cross-sectional section that, in the two cases investigated is the same (a square). On the other side, substantial differences are observed in the non-dimensional spectra of the non-linear quadrupole terms, the signal given by the wake of the cylinder being much larger than that given by the cube. This has to be attributed to the energy content of the 2D-shaped wake developing behind the cylinder, when compared to the 3D-shaped wake developing around the cube. This important aspect will be exploited in a successive work.

Chapter 6

Hydroacoustic noise from cavitating flows

This chapter is dedicated to preliminary considerations on the modeling of pressure disturbance that may propagate from cavitating flows and results from simplified cases are discussed from a qualitative point of view. The dynamics of vapor bubble forming and collapsing within a flow requires many assumptions that force both theoretical and numerical models to approximate several physical mechanisms. The main assumptions which have been made for the present study are: vapor bubbles are spherical, the temperature is constant, the distribution of bubble is uniform in space and phenomena of coalescence or collision of bubbles are absent.
In the present study, three steps are proposed, to analyze the complex mechanisms related to cavitation noise and to discuss the numerical results of a cavitating flow around an hydrofoil. First, we present dynamics and acoustics related to a single bubble whose oscillatory motion is ruled by the Rayleigh-Plesset equation. Then, a collection of bubbles constituting of a symmetrical spherical cloud is considered, whose behavior is strictly related to the single bubble motion. Last step introduces the mixture model, in which the vapor growth is based on the bubble dynamics, derived from the Rayleigh-Plesset equation. The mixture model is applied for the case of a cavitating flow around an hydrofoil. The pressure signals observed in the hydrofoil case are found to be related to those observed in the case of the single bubble and the bubble cloud. In particular, the bubble rebounds characterize the bubble noise as well as the rebounds of the vapor cavity characterize the cavitating hydrofoil noise signal.
The chapter is organized as follow: before describing the equations of the mixture model adopted to reproduce the cavitating flow (section 6.2) a brief introduction is given (section 6.1) about physics concerning the formation of bubbles in a liquid medium and about alternative methods of modeling this type of multiphase flow. In section 6.3 and 6.4 dynamics and acoustics of a single isolated bubble and of bubble cloud respectively are briefly presented and discussed; section 6.5 is devoted to some details of the adopted multiphase solver and the numerical results for a cavitating flow around a hydrofoil, at

different Reynolds and cavitation numbers.

6.1 Physical aspects of sheet and cloud cavitation

The cavitation phenomenon can be interpreted as the rupture of the liquid continuum due to excessive stresses. The liquid to vapor transition may be obtained either by heating the liquid at constant pressure, which is well known as boiling, or by decreasing the pressure in the liquid at constant temperature.
In practice, if a liquid at constant temperature is subject to a decreasing pressure p below the saturated vapor pressure p_v the transition to vapor occurs. The value of $(p - p_v)$ is called the tension, and the magnitude at which rupture occurs is the tensile strength of the liquid [6].
The (instantaneous) formation of vapor cavities in a liquid is generally initiated from microscopic nuclei carried by the flow. Such nuclei are points of weakness for the liquid from which macroscopic cavities are generated and grow in low pressure regions.
The simplest and most widely used model of nucleus is that of a micro-bubble. Such a micro-bubble, typically of a few microns in diameter, is assumed to be spherical and to contain a gaseous mixture made of the vapor of the liquid and possibly of non condensable gas.
It is well-known that ordinary water contains dissolved air (essentially oxygen and nitrogen) at least if no special degassing procedure is applied to it.
In any practical experiment or application (see among others [19, 24]), weaknesses can typically occur in two forms. The thermal motions within the liquid form temporary, microscopic voids that can constitute the nuclei necessary for rupture and growth to macroscopic bubbles. This is termed homogeneous nucleation. In practical engineering situations it is much commoner to find that the major weaknesses occur at the boundary between the liquid and the solid wall of the container or between the liquid and small particles suspended in the liquid. When rupture occurs at such sites, it is termed heterogeneous nucleation.
While it may be possible to remove most of these nuclei from a small research laboratory sample, their presence dominates most engineering applications.
The important fact concerning the liquid weakness is that the different nuclei concentration is significant for the inception and development of cavitation. To make comparisons of the initial/background conditions of ambient liquid created in the experimental laboratories, a non-dimensional parameter was introduced: $\sigma = (p_0 - p_v)/0.5 * \rho_L U^2$ which is named cavitation number. It is a measure for the sensitivity of the flow for cavitation to occur and is useful to facilitate the comparison of results from experiments and numerical simulations. A higher cavitation number indicates that the pressure in the flow must decrease more before cavitation occurs. A smaller cavitation number indicates that a smaller decrease in pressure causes cavitation. Thus, a low cavitation number corresponds to a high susceptibility for cavitation.
The Rayleigh-Plesset (RP) equation [50] describes the time evolution of the bubble radius when the bubble lies in an infinite domain. The equation simply represents the equilibrium

of the stress at the interface between gas and liquid. In order to obtain the RP equation, the mass and momentum conservation equations in both fluids are considered and the stress equilibrium at the interface is then written. The driving term is the time evolution of the liquid pressure at infinity $p_\infty(t)$. Initial bubble radius R_0 needs to be specified as well as the initial interface velocity $\dot{R}$ often chosen equal to zero as it is the case if the bubble is initially in equilibrium. There is no solution in closed form for the Rayleigh-Plesset equation, but accurate numerical solutions can be easily obtained.

6.2 Mixture model

Numerical techniques frequently used for simulating a limited number of bubbles can be subdivided based on how they treat the interface between the liquid and the gas. Interface tracking techniques place grid nodes on the interface and the grid is thus deformed by the bubble motion. Conversely, interface capturing techniques employ a static grid and therefore do not place grid points on the interface, but they reconstruct the interface from a marker in the flow field. Although the former techniques provide a sharper and precise representation of the interface, they turn out to be impractical whether the vapor cavity consists of a multitude of bubbles that may be also smaller than a computational cell.
Homogeneous-mixture assumes that vapor phase is very finely dispersed within the liquid phase. Many bubbly flows come close to this limit and can, to a first approximation, be considered to be homogeneous. In fact, the two phases could, in theory, be sufficiently well mixed and the disperse particle size sufficiently small so as to eliminate any significant relative motion.
To summarize, the main assumptions of the mixture model here adopted are: the vapor phase is very finely dispersed within the water phase, the relative motion between liquid and vapor phases is neglected, the two phases are in thermodynamic and mechanical equilibrium, the liquid vapor mixture is treated as an homogeneous medium with variable density ρ_m and viscosity μ_m, being

$$\begin{aligned} \alpha_v &= \frac{V_v}{V} \\ \rho_m &= \rho_L(1-\alpha_v) + \alpha_v\rho_v \\ \mu_m &= \mu_L(1-\alpha_v) + \mu_v\rho_v \end{aligned}$$

where V is a volume element of fluid and V_v is the volume of vapor contained in V, α_v is named the vapor fraction, the subscript L and v indicate that the constant quantities (ρ or μ) refer to liquid or vapor phase respectively.
The solver is available in OpenFoam (named *InterPhaseChangeFoam*) for incompressible, isothermal immiscible fluids with phase-change. It employs a VoF phase-fraction based interface capturing approach. It solves the continuity and momentum equations for the

mixture

$$\frac{\partial \rho_m}{\partial t} + \frac{\partial}{\partial x_i}(\rho_m u_i) = 0,$$
$$\frac{\partial}{\partial t}(\rho_m u_i) + \frac{\partial}{\partial x_j}(\rho_m u_i u_j) = -\frac{\partial p \delta_{ij}}{\partial x_j} + \frac{\partial \tau_{ij}}{\partial x_j} + f_\sigma,$$

being $f_\sigma = sk\nabla\alpha_v$ the surface tension force,

and a transport equation for α_v

$$\frac{\partial \alpha_v}{\partial t} + \frac{\partial \alpha_v u_i}{\partial x_i} + \frac{\partial \alpha_v (1-\alpha_v) U_c}{\partial x_i} = m^+ + m^- \tag{6.1}$$

being U_c the interface-compression velocity which will be discussed in section 6.5.1. The two terms on the RHS are source/sink terms, they describe the phenomena of vaporization and condensation. In literature different models for the source/sink terms are available; we adopted the one proposed by Sauer *et al.* [56], which relates them to the variation of the bubbles radius by using the Rayleigh-Plesset equation [50, 48]. Further details on the multiphase solver adopted for the numerical experiments are reported in section 6.5.

6.3 Single bubble

The dynamics of a single, spherical bubble immersed in a incompressible fluid can be modeled by a nonlinear differential equation of second order, known as the Rayleigh-Plesset equation. The radius of the spherical bubble, assuming constant temperature, varies in time $R(t)$ according to the equation

$$\rho_L \left(R(t)\frac{\partial^2 R(t)}{\partial t^2} + \frac{3}{2}\left(\frac{\partial R(t)}{\partial t}\right)^2 \right) = \tag{6.2}$$
$$\left(p_0 - p_v + \frac{2s}{R_0}\right)\left(\frac{R_0}{R(t)}\right)^{3\gamma} - \frac{2s}{R(t)} - 4\mu\frac{1}{R(t)}\frac{\partial R(t)}{\partial t} + p_v - p_0 - \Delta p(t),$$

where R_0 and p_0 are the bubble radius and the fluid pressure at undisturbed (reference) conditions, respectively, ρ_L is the density of the liquid, μ is the dynamic viscosity, s is the surface tension, γ is the polytropic index for the gas inside the bubbles and $\Delta p(t)$ is the imposed driving pressure at infinity. Under equilibrium conditions $\Delta p(t) = 0$, the pressure inside the liquid surrounding the bubble is p_0.
The outer pressure varies in time as

$$\Delta p(t) = \Delta p_0 \sin(2\pi f_{exc} t), \tag{6.3}$$

Table 6.1: Characteristic values of gas (air) and surrounding liquid (water) that have been used for the simulation.

Initial radius	R_0	$1.4\,\mu m$
Liquid pressure	p_0	$100\,kPa$
Liquid density	ρ_L	$998\,Kg/m^3$
Dynamic viscosity	μ	$1\,mPa$
Vapour pressure	p_v	$5945\,Pa$
Surface tension	s	$72.5\,mN/m$
Polytropic exponent	γ	1

where $\Delta p_0 = 36kPa$ and the resonance frequency $f_{exc} = 1260kHz$. The values used for the simulation are listed in the Table 6.1, where the value $\gamma = 1$ corresponds to an adiabatic behavior.
The values $R(t+\Delta t)$ and $\dot{R}(t+\Delta t)$ are calculated using Taylor's series expansion of the solution at the previous time step $R(t)$, $\dot{R}(t)$, and $\ddot{R}(t)$; then equation (6.2) is used to find $\ddot{R}(t+\Delta t)$. The program automatically adjusts the time steps to ensure that the fractional change in bubble radius between two subsequent steps does not exceed 5%.
In Figure 6.1 the evolution of the bubble radius over time is depicted for the case of the imposed harmonic pressure wave given in eq. (6.3). The difference between top and bottom panel of figure 6.1 lies in the duration of the imposed external pressure, in particular:

a) the top panel figure shows the response of the bubble to a single sinusoidal oscillation of $\Delta p(t)$, that is $\Delta p(t) = 0$ for $t > 1/f_{exc}$. It is noticeable the distinct resonant behavior of the micro-bubble which rebounds according its natural frequency;

b) the bottom panel figure shows the response of the bubble to a continuous sinusoidal pressure, meaning that $\Delta p(t)$ behaves as in eq. (6.3) for any time t. In this case, a second lower frequency appears, and makes the maximum value of radius, reached at every rebound, fluctuating (oscillating) as well.

The acoustic pressure disturbance generated by the oscillating bubble can be written according to FW-H equation, neglecting the contribution of volume sources, that is including only the thickness and loading terms. Moreover, in most cases, far field acoustic pressure from bubbles or cavities is due to rapid oscillations of their volume which is represented by the thickness term alone. This is responsible for the monopole character of the far field bubble noise. Considering the system as instantaneous, (a reasonable assumption, due to the high sound speed underwater and the small source length scale), we may approximate the far field acoustic pressure as

$$P_a = \frac{\rho_L}{4\pi}\frac{\partial}{\partial t}\int_{\partial V}\frac{u_n}{r}dS, \tag{6.4}$$

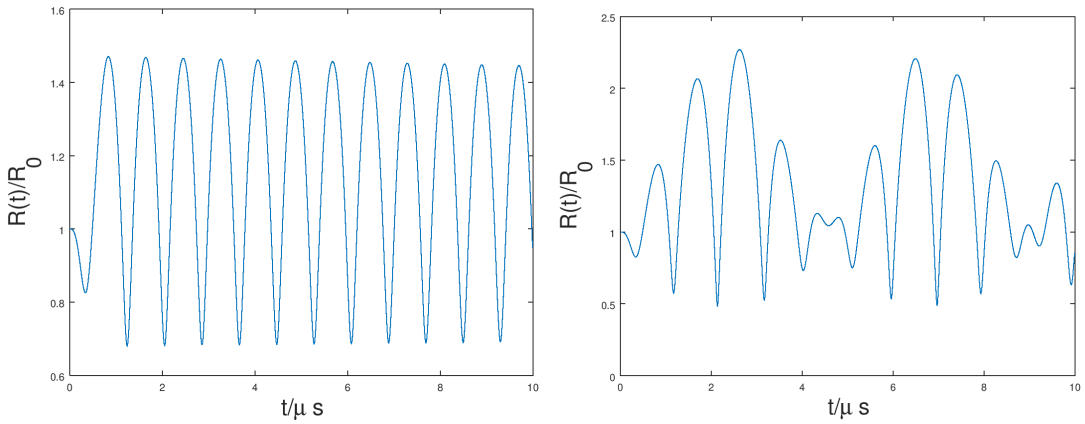

Figure 6.1: Normalized bubble radius $R(t)/R_0$ excited by harmonic pressure wave given by equation (6.3). If the imposed pressure is zero for $t > f_{exc}$ the bubble oscillates symmetrically in time (left panel). If the external pressure persists for any time t a lower frequency characterizes the resulting radius oscillation (right panel).

where $\partial V = S$ is the bubble surface, u_n is the bubble velocity projected along the outward normal to the bubble surface and r is the source-observer distance. The velocity of the bubble oscillation is expressed as the time derivative of the radius $u_n = \dot{R}$, thus from eq. (6.4) we obtain

$$P_a = \frac{\rho_L}{4\pi}\frac{\partial}{\partial t}\frac{1}{r}\left[\frac{\partial R}{\partial t}4\pi R^2\right] = \frac{\rho_L}{r}\left[\frac{\partial^2 R}{\partial t^2}R^2 + 2R\frac{\partial R}{\partial t}\right]. \tag{6.5}$$

The acoustic pressure P_a is evaluated for the oscillating bubble of figure 6.1: the two cases, left and right panel respectively, are depicted in figure 6.2. The observer is at a distance $r = 0.001m$ from the bubble center. The typical pressure field behavior (see for example [6]) is computed correctly, since (as expected) each volumetric rebound of the bubble causes an acoustic peak. The radial symmetry of the velocity field u_n characterizes the acoustic field as a monopole field; it is worth noting that by accounting for a deformation of the spherical symmetry, the pressure field would probably characterized by a specific directivity.

6.4 Bubble cloud

In this section we deal with a simplified ensemble of bubbles which are enclosed in a spherical domain. The modeling of dynamics and acoustics is quite similar to the one described in the previous section, but it refers to a spherical cloud of bubbles. Some assumptions are needed, to gradually address the complex physics of the problem. Specifically, the relative motion and the mass transfer between the two phases (bubble gas/vapor and surrounding liquid) are neglected. The population of bubbles per unit liquid volume η, within the cloud, is assumed uniform initially and there is no coalescence or break-up of bubbles. Since the

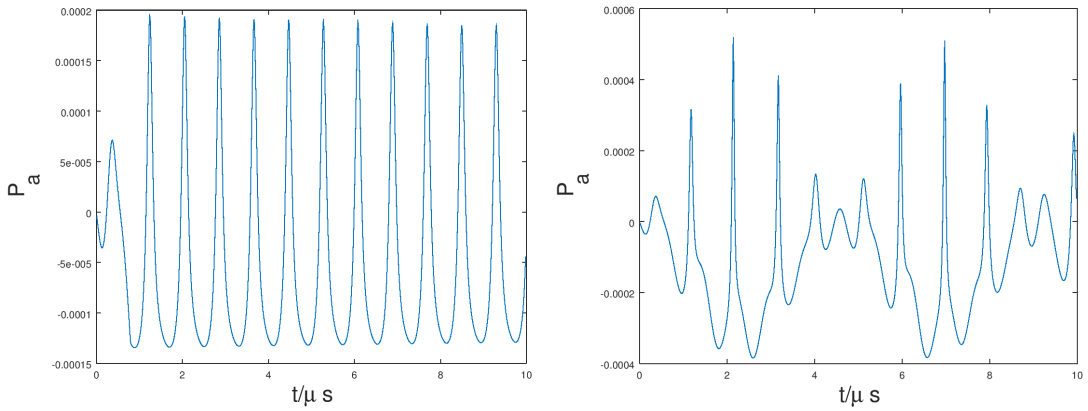

Figure 6.2: Far field acoustic pressure P_a evaluated according eq. (6.5) of oscillating bubble of figure 6.1, left and right panel respectively.

relative motion and coalescence phenomena are neglected, it follows that η is constant and uniform within the cloud in time. The equations here adopted are those derived in [16] and [64]. The continuity and momentum equations for the one-dimensional spherical bubbly mixture are rewritten in an integral form, in terms of the Lagrangian coordinate (r_0, t), where r_0 is the (non-dimensional) initial radial position at time $t = 0$. The equations for the cloud dynamics are

$$\begin{aligned} r(r_0,t) =& \left[\frac{3}{3+4\pi\eta}\int_0^{r_0}(3+4\pi\eta R^3(\xi,t)\xi^2 d\xi\right]^{1/3}, \\ u(r_0,t) =& \frac{12\pi\eta}{(3+4\pi\eta)r^2(r_0,t)}\int_0^{r_0}\frac{\partial R(\xi,t)}{\partial t}R^2(\xi,t)\xi^2 d\xi. \end{aligned} \tag{6.6}$$

In eq. (6.6) the variable r is the Eulerian radial coordinate measured from the center of the cloud, r_0 is the Lagrangian radial coordinate measured from the center of the cloud and u is the radial velocity of the fluid. The parameter η may be expressed in terms of the void fraction $\eta = \alpha/(1-\alpha\tau)$.
The dynamics of the bubbles within the cloud is always ruled by (6.1); nevertheless, in this case:

- the dynamic viscosity μ is replaced by the dynamic viscosity of the mixture μ_E,
- the time derivative $\partial/\partial t$ is replaced by the material derivative $D/Dt = \partial/\partial t + u\partial/\partial r$.
- the external pressure $\Delta p(t)$ is replaced by the pressure field $p = p(r_0, t)$.

The pressure field p, which varies along the radial direction and in time, is obtained by solving the equation of motion:

$$\rho\frac{Du}{Dt} = -(1+\eta\tau)\nabla p. \tag{6.7}$$

where $\tau = 4\pi R^3/3$ is the bubble volume. The boundary condition for the pressure p is given by an harmonic pressure wave $Cp_{inf}(t)$, external to the bubble cloud:

$$Cp_{inf}(t) = \begin{cases} \Delta p_0[\cos(2\pi f_{exc} t) - 1]\,; & 0 < t \leq 1/f_{exc} \\ 0\,; & t > 1/f_{exc}, \end{cases} \tag{6.8}$$

where f_{exc} coincides with the frequency adopted for the single bubble case and $\Delta p_0 = 6kPa$. Different values were chosen for the external harmonic pressure Cp_{inf}, the effective viscosity μ_E and the void fraction α, and a strong dependence of the bubble cloud dynamics on their variation has been observed. However, the in-depth analysis of the complex dynamics of the bubble ensemble is beyond the scope of this thesis and we limit our attention to a single test case whose parameters are listed in Table 6.2 (in addition to those already expressed in Table 6.1); note that the initial cloud radius is set to $A_0 = 100R_0$. As already mentioned in [64], the characteristics of the growth of the cloud are similar to those of the bubbles within the cloud and all the bubbles grow almost in phase. Instead, comparing bubble cloud behavior with that of a single isolated bubble (see previous section) a substantial difference was found to be related to the dissipative action of the effective viscosity of the mixture. The oscillations of the bubbles within the cloud (and consequently of the cloud itself) are damped by the high viscosity μ_E, as showed in Figure 6.3 (left panel), where the time history of the cloud radius $A(t) = r(A_0, t)$ is reported.
For what concerns the acoustic noise generated by the spherical cloud, the same observations and arguments made for the single bubble apply. With reference to the FW-H equation, the only contribution to the acoustic (far) field is provided by the thickness noise term, which is related to the motion of the cloud surface. Thus, by applying eq. (6.4), where $S = 4\pi A(t)^2$ and $u = u(A_0, t)$ now represent the cloud surface extension and velocity respectively, we obtain a pressure disturbance which is strictly related to the cloud rebounds, see Figure 6.3 (right panel). Further experiments should investigate on the acoustic frequency dependence from the different parameters involved, the rate of dissipation due to the effective viscosity, which is related to the number of bubble within the cloud.

Table 6.2: Characteristic values used for the bubble cloud simulation.

Initial bubble radius	R_0	$1.4\,\mu m$
Initial cloud radius	A_0	$140\,\mu m$
Liquid pressure	p_0	$100\,kPa$
Effective dynamic viscosity	μ_E	$100\,mPa$
Void fraction	α	0.03%

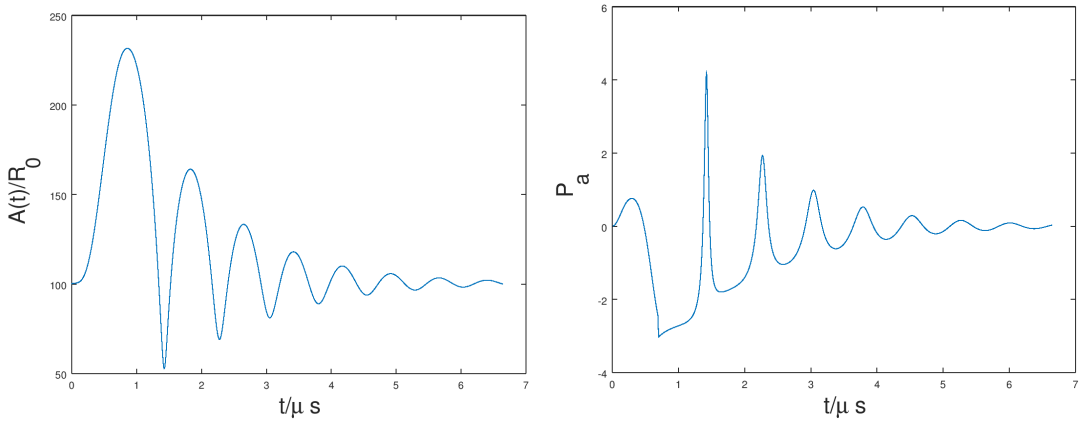

Figure 6.3: Time history of the cloud radius (left panel) and far field acoustic pressure P_a evaluated according eq. (6.5) of the oscillating bubble cloud (right panel).

6.5 Hydrofoil NACA0012

In the previous sections a brief introduction about bubble motion was presented. The passage from the case of a spherical symmetrical bubble cloud to the case of a cavitating flow is not immediate and, roughly speaking, in the mixture model each computational cell is interpreted as a cloud bubble. As a first attempt to reproduce a cavitating flow, with the aim to test the available multi-phase solver in OpenFoam, we considered a simple two-dimensional configuration: an hydrofoil NACA0012 at a low Reynolds number (based on the foil chord) $Re_c = 2000, 6000$. We first introduce some details on the multiphase solver adopted and briefly discuss the results, then we apply the FW-H equation to reconstruct the acoustic pressure field.

6.5.1 InterPhaseChangeFoam

In this section we describe some details on the multiphase solver we adopted to reproduce a two-dimensional cavitating flow over an hydrofoil. The solver, named *InterPhaseChangeFoam*, already implemented in OpenFoam, is defined as a solver for two incompressible, isothermal fluids with phase-change (e.g. cavitation). It uses a VOF (volume of fluid) phase-fraction based interface capturing approach. The momentum and other fluid properties are related to the mixture and a single momentum equation is solved with a unique density of the mixture $\rho_m = (1 - \alpha_v)\rho_L + \alpha_v\rho_v$.
In particular, the governing equations are those presented in section 6.2. Here we give a description of the source/sink terms that appear in eq. (6.1): $m^+ + m^-$.
Different phase-change models have been developed and are available in literature and many of them are present in OpenFoam, though in a simplified version. A comparative analysis of the different source/sink models response and their sensitiveness on parameters variation is described in [20]. In the present study, the model proposed by Sauer and Schnerr [56]

was adopted. This model relates the sink/source terms of the advective equation for α to the bubble dynamics expressed by the Rayleigh-Plesset equation; thus m^+ and m^- are function of bubble radius R which varies according to the ambient pressure. This means that the micro-bubbles are thought to be contained in a computational cell and the pressure related to every cell works as outer pressure for the bubble dynamics. The bubbles grow and collapse and hence change the vapor fraction in a computational cell in addition to the convective transport.
The vapor fraction α_v is defined as:

$$\alpha_v = \frac{V_v}{V_{cell}} = \frac{N_{bubbles} \cdot \frac{4}{3}\pi R^3}{V_v + V_l} = \frac{\eta V_l \cdot \frac{4}{3}\pi R^3}{\eta V_l \cdot \frac{4}{3}\pi R^3 + V_l} = \frac{\eta \cdot \frac{4}{3}\pi R^3}{1 + \eta \cdot \frac{4}{3}\pi R^3} \tag{6.9}$$

where V_{cell} is the volume of the computational cell, V_v and V_l are the volumes occupied by vapor and liquid respectively, $N_{bubbles}$ is the number of bubbles in the computational cell and η is the bubble concentration per unit volume of pure liquid.
The transport equation for the vapor fraction reads as:

$$\frac{D\alpha_v}{Dt} = \left(\frac{\eta}{1 + \eta \cdot \frac{4}{3}\pi R^3} \right) \frac{\partial}{\partial t} \left(\frac{4}{3}\pi R^3 \right) \tag{6.10}$$

Thus, the vapor production and dissipation $m^+ + m^-$ depend on the number of bubbles per cell volume (rhs: 1st parenthesis) times the volume change of a single bubble (rhs: 2nd parenthesis). The motion of the bubble radius R is ruled by the Rayleigh-Plesset equation, however, not the whole equation (6.2) is solved in interPhaseChangeFoam. If the pressure difference $p_v - \Delta p(t)$ of eq. (6.2) is large enough, after neglecting second order terms, the bubble growth may be described in terms of the single component:

$$\dot{R} = \sqrt{\frac{2}{3} \frac{p_v - \Delta p(t)}{\rho_L}}, \tag{6.11}$$

being $\Delta p(t)$ associated to the ambient cell pressure.

The InterPhaseChangeFoam solver needed some corrections regarding the correct implementation of surface tension and compression terms. The corrections were made on the basis of a work previously done by the IE-FLUIDS group on a different multiphase solver. In particular, in the original solver, surface tension and compression of the interface were activated indiscriminately throughout the whole domain. On the contrary, a consistent modeling should activate the contribution of surface tension only where it is possible to define an interface to allow compression. Moreover, in the present case, the interface is meant as the transition area from high bubble concentration region to a pure liquid region. Thus, there is no need to make it as fine as if it were an interface between two distinct phases.
In the modified solver the surface tension and the compression at the interface are controlled so as to be activated in presence of a consistent interface region. The technique that makes

this process automatic is called dynamic switch and is based on the following criterion (see for example [65]) :

$$\lambda = \frac{|\nabla\alpha|}{\max(|\nabla\alpha|)} \geq \lambda_t \tag{6.12}$$

with λ switch function and λ_t threshold value, which need to be set appropriately. When the normalized magnitude of the gradient of the void fraction λ becomes smaller than some cutoff value λ_t, actual phase dispersion and interface sharpening is turned off.
The artificial compression term in eq.(6.1) has non-zero value only at the interface and defines the flow of α_v in the normal direction to the interface. The expression for U_C is that proposed by [66] :

$$U_c = \min[C_\alpha|\mathbf{u}|, \max(|\mathbf{u}|)]\frac{\nabla\alpha}{|\nabla\alpha|}. \tag{6.13}$$

where C_α is a binary coefficient which switches interface sharpening on (1) or off (0).
The sharpening mechanism may be controlled by calibrating λ_t which is based on the multiphase flow characteristics that are taken into account. In the present work no rigorous study of dependence on this parameter has been carried out, and the cutoff value was set $\lambda_t = 0.4$ and, therefore, $C_\alpha = 1$ as $\lambda \geq \lambda_t$.
Here a comparison between the original solver (without dynamic switch) and the modified solver is reported. Noticeable differences from the original solver were observed. Figure 6.4 reports two snapshots of the cavity developing on the leading edge of the hydrofoil for the two cases: modified solver (top panels) and original solver (bottom panels). The main improvement regards the cavity contour, which appear smoother so as to make the vapor region homogeneous and not jagged as in the original solver results. However, in general, the cavity shape develops similarly in the two cases.

6.5.2 Cavitating hydrofoil

In this section, the aforementioned modified solver is adopted to reproduce a cavitating flow around a two-dimensional hydrofoil NACA0012 at different conditions. Three cases are considered and details of the simulations are summarized in Table 6.3, in particular U_0 is the uniform inlet velocity and the Reynolds number Re is based on U_0 and the chord length $c = 0.1m$. It was adopted the same grid for the three cases, it consists of 250000 cells. The downstream section of the computational domain is $4c$ long and half height of channel is $1.5c$.
The flow around the hydrofoil for the three simulations was developed (deactivating the cavitation) until a regular vortex shedding was observed. Then, the vapor pressure p_v was set as to obtain the cavitation numbers listed in Table 6.3. Since the occurrence of cavitation, the simulations ran for a period of about $T = 6s$. The constant time step needed to be very low in order to keep the Courant under 0.01, they are $\Delta t = 0.00002$, 0.00005, 0.0001 for $N2a$, $N2b$ and $N6$ respectively. The initial radius is set $R_0 = 10^{-6}$.
We have to point out that the physical characteristics of the vapor bubble, which forms and develops over time, can not be compared with previous experimental studies, since the

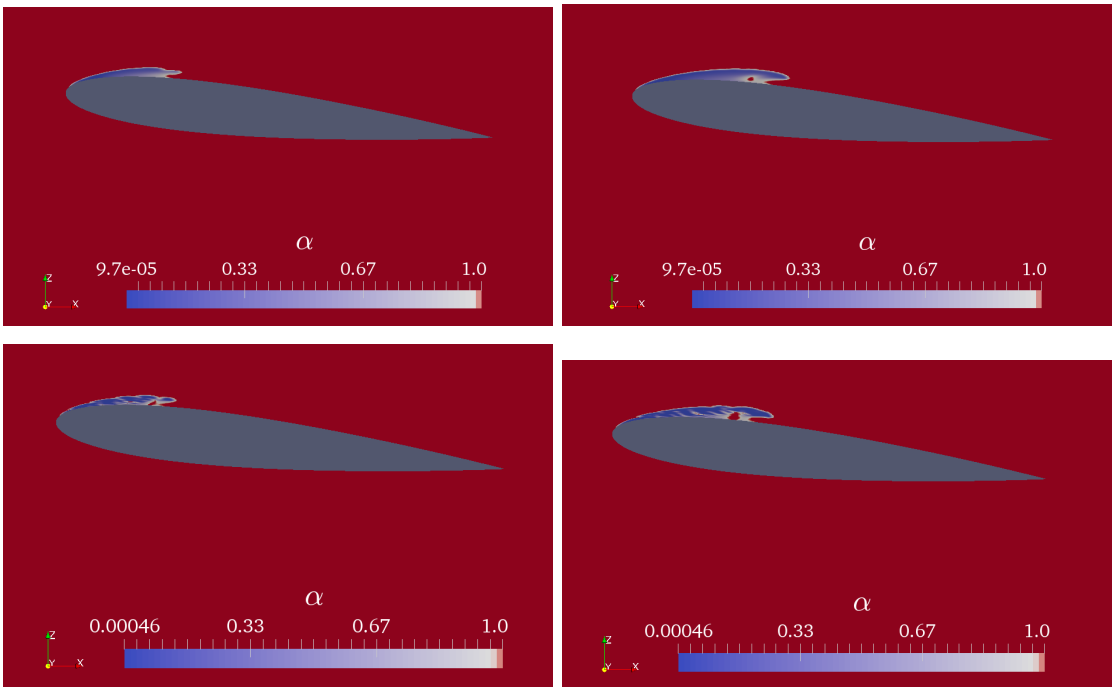

Figure 6.4: Snapshots of the volume vapor fraction α which depict the cavity forming on the leading edge of the airfoil then being transported by the flow.

three-dimensional effects, which largely affect the dynamics of the cavity, are not taken into account. Anyway, results observed were considered qualitatively adequate for the purpose of the present study. Different angle of attack, inlet velocity and vapor pressure p_v have lead to different response of the cavity motion.
As showed in figure 6.5 the inception of cavitation occurs, for the three cases, on the leading edge. The cavity grows correctly and is advected by the laminar flow. The re-entrant jet on the upper surface of the foil is strong enough just in the case $N2b$ and $N6$ (second and third column) and it induces a separation on the sheet cavitation, while a vapor cloud detaches and is driven by the flow. The $N2a$ case does not exhibit this behavior; the cavity was observed to have an initial decrease (between first and second picture of first column) and then stabilizes (third and forth picture of first column).

6.5.3 Hydrofoil acoustics

This section is dedicated to a preliminary hydroacoustic analysis of the profile in presence of cavitation. The results obtained through the FW-H formulation are presented and briefly discussed on the basis of a qualitative analysis. Very few quantitative measurements of noise from surface cavitation on hydrofoils are available in literature. In the work of Blake *et al.* [4] measurements of noise of a two-phase flow over hydrofoils were performed in a

Table 6.3: Characteristic of the three simulations performed with interPhaseChangeFoam, to reproduce a cavitating flow around an hydrofoil NACA0012.

NAME	σ	Re	AoA	U_0
N2a	1.25	2000	8^o	0.02
N2b	1	2000	8^o	0.02
N6	0.8	6000	6^o	0.06

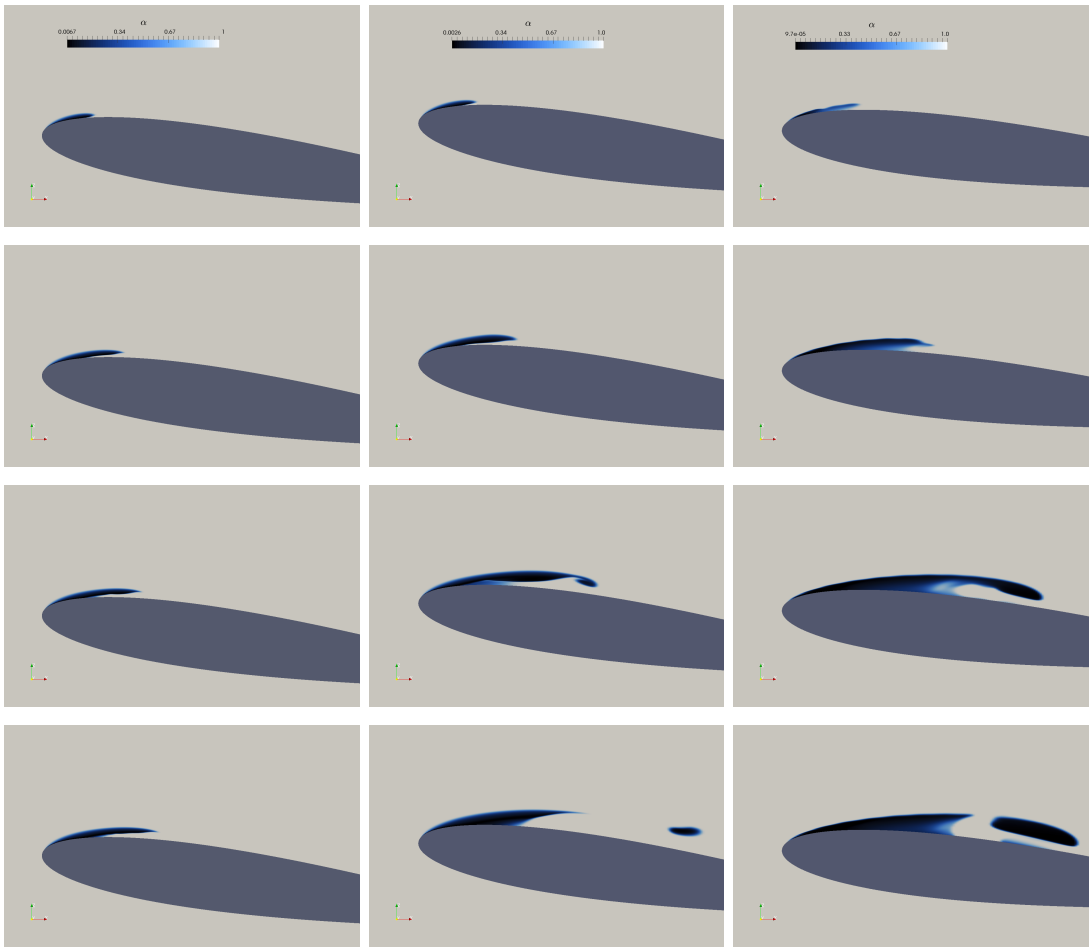

Figure 6.5: Snapshots of the volume vapor fraction α which depict the cavity forming on the leading edge of the airfoil then being transported by the flow. Three cases are reproduced and their characteristics are expressed in Table 6.3: N2a - first column, N2b second column, N6 - third column.

water tunnel (acustically calibrated). The results put in evidence the dependence of noise from the type of cavitation produced, and for each type, the dependence on speed and cavity index $\sigma = (p_\infty - p_v)/\frac{1}{2}\rho_L U_0^2$. An experimental investigation reported by Reisman and Brennen [52] concerns the acoustic pressure related to cloud cavitation appearing on hydrofoil flow. They observed large pressure impulses with typical durations of the order of tenths of milliseconds. The strength of the pressure pulses was found to depend on both the cavitationa and Reynolds number. From a qualitative point of view, their acoustic results are comperable to the pressure impulsive behavior observed in the present study.
A comparison of the pressure field extracted from the fluid dynamic simulation for the $N6$, in presence and absence of cavitation, is showed in figure 6.6 (top panel). The measurement point is set at (0, 0, 0.6c). It is evident the difference between the smooth and regular oscillatory pattern of the non-cavitating case with respect to the richer signal of the cavitating case. This last signal preserves an oscillatory mode due to the main motion of the flow, which is still characterized by the vortex shedding on the trailing edge; however, it also exhibits clear pressure disturbances appearing as the several peaks. In the bottom panel of Figure 6.6 the pressure signals of the three cases are compared; it shows how the $N6$ case presents a jagged signal, this is due to the high volume variation of the vapor cavity. In fact, the pressure peaks due to the vapor cavity rebounds remind the behavior of the bubble cloud acoustic peaks, evaluated in the previous section. In Figure 6.7 the spectrum of bubble cloud pressure signal (depicted in Figure 6.6) is compared with the spectrum of the cavitating hydrofoil, whose pressure signal in time was obtained by running the $N6$ case with a time step $dt = 10^{-6}$ (and sampling the pressure data at every time step), in order to have an appreciable comparison on the highest frequencies. The comparison, however, has a qualitative purpose, due to the different physical conditions that characterize the two cases. Moreover, the acoustic field radiated from the hydrofoil has an intrinsic directivity while the pressure signal of the bubble cloud has radial symmetry.
In order to validate the FW-H solution in the particular case of cavitating flows, we report the comparison of the acoustic pressure field obtained by the porous and direct FW-H solution with respect to the fluid dynamic pressure, here assumed as a reference data. The direct FW-H solution was applied as follows: the loading terms were evaluated on the hydrofoil surface, the quadrupole terms were evaluated in the liquid section of the volume (i.e. where $\alpha = 1$) and the thickness term was considered on the cavity surface, so as to take into account the effects of the volume variation of the cavity on the acoustic field. However, the adopted solver doesn't provide a sharp interface, in fact, a thick layer of cells assume values in the range $0 < \alpha < 1$. They represent regions where the concentration of bubbles gradually decreases, until they encounter cells containing pure water. This vapor mixture, represented by the entire region where $\alpha < 1$, was treated as if it were a bubble cloud, described in the previous section. Consequently, the thickness noise term T_{th} is evaluated as:

$$T_{th} = \frac{\partial}{\partial t}\int_{S_c}\left[\frac{\rho_v v_n}{r}\right]_\tau dS_c = \frac{\partial}{\partial t}\int_{V_c}\left[\nabla\cdot\frac{\rho_v v}{r}\right]_\tau dV_c \tag{6.14}$$

where v_n represents the velocity of the vapor mass projected along n the outward normal

to the cavity surface S_c, while V_c is the cavity volume. Due to the absence of a defined interface on which to calculate the normal unit vector and the surface element dS_c, the right formulation in equation (6.14) was adopted. The porous formulation remains unchanged from that adopted in the previous chapters. The porous domain is a box which is left open at the outlet side. Both the formulations, depicted in Figure 6.8, are able to reproduce the pressure disturbance satisfactorily, although the signals do not exactly overlap.

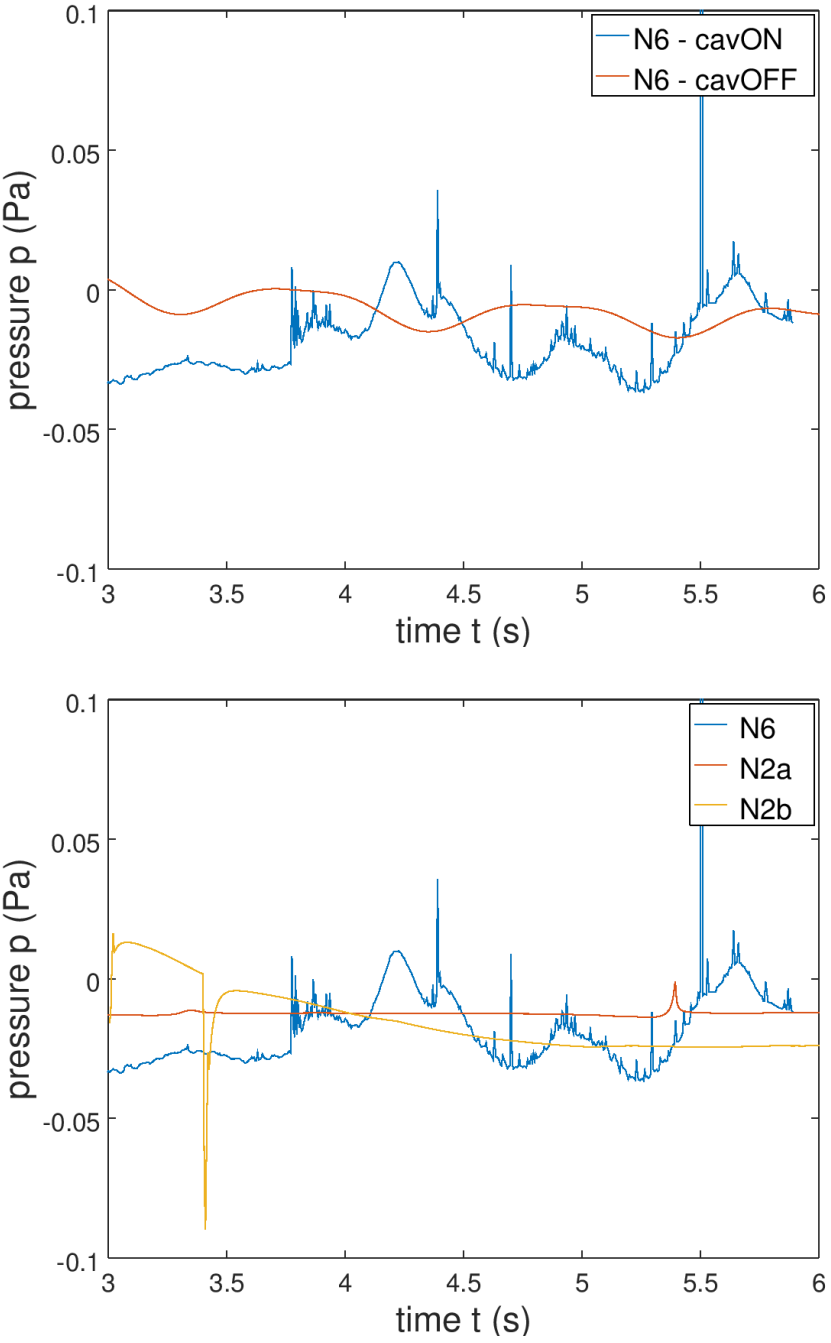

Figure 6.6: Top panel: comparison of pressure field in the case $N6$ of Table 6.3 with respect to the activation (*cavON*) or deactivation (*cavOFF*) of cavitation. Bottom panel: Comparison of pressure field for the three cases $N2a$, $N2b$ and $N6$ of Table 6.3. Measurement point is (0, 0, 0.6c).

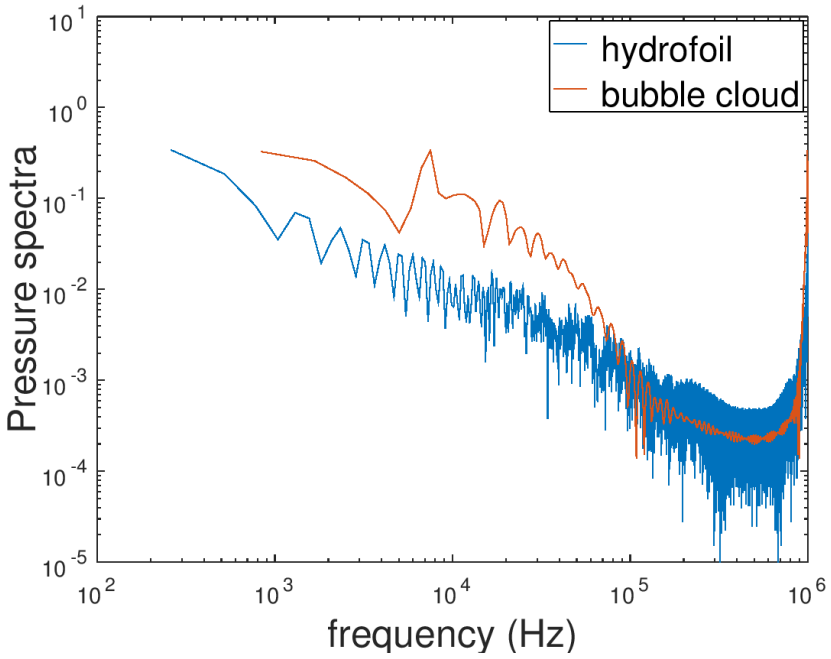

Figure 6.7: Pressure spectra corresponding to the pressure time hystory of the bubble cloud depicted in Figure 6.3 and of the cavitating hydrofoil depicted in Figure 6.6.

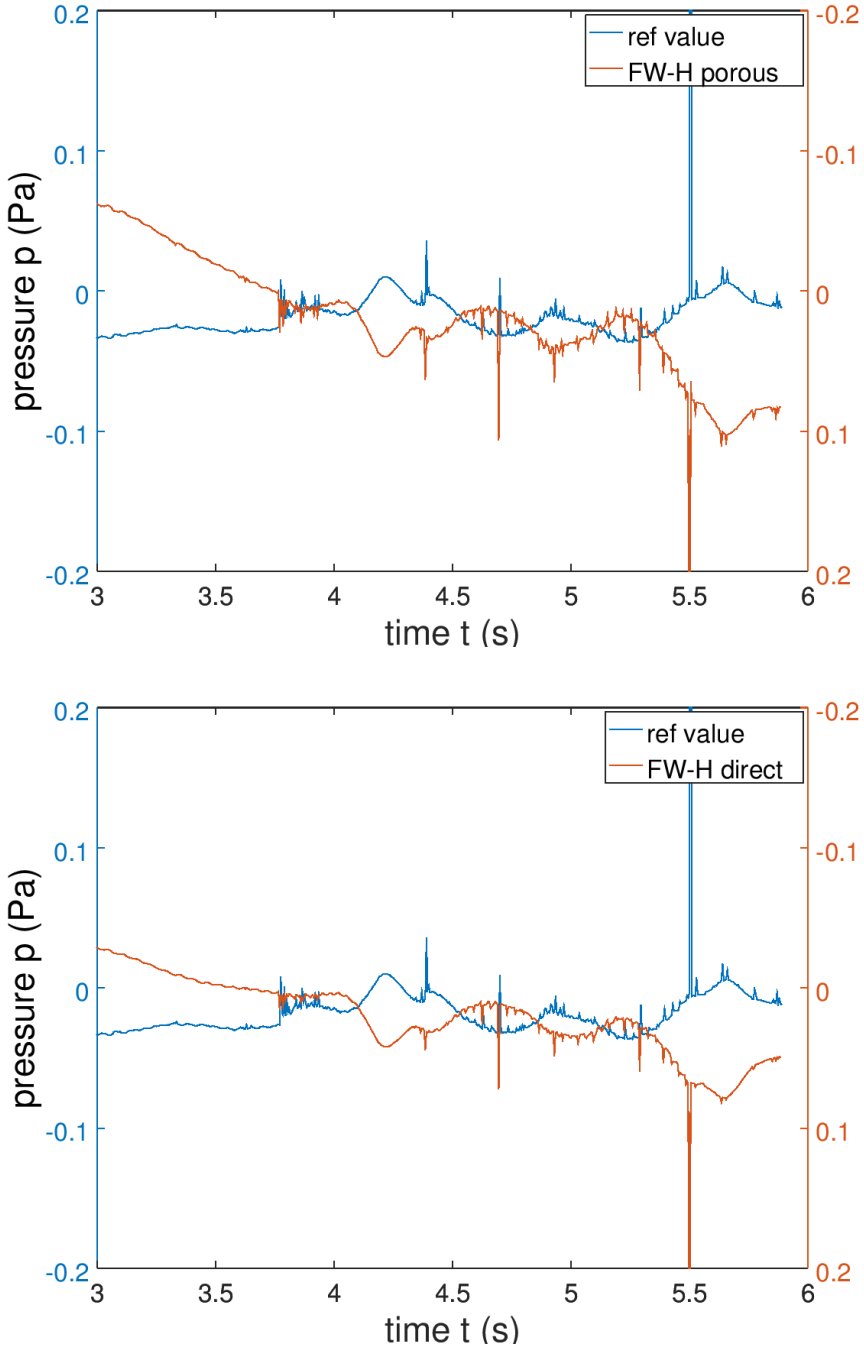

Figure 6.8: Comparison of pressure reference with FW-H signal, porous formulation (top panel) and direct formulation (bottom panel). The case considered is $N6$ whose details are in Table 6.3. Measurement point is (0, 0, 0.6c).

Chapter 7

Concluding remarks

In the present thesis the accuracy of different numerical methodologies to solve the (convective) FW-H equation were investigated and the noise generated by archetypal three-dimensional bodies placed in a uniform current has been estimated.
In order to consider the nonlinear contribution to the generation of noise, the convective form of the quadrupole term has been formulated. The analysis is significant in the turbulent incompressible flow regime.
As a fluid-dynamic problem, first the flow around a finite size cylinder with square section, at $Re = 4000$, has been considered. Although simple, this case exhibits a number of points of interest for the generation and propagation of fluid dynamic noise. First, it is characterized by the presence of a turbulent wake, combined with a vortex sheet, which gives rise to a significant contribution form the FW-H quadrupole source terms; second, it is representative of a wide class of problems of interest in engineering.
The fluid-dynamic field was solved using wall-resolving LES and validated using available literature data. This simulation provides both the input data for the acoustic solvers and a reference pressure to check the reliability of noise predictions given the negligible role played by the compressibility delays. The results from a (pure linear) Curle solution, the standard porous formulation, the direct approach including the computation of the volume, nonlinear terms and a combination of porous and direct methods, were compared. The calculations confirm that in cases where the acoustic field is essentially of nonlinear nature (like those herein investigated), the noise due to the fluid dynamic loads occurring on body surface is relevant just in a very near region close to the body itself; thus, as expected, the Curle solution is inadequate to evaluate the noise signature far from the cylinder, both in terms of amplitude and frequencies. The porous formulation successfully predicts the main frequency components of the resulting signature, but their amplitude can be undervalued and the solutions are somehow sensitive to the position of measurement points, as well as the choice of the integration domain. This can be attributed to the overall distribution of nonlinear sources and their main cross-stream directivity. On the contrary, the direct approach provides a noise prediction very similar to reference data everywhere in the field, at least at points where (according to the fundamental assumption

on which the FW-H equation is based) the pressure is characterized by small (acoustic) perturbations. This methodology is easy to be implemented, fully exploits the underlying CFD solution and makes the calculations free from any arbitrariness concerning the radiating domain. Nevertheless, its applicability is presently limited to problems where the effects of fluid-dynamic compressibility on noise propagation can be neglected (low Mach number and absence of cavitation); in this context, the acoustic calculations could be even coded within the fluid dynamic solver, thus avoiding any complex post processing of huge set of data. The coupling of porous and direct methods appears as a further, valid and convenient, computational approach: although not able to fit the direct solution perfectly, it can improve the solution achieved by the pure porous formulation, somehow relaxing any rigorous requirement about the choice of the integration domain; then, it may be considered a useful and interesting compromise between accuracy and computational cost for engineering purposes.

As further cases of study, the flow around a sphere, a cube and a prolate spheroid has been reproduced, at a value of the Reynolds number, based on the square root of the frontal area, $R_A = 4430$. The acoustic analogy has been used, solving the turbulent fluid dynamic field through wall-resolving LES and the FW-H equation for the evaluation of the acoustic far-field noise. The quadrupole term of the FW-H equation was solved through direct volume integration.

The analysis of the fluid-dynamic data showed that the cube has the widest and most energetic and irregular wake mainly associated to the sharp corners. At the opposite stands the prolate spheroid, whose the streamlined shape provides a small slender wake characterized by a low level of turbulent kinetic energy. These differences were shown to impact the generated hydrodynamic noise.

The comparison of the acoustic field generated by sphere, cube and ellipsoid demonstrate how body shape is decisive in the generation of different types of hydroacoustic noise. Specifically, the cube appears to be the loudest with a signal composed of a wide spectrum of frequencies; the sphere is characterized by an almost monochromatic signal with smaller amplitude compared to the cube; the prolate spheroid provides a pressure signal one order of magnitude lower than the other cases, associated to a very low frequency.

The analysis of the contribution of the different terms of the FW-H equation showed that for the bluff bodies (cube and sphere) the linear terms contribute to the overall noise signal more than the non-linear ones. The opposite is true for the streamlined body (prolate spheroid).

Finally, a preliminary comparison between the noise generated by the cube and by square elongated cylinder, shows that the aspect ratio of the body might affect the relative importance between linear and non-linear contributions to the acoustic field. This has been attributed to the persistence of the two-dimensionally shaped wake in case of elongated cylinder when compared to the three-dimensional one generated by the cube. This issue deserves a successive study.

Last part of the thesis represents an introductory study on the noise radiated from cavitating flows. To gradually approach the complex physics involved first the dynamics and the acoustics of a single bubble were reproduced, using the Rayleigh-Plesset equation that

governs the motion of the radius of a bubble with spherical symmetry and the thickness term of the FW-H equation which is related to the pulsations of the bubble. Then, a spherical ensemble of bubble was considered, and it was observed how the viscosity influences the bubble dynamics within the cloud distinguishing it from that of an isolated bubble. Moreover, other parameters were found to considerably influence the solution of the bubble cloud equations, however, the study on the complex dynamics of the bubbles was considered beyond the scope of this thesis. Finally, a cavitating flow around an hydrofoil was reproduced by adopting the mixture model, which considers an advected vapor fraction and relates the condensation/vaporization rates to the bubble radius. Different Reynolds and cavitation numbers were considered. Since the case of $Re = 6000$ turned out to be the most interesting and "noisy", it was qualitatively compared to the bubble cloud pressure signal and similar type of pressure peaks due to the vapor cloud rebounds were observed.
All the Large-Eddy Simulations described in this study were performed by adopting customized solvers present in OpenFOAM® . The acoustic solver (namely the integral formulations of the FW-H equation) was implemented as a post-processing utility within the OpenFOAM® platform.
All the topics addressed in this thesis deserve further investigations.
The coupling of LES and FW-H equation may be adopted to study more complex configurations, such as an isolated marine propeller or a propeller behind hull. Some works are already available in literature concerning an isolated propeller, it would be interesting to adopt the FW-H direct formulation and isolating different region of the volume one may identify the main noise source which characterize the wake. A more accurate study may concern the response of objects immersed in a flow according to their particular surface geometry. Indeed, the surface variations can largely affect the loading term contribution; either the effect of roughness or a mechanism of absorption of the fluid dynamic forces by the object's walls may be considered. Moreover, the effect of sound wave reflection may be faced by adopting the Green's function for the semi-space and the phenomenon of refraction may be investigated by changing gradually both the density and speed of sound of the medium where the sound waves propagates.
The reproduction of cavitating flows and the noise emissions related to them have many aspects that need to be clarified and improved. For example, the multiphase solver adopted in this thesis may take into account for a more complex bubble dynamics than the one already considered. Moreover, the effects of coalescence, separation and collapse are not provided in the current solver.
All the aspects just mentioned are interesting, they deserve careful research and may be developed in the near future.

Bibliography

[1] Achenbach E., "Vortex shedding from spheres", *J Fluid Mech* 62, pp. 209-221, (1974).

[2] Bakic V., "Experimental investigation of turbulent flows around a sphere", *Ph.D. Thesis*, TUHH Hamburg, Germany, (2002).

[3] Bensow R.E., Liefvendhal M., "An acoustic analogy and scale-resolving flow simulation methodology for the prediction of propeller radiated noise", *31th Symposium on Naval Hydrodynamics, California,* (2016).

[4] Blake W.K., Wolpert M.J. and Geib F.E., "Cavitation noise and inception as influenced by boundary-layer development on a hydrofoil", *J Fluid Mech* 80, 4, pp. 617-640, (1977).

[5] Blokhintsev D., "Acoustics of a nonhomogeneous moving media", NACA TM–1399 (http://ntrs.nasa.gov), (1956).

[6] Brennen C.E., "Cavitation and Bubble Dynamics", *Oxford University Press*, Oxford, (1995).

[7] Brentner K.S. and Farassat F., "Analytical comparison of the acoustic analogy and Kirchhoff formulation for moving surfaces", *AIAA Journal*, 36 (8), 1379-1386, (1998).

[8] Brentner K.S. and Farassat F., "Modeling aerodynamically generated sound of helicopter rotors", *Progress in Aerospace Sciences* 39, 2-3, pp. 83-120, (2003).

[9] Carlton J. S., Vlasic D., "Ship vibration and noise: some topical aspects", *1st International Ship Noise and Vibration Conference*, pp. 1-11, (2005).

[10] Ceccio S.L. and Brennen C.E., "Observations of the dynamics and acoustics of travelling bubble cavitation", *J. Fluid Mechanics* 233, pp. 633 - 660, (1991).

[11] Cintolesi C., Petronio A., Armenio V., "Large eddy simulation of turbulent buoyant flow in a confined cavity with conjugate heat transfer", *Physics of Fluids* 27, (2015).

[12] Chang N.A. and Ceccio S.L., " The acoustic emissions of cavitation bubbles in stretched vortices", *J. Acoustical Society of America* 130(5), pp. 3209 - 3219, (2011).

[13] Choi J. and Ceccio S.L., "Dynamics and noise emission of vortex cavitation bubbles", *J. Fluid Mechanics* 575, pp. 1 - 26, (2007).

[14] Chomaz J.M., Bonnetin P. and Hopfinger E.J., "The structure of the near wake of a sphere moving horizontally in a stratified fluid", *J Fluid Mech*, 254, pp. 1-21, (1993).

[15] Curle N., "The influence of solid boundaries upon aerodynamic sound", *Proceedings of Royal Society* A231(1187), pp. 505-514, (1955).

[16] D'Agostino L. and Brennen C.E., "On the acoustical dynamics of bubble clouds", *ASME Cavitation on Multiphase Flow Forum*, pp. 72 - 75, (1983).

[17] Di Francescantonio P., "A new boundary integral formulation for the prediction of sound radiation", *Journal of Sound and Vibration*, 202(4), pp. 491-509, (1997).

[18] Ffowcs Williams J.E. and Hawkings D.L., "Sound generation by turbulence and surfaces in arbitrary motion", *Philosophical Transaction of Royal Society*, 264(A1151), pp. 321-342, (1969).

[19] Frank J.P., "Physics and Control of Cavitation. In Design and Analysis of High Speed Pumps" , *Educational Notes RTO-EN-AVT-143*, Paper 2. Neuilly-sur-Seine, France: RTO, pp. 2-1 - 2-36, (2006).

[20] Frikha S., Coutier-Delgosha O. and Astolfi J.A., "Influence of the cavitation model on the simulation of cloud cavitation on 2D foil section", *International Journal of Rotating Machinery*, p. 12, (2008).

[21] Fujikawa S. and Akamatsu T., "Effects of the non-equilibrium condensation of vapour on the pressure wave produced by the collapse of a bubble in a liquid", *J. Fluid Mechanics*, Volume 97, Issue 3, pp. 481-512, (1980).

[22] Germano M., Piomelli U., Moin P., and Cabot W., "A dynamic subgrid-scale eddy viscosity model", *Phys. Fluids* A3, p. 1760, (1991).

[23] Gloerfelt X., Perot F., Bailly C., Juve D., "Flow-induced cylinder noise formulated as a diffraction problem for low Mach numbers", *Journal of Sound and Vibration*, 287, pp. 129-151, (2005).

[24] Herbert E., Balibar S. and Caupin F., "Cavitation pressure in water", *Phys. Rev.* E 74, (2006).

[25] Ianniello S., "New perspectives in the use of the Ffowcs Williams-Hawkings equation for aeroacoustic analysis of rotating blades", *Journal of Fluid Mechanics*, 570, pp. 79–127, (2007).

[26] Ianniello S., Muscari R. and Di Mascio A., "Ship underwater noise assessment by the acoustic analogy. Part I: nonlinear analysis of a marine propeller in a auniform flow", *Journal of Marine Science and Technology*, 18(4), pp. 547-570, (2013).

[27] Ianniello S., "The Ffowcs Williams-Hawkings equation for hydroacoustic analysis of rotating blades. Part I. The rotpole", *Journal of Fluid Mechanics*, 797, pp. 345-388, (2016).

[28] Ikeda T., Enomoto S. and Yamamoto K., "Quadrupole Corrections for the Permeable-Surface Ffowcs Williams–Hawkings Equation", *AIAA J OURNAL* Vol. 55, No. 7, (2017).

[29] Inoue O. and Hatakeyama N., "Sound generation by a two-dimensional circular cylinder in a uniform flow", *Journal of Fluid Mechanics*, 471, pp. 285-314, (2002).

[30] Kim H.J. and Durbin P.A., "Observations of the frequencies in a sphere wake and of drag increase by acoustic excitation", *Phys Fluids* 31(11), pp. 3260-3265, (1988).

[31] Kim K.C., Lee M. B., Yoon S. Y., Boo J. S. Chun H. H., "Phase averaged velocity field in the near wake of a square cylinder obtained by a PIV method", *Journal of Visualization*, 5(1), pp. 29-36, (2002).

[32] Lyrintzis A. S., "Review. The use of Kirchhoff's methods in computational aeroacoustics", *ASME Journel of Fluids Engineering*, 202(4), (1997).

[33] Lafitte A. and Pérot F., "Investigation on the noise generated by cylinder flows using direct Lattice-Boltzmann approach", *15th AIAA/CEAS Aeroacoustics Conference*, AIAA 2009-3268, (2009).

[34] Lele S.K., Nichols J.W., "A second golden age of aeroacoustics?", *Phil. Trans. R. Soc.*, A 372: 20130321, (2014).

[35] Lighthill M.J., "On sound generated aerodynamically. I General theory", *Proceedings of Royal Society*, A211(11079), 564, (1952).

[36] Lilly D., "A proposed modification of germano subgrid-scale closure method", *Phys. Fluids* A4, p. 633, (1992).

[37] Lockard D. P. and Casper J. H., "Permeable surface corrections for Ffowcs Williams and Hawkings integrals", *11th AIAA/CEAS Aeroacoustics Conference*, AIAA-2005-2995, (2005).

[38] Lyn D. A., Einav S., Rodi W., Park J. H., "A laser-Doppler velocimetry Study of the ensemble-averaged characteristics of the turbulent near wake of a square cylinder", *Journal of Fluid Mechanics*, 304, pp. 285-319, (1995).

[39] Marsden O., Bogey C. and Bailly C., "Direct noise computation of the turbulent flow around a zero-incidence airfoil", *AIAA Journal*, 46(4), pp. 874-883 (2008).

[40] Martinez-Lera P., Muller A., Schram C., Rambaud P., Desmet W., Anthoine J., "Robust aeroacoustic computations based on Curle's and Powell's analogies", *Proceedings of the International Conference on Noise and Vibration Engineering*, pp. 513-524, (2008).

[41] Meneveau C., Lund T., and Cabot W., "A lagrangian dynamic subgrid-scale model of turbulence", *J. Fluid Mechanics* 316, p. 353, (1996).

[42] Murphy E., King E., "Environmental Noise Pollution", *Elsevier*, (2014).

[43] Najafi-Yazdi A., Bres G. A. and Mongeau L., "An acoustic analogy formulation for moving sources in uniformly moving media", *Proceedings of Royal Society London*, A467, pp. 144-165, (2011).

[44] Nitzorski Z. and Mahesh K., "A dynamic technique for sound computation using the Ffowcs Williams and Hawkings equations", *Physics of Fluids*, 26(11), 115101, (2014).

[45] Okajima A., "Strouhal numbers of rectangular cylinders", *Journal of Fluid Mechanics*, 123, pp. 379-398, (1982).

[46] van Oudheusden B. W., Scarano F., van Hinsberg N. P., Watt W., "Phase-resolved characterization of vortex shedding in the near wake of a square-section cylinder at incidence", *Experiments in Fluids*, 39, pp. 86-98, (2005).

[47] Piomelli U., Craig L. S. and Sarkar S., "On the computation of sound by large-eddy simulation", *Journal of Engineering and Mathematics* 32, pp. 217-236, (1997).

[48] Plesset, M.W., "The dynamics of cavitation bubbles, *J. Applied Mechanics* 16, pp. 277 - 282, (1949).

[49] Rahier G., Huet M. and Prieur J., "Additional terms for the use of Ffowcs Williams and Hawkings surface integrals in turbulent flows", *Computers and Fluids* 120, pp. 158-172, (2015).

[50] Rayleigh, Lord "On the pressure developed in a liquid during the collapse of a spherical cavity", *Philosophical Magazine Series* 6, 34: 200, pp. 94 - 98, (1917).

[51] Reisman G.E., McKenney E.A. and Brennen E.A., "Cloud cavitation on an oscillating hydrofoil", *Proc. 20th ONR Symp. on Naval Hydrodynamics*, pp. 78 - 89, (1994).

[52] Reisman G.E. and Brennen E.A., "Pressure pulses generated by cloud cavitation", *FED-Vol.236, 1996 Fluids Engineering Division Conference*, Vol 1, ASME (1996).

[53] Riccardi G. and De Bernardis E., "Dynamics and acoustics of a spherical bubble rising under gravity in an inviscid liquid", *J. Acoustical Society of America* 140, 1488, pp. 1488 - 1497, (2016).

[54] Rodi W., Constantinescu G. and Stosser T., "Large-Eddy Simulation in Hydraulics", *CRC Press/Balkema, Taylor & Francins Group*, London, UK, (2013).

[55] Rodriguez I., Lehmkuhl O. Borrell R., Oliva A. and Perez-Segarra C.D., "Direct numerical simulation of turbulent wakes:flow past a sphere at Re=5000", *V European Conference on Computational Fluid Dynamics*, (2010).

[56] Sauer J. and Schnerr G.H., "Unsteady cavitating flow - a new cavitation model based on a modified front capturing method and bubble dynamics", *Proc. of FEDSM00, ASME Fluids Engineering Summer Conference*, (2000).

[57] Seidl V., Muzaferija S. and Peric M., "Parallel DNS with local grid refinement", *Applied Scientific Research* 59, pp. 379-394,(1998).

[58] Seror C., Sagaut P., Bailly C., Juvé D., "On the radiated noise computed by large-eddy simulation", *Physics of Fluids* 13(2), (2000).

[59] Sakamoto H. and Haniu H., "A study on vortex shedding from spheres in a uniform flow", *J of Fluids Eng* 112, pp. 386-392, (1990).

[60] J. Smagorinsky, "General circulation experiments with the primitive equations: I. the basic experiment", *Mon. Weather Rev.* 91 , p. 99, (1963).

[61] Van Driest E.R., "On the turbulent flow near the a wall", *Journal of Aeronautical Science* 23, pp. 1007 - 1011, (1956).

[62] Wagner C. A., Huttl T., Sagaut P., "Large-Eddy Simulation for Acoustics", *Cambridge University Press*, (2007).

[63] Wallace J.M. and Piomelli U., "Class notes, ENME 656, Physics of turbulence", *University of Maryland*, (1998).

[64] Wang Y.C. and Brennen C.E., "The noise generated by the collapse of a cloud of cavitation bubbles", *ASME Cavitation and Gas-Liquid Flow in Fluid Machinery Devices*, pp. 17 - 29, (1995).

[65] Wardle K.E. and Weller H.G., "Hybrid multiphase CFD solver for coupled dispersed/segregated flows in liquid-liquid extraction", *International Journal of Chemical Engineering*, p 1-13, (2013).

[66] Weller H., "A new approach to VOF-based interface capturing methods for incompressible and compressible flow", *OpenCFD Ltd., Report TR/HGW/04*, (2008).